Technische Universität München
Fakultät für Elektrotechnik und Informationstechnik
Professur für Mikrostrukturierte Mechatronische Systeme

Nature-Inspired Capacitive Sensor

Cyril Baby Karuthedath

Vollständiger Abdruck der von der Fakultät für Elektrotechnik und Informationstechnik der Technischen Universität München zur Erlangung des akademischen Grades eines

Doktor- Ingenieurs

genehmigten Dissertation.

Vorsitzender: Prof. Dr.-Ing. Georg Sigl
Prüfer der Dissertation:
1. Prof. Dr.-Ing. Norbert Schwesinger
2. Prof. Dr.-Ing. Walter Hansch,
Universität der Bundeswehr München

Die Dissertation wurde am 13.04.2017 bei der Technischen Universität München eingereicht und durch die Fakultät für Elektrotechnik und Informationstechnik am 06.11.2017 angenommen.

Nature-Inspired Capacitive Sensor

Cyril Baby Karuthedath

Abstract

Inspired by nature, a new class of sensors, called 'sensors with unique and unclonable characteristic', has been developed. Similar to sensors in nature, they respond to a measurand and provide a unique output. Random variations in the structure of the sensors are responsible for these unique characteristic. As random variations are difficult to measure, model and duplicate, it is impossible to clone these sensors. Such sensors are very interesting, as they can be used as hardware identifiers, as sensors with an integrated identifier and also as nature-like sensors.

Capacitive sensors with unique and unclonable characteristic are proposed. The sensors respond to tilt and provide unique and unclonable capacitance output. Random structural variations integrated into the sensor structure during the fabrication process are the sources of these unique and unclonable sensor characteristic. The design, modeling, simulation, optimization, fabrication, testing and applications of these capacitance-based, unique and unclonable tilt sensors are presented in this thesis.

Zusammenfassung

Von der Natur inspiriert, wurde eine neue Art von Sensoren entwickelt: Sensoren mit einzigartigen und unklonbaren Merkmalen. Ähnlich wie Sensoren in der Natur, reagieren diese auf eine Messgröße und liefern dabei spezifische und einzigartige Werte. Willkürliche Variationen im Aufbau der Sensoren sind zuständig für diese einzigartigen Merkmale. Da willkürliche Variationen schwierig zu messen, modellieren oder duplizieren sind, ist es unmöglich diese Sensoren zu klonen. Solche Sensoren sind von größtem Interesse, da diese zur Hardwareidentifizierung, als Sensoren mit integriertem Identifikator oder auch als natur-ähnliche Sensoren eingesetzt werden können.

Kapazitive Sensoren mit einzigartigen und unklonbaren Merkmalen werden vorgeschlagen. Die Sensoren reagieren auf Neigung und liefern einzigartige, unklonbare Kapazitätswerte. Willkürliche Variationen im Sensoraufbau während dem Herstellungsprozess sind die Quelle dieser einzigartigen und unklonbaren Merkmale. In dieser Arbeit werden Design, Modellierung Simulation, Optimierung, Herstellung, Testen und Applikation solcher kapazitiven, einzigartigen und unklonbaren Neigungssensoren präsentiert.

Contents

List of Abbreviation

BC	Base Component
CA	Curing Agent
CH	Challenge
CPDMS	Conductive Polydimethylsiloxane
CRP	Challenge Response Pair
EID	Electronic Identifier
EMI	Electromagnetic Interference
F	Floating Electrode
FEA	Finite Element Analysis
G	Ground
IDE	Interdigitated Electrode
IoT	Internet of Things
MEMS	Microelectromechanical System
NTC	Negative Temperature Coefficient
OA	Operational Amplifier
PCB	Printed Circuit Board
PD	Packing Density
PDMS	Polydimethylsiloxane
RS	Response
R	Receiver Electrode
SM	Sensor Model
T	Transmitter Electrode

List of Symbols

A	Area
a	Acceleration
C	Capacitance
d	Diameter
E_Y	Young's modulus
F	Force
g	Acceleration due to gravity
I, i	Current
L	Length
M, m	Mass
P	Pressure
R	Resistance
r	Radius
S	Surface
t	Thickness
V	Voltage
W	Width
w	Deflection
x	Distance
θ	Angle
ρ_c	Concordance Correlation Coefficient
μ	Poisson's ratio
σ	Stress
ϵ	Strain

1 Introduction

1.1 Nature: Inspiration

Nature is a source of inspiration for many researchers and scientists around the globe, who look upon it as a model, mentor and measure [1]. From waste management to transportation, nature has provided solutions to various engineering problems over the years; for instance, the kingfisher inspired Japanese engineers to solve noise problems in high-speed trains [2]. In addition, the structures of bones and trees are perfect examples of how to maximize strength while minimizing materials [3], whilst termite mounds have inspired architects to devise a number of structural solutions [2]. All of these nature-inspired solutions are efficient and well adapted to the surrounding conditions.

The sensor domain also follows the same trend. Researchers have studied various natural sensors, all of which have a diverse set of properties that have evolved over millions of years. These sensors help different species to survive in their environment. Humans and animals rely on visual, acoustic, olfactory and tactile sensors for navigation, localization, object detection, spatial orientation, discrimination, etc., but beyond this point, certain species have developed specialized sensors to understand their complex surroundings. For instance, some types of beetle can detect IR (infrared) energy emanating from forest fires or the body heat of other animals [4]. Furthermore, bats use ultrasonic waves to navigate in the dark, while dolphins use it for underwater navigation and ranging (echolocation) [5], and elephants can sense seismic vibrations created by herds many miles away [6]. In addition, certain aquatic creatures have the ability to emit and detect weak electromagnetic fields, known as 'electrolocation', for localization purposes [7], and fish use spacial hair cell sensors, called 'lateral lines', for prey detection, spatial orientation, flow imaging, etc. [8]. All of these natural sensors are far superior to their artificial counterparts, which has motivated engineers to mimic nature's sensing strategies in artificial domains.

Various sensors have been developed by copying from nature, either functionally or structurally, or both. Taste sensors have been developed by mimicking the functionality of the tongue [9], whilst an electronic nose, copying the human nose, has also been developed [10]. Artificial skin with the properties of human skin has been reported in [11], and electrolocation and echolocation have been artificially replicated in [12] and [13], respectively. Bio-inspired hair sensors and lateral lines have been developed for flow imaging, prey detection, spatial orientation, etc. [14]- [16], all of which offer several advantages, such as high signal-to-noise-ratios, high sensitivity over a large bandwidth and uniqueness, over traditional sensors.

1.2 Sensing in Biological and Artificial Systems

Nature-inspired sensors are developed by transforming biological (in nature) sensor models into engineering solutions, which are then applicable to artificial (traditional) systems. To develop such sensors, a general understanding of both biological and artificial sensing systems is required. An overview of a biological sensing system is shown in Fig. 1.1(a). It consists of an auxiliary structural element, such as an ear, a cornea, a hair cell structure, etc., designed to accept the external stimulus, which, when collected, is passed to the sensory receptors. Depending on the stimulus to which they respond, sensory receptors can be broadly classified as 'mechanoreceptors' (respond to mechanical stimulus), 'chemoreceptors' (respond to chemical stimulus), or 'photoreceptors' (respond to electromagnetic and thermal stimulus). These sensory receptors convert the stimulus into electro-chemical signals. Neurons are designed to accept these electrochemical signals and carry them as an 'action potential' to the brain, which in turn distinguishes the type of sensory signal and the intensity of the stimulus from the identity of the neuron and frequency of the signal. After processing, the brain compares the received signal with patterns stored in the memory, to create sensor perception.

An artificial sensing system is shown in Fig. 1.1(b). It is analogous to the biological sensing system. In an artificial sensing system, a sensor or a transducer accepts an external stimulus and converts it into a more suitable output. Depending on the sensing principle, sensor output can be a change of resistance, capacitance, inductance, current, voltage, etc. In an artificial domain, most systems read, transmit, process and store information as a voltage (analog or digital) signal, and only a few sensors, such as hall sensors, thermocouples and photodetectors, provide a direct voltage output. Other

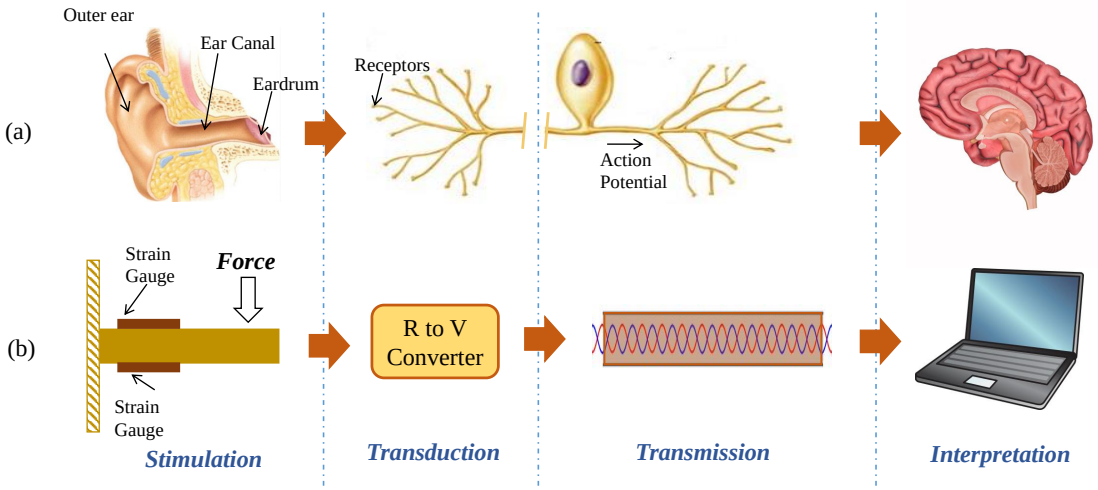

Figure 1.1: (a) Artificial Sensing System (b) Natural Sensing System

types of sensor (capacitive, inductive, resistive, etc.) require an interface circuit to convert sensor output into a corresponding voltage signal, which is then transmitted to a computer (or processor) for further processing. The signal is proportional to the stimulus. The processor requires a mapping function, in order to map the received voltage signal to a corresponding stimulus. These mapping functions are generated through calibration.

1.3 Unique and Unclonable Sensors in Nature

Everything in nature is unique—even within a species, no two individuals are alike, and every offspring differs from its parents in random ways [17]. Consider humans, for instance, whereby each person is unique: The characteristics, features and abilities of each person are different from others, and the same is the case for all other organisms.

This uniqueness also exists in nature's sensing systems. Even though the overall functionality and types of sensory systems within a species are similar, they differ in the detail, and so the exact characteristics of sensors in two different individuals are different. For instance, consider auditory sensing systems in humans. The overall structure and functionalities of auditory sensor structures are similar. However, the exact shape and structure of the outer ear (in Fig. 1.1) is unique for every person [18]. Ear canal morphologies are also different. The ways in which the outer ear and the ear canal modify sound waves are different for every person, resulting in unique ear drum vibrations. Hence, every person perceives the same sound signal in a slightly different manner. Similarly, the shape and texture of the tongue are also unique [19]. Even though taste receptors are distributed in a similar way, their exact spatial distribution on the tongue is different for every person. Also, the morphology of bumps and ridges on the tongue is unique, so the signature developed by taste receptors for a particular substance is unique to each person. Similarly, all sensors in nature have unique characteristics, and as the brain is tuned to these unique particular characteristics, it can accurately identify sensing quantity.

Most biological sensing systems are actually redundant, as they consist mainly of a large number of similar sensor elements with unique characteristics which act together to form a sensor array. This parallel sensing technique not only improves noise cancellation, for example, but it also helps sensory systems to function properly when one or more of the sensor elements is damaged [20]. Due to their different characteristics, the dynamic range of sensor elements in an array is different. Combining such sensor elements helps achieve high sensitivity over a wide bandwidth. One typical example is lateral lines in fish, in that certain fish and aquatic creatures have an array of hair cell sensors called 'lateral lines', which are used in schooling behavior, prey detection, flow profiling, navigation, etc. [8]. The numbers of hair sensors and its morphologies vary significantly between individuals and among populations within the same species [21]. Even in the same fish, the heights of the hair cells vary significantly, and the sensitivity and dynamic range of the each hair cell sensor depends on its height. There therefore exists an inverse relationship between height and dynamic range, whereby tall hair sensors provide high

sensitivity but saturate at relatively high velocities, whilst, on the other hand, short hair cells are insensitive to low-flow velocities but can detect high intensity flows. By combining sensors of different heights, lateral line sensors achieve high sensitivity over a wide range of flow velocities.

Unlike artificial sensors, sensors in nature have evolved though uncontrolled processes, which introduces random minor variations in sensor structures. For instance, it has been shown that morphological variations in lateral lines are entropic and there is no correlation between a hair cell's geometry and factors such as its position on the fish's body [21]. Similarly, variations in the outer ear and tongue are also random and are responsible for a set of unique sensor characteristics. This makes the sensor characteristics difficult to predict, model and duplicate; hence, sensors in nature are not only unique, but also unclonable.

1.4 Uniqueness and Unclonability in Artificial Sensors: A Literature Survey

When nature's sensing systems extract complex information, using sensors with unique and unclonable characteristics, the artificial sensor domain moves in the opposite direction. Engineers continue in an ongoing effort to make sensors more and more precise, and complex designs and advanced fabrication technologies have been developed for fabricating them with exactly the same characteristics. It is generally assumed that the accuracy of a sensing system depends on the precision of the sensor, but this is not actually true. Properties such as precision and linearity help to reduce the number of calibration steps. If the characteristics of the sensors are the same, the mapping functions that map the sensor's output to the measured quantity will also be the same. Therefore, different sensing systems can be developed with minimal calibration steps. Furthermore, it gives the flexibility of replacing sensors and associated circuitry without any calibrations. Similarly, linearity makes the mapping function simple, as linear functions can be implemented and processed with minimum resources. On the other hand, if the characteristics of sensors are different, mapping functions are different for each sensor, in which case, to make it accurate, each sensing system needs to calibrated separately, in order to generate a corresponding mapping function. As calibration is an expensive and particularly time-consuming process, the artificial sensor domain is focusing on developing sensors with exactly the same characteristics.

A few researchers have managed to mimic nature's concept of bandwidth improvement by combining sensors with different characteristics. The nature-inspired lateral line, reported in [22], uses an array of hair cell sensors with different heights, for flow measurement. By combining these sensor elements with different dynamic characteristics, the lateral line achieves high sensitivity over a large bandwidth. An artificial tongue has also been developed by using an array of nonspecific (unique) taste sensors [9]. Each sensor element in the array responds only to a specific compound. For a particular sample, the sensor elements that are sensitive to the compounds present in the sample respond, and the sensor array then generates a unique signature. An Artificial Neural

Network (ANN)-based algorithm is trained to identify the sample from its unique signature. The same concept has also been used in an artificial nose [10]. In all of these studies, the characteristics of the sensor elements are unique albeit not random. Similar to artificial sensors, they are precise and fabricated using complex technology. Sensors with the exact characteristics can therefore be duplicated and are not unclonable.

In the security domain, the unique and unclonable characteristics of devices are exploited. These features, their uniqueness, and unclonability are the basis of identification. In biometrics, unique and unclonable physical human characteristics, such as fingerprints, eye iris, heartbeats, ear-prints and tongue-prints, are used for identifying an individual [23]. Such authentication, based on physical characteristics, can provide better security than soft authentication (such as a password). Similarly, the unique and unclonable physical characteristics of devices including sensors are suitable for device identification and authentication. Ongoing research on this subject resides under the category 'Physical Unclonable Function' (PUF).

1.4.1 Physical Unclonable Function (PUF)

With the growing popularity of the Internet of Things (IoT), a large number of devices are connecting to public networks. The proper identification and authentication of these devices is a major security concern. The traditional method involves using a separate identifier along with the device. In most cases, the identifier is a secret code/key in protected memory. As many such devices are installed in remote, untrusted environments, they are vulnerable to direct physical attacks [24]; information even stored inside protected memories can be revealed by using techniques such as side-channel attacks, fault injunctions and microprobing. Once the secret code is known, the device can be easily duplicated. Such duplicated devices then have the potential to carry out various attacks, ranging from simple hacking to major terrorist attacks. Furthermore, secret code-based identification techniques require memory, which is an additional overheard and not feasible for many devices with limited memory and processing power.

The Physical Unclonable Function (PUF) is a simple, low-cost and superior alternative to memory-based identifiers. PUFs are functions based on physical characteristics which are unique, unpredictable and impossible to duplicate. Similar to biometrics, the PUF uses random physical variations inside the device as a 'signature' for identification. These variations can be either intrinsic within the devices or intentionally introduced during the fabrication processes [25]. A PUF block representation is shown in Fig. 1.2. It exhibits challenge-response behavior, in that when it is challenged with an external stimulus, called a 'challenge' (CH), it generates an output, called a 'response' (RS). Due to random physical variations, RS is unique for a particular PUF device, for a specific challenge. Some PUFs have only one challenge-response pair (CRP), while others have large numbers of CRPs [25]. The unique CRPs of a PUF can be used as an identifier which, based on structural uniqueness, has the following advantages.

1. As cloning a physical structure is much more difficult than cloning memory, PUF offers high-level security.

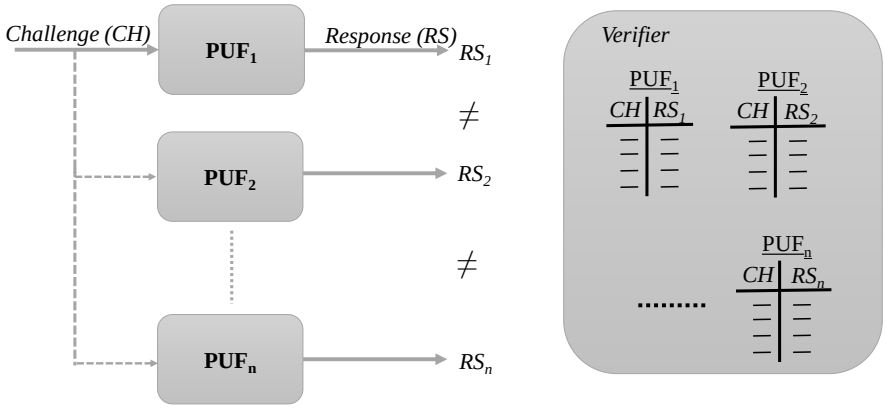

Figure 1.2: Block representation of Physical Unclonable Functions(PUFs)

2. No memory is required in the device, which helps reduce cost and complexity.

In security applications, PUFs are general employed in two different ways: For device identification and key generation [26]. For device identification, the verifier (authorizing party) initially records all available CRPs. During the device verification phase, shown in Fig. 1.3, the verifier sends one or a set of CH to the PUF, which then sends the corresponding RS back to the verifier. The verifier compares the RS with the value stored in memory. In the case of a positive match, the device's identity is authenticated. These types of PUF-based device identifications are deployed in smart cards [27], RFID tags [28], etc. Another potential application is PUF-based key generation, which is shown in Fig. 1.4. The idea is to split the secret key information and store one part as a PUF. During the enrollment phase (Fig. 1.4(a)), a pseudo key is generated by combining the PUF's response and the key. The pseudo key is then stored in the device. In the key reconstruction phase (Fig. 1.4(b)), the actual key is reconstructed by removing the PUF's response from the pseudo key. To reconstruct the key, both the activation code and device-specific PUF data need to be available. Hence, it is not necessary to store a pseudo key in protected memory. This type of key generation technique

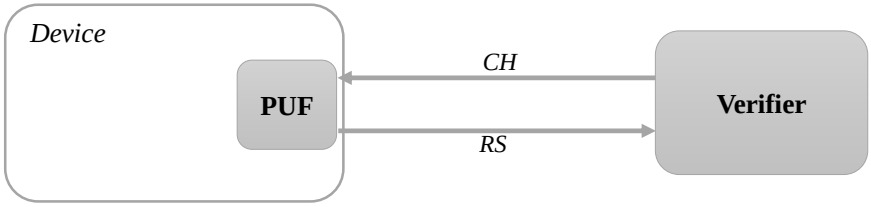

Figure 1.3: Block representation of lightweight device identification

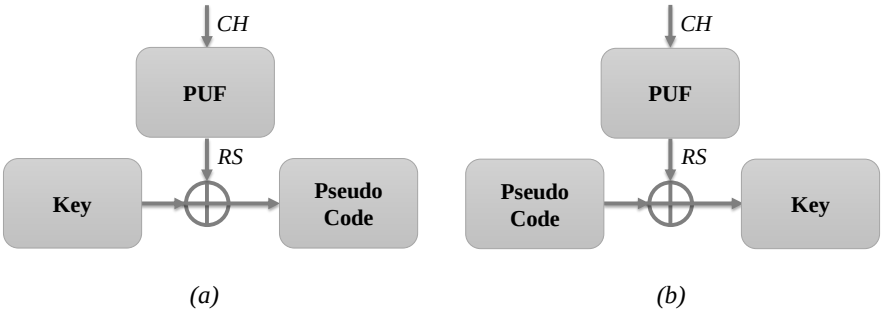

Figure 1.4: Block representation of PUF-based key generation. (a)Pseudo code generation (b)Key reconstruction.

is used in applications such as cryptographic algorithms [29], hardware-based software activation [30], and remote attestation protocols [31].

Different types of PUF realization have been proposed in the literature. Paper-PUF, reported in [32], uses microstructural variations in paper surfaces as identifiers, in order to prevent counterfeiting. These surface variations are measured from reflected light beams. Similarly, CD (compact disc)-PUFs measure random variations on CD surfaces. Uncertainties in silicon fabrication processes are also utilized for the development of PUFs, whilst delay-based PUFs use random delay variations in digital circuits for identification [33]. In a memory-based PUF, unique characteristics are derived from the unpredictable stable state of disabled memory cells [34]. Any variation in transistor offset voltage also has PUF characteristics [35]. In all of the PUF implementations discussed above, the source of the identifier is the random variations intrinsic within the devices. Such PUFs are called 'intrinsic PUFs'. On the other hand, a 'non-intrinsic PUF' requires additional fabrication steps, to insert random variations. The optical PUF discussed in [36] falls into this category and consists of a transparent layer filled with randomly distributed light-scattering particles. The reflection pattern of the light from the layer is unique and unclonable. Another non-intrinsic PUF, namely a coating PUF reported in [37], uses a layer with random dielectric patterns to generate a unique capacitance output. These random dielectric patterns are generated by randomly distributing TiO_2 and TiN particles in a aluminum phosphate layer.

1.4.2 PUF Sensor

In many applications, such as the military, transportation and health care, information from sensors is of critical importance. For instance, armed forces deploy MEMS sensors to track the use of their weapons [38]. Additionally, security agencies, including the UN (United Nations), need sensors to monitor various international research facilities [39], whilst in cars, ABS (Anti-lock Braking Systems) control units require information from different sensors, to decide on the breaking torque factor [40]. In such situations, as the data collected from the sensors are used to make a decision on further crucial actions,

the trustworthiness of the sensor and its data is a major concern. The verifier or the corresponding authorities need to guarantee that the information is from a specific sensor and not erroneous.

The common way to provide security to a sensing system is to use an additional cryptographic module along with the sensor, as shown in Fig. 1.5(a). Classical cryptographic techniques which are developed for computers cannot be implemented in sensor systems, due to their resources limitations. It has been shown that PUF-based security architectures are well-suited to low-cost, lightweight applications, including sensor systems [41]. In the security architecture shown in Fig. 1.5(a), the cryptographic module encrypts the sensor output using the PUF as a key. This encrypted information is then sent to the verifier, which authenticates and decrypts the information and then extracts sensor data, using the key. However, in this scheme, as the cryptographic module is separate, the system is vulnerable to direct sensor attacks, such as sensor tampering, the insertion of a malicious signal into the cryptographic module and in-authenticate sensor substitution. For instance, in a remote video surveillance system, an attacker can disconnect a CCTV (Closed Circuit Television) camera and inset any video signal into the cryptographic module. In [42], the authors discussed methods employed to insert bogus information into sensors, using intentional electromagnetic interference (EMI). Such attacks can inhibit pacing or induce defibrillator shocks in Cardiac Implantable Electrical Devices (CIEDs). Measurements from magnetic rotational sensors used by ABS systems can be easily corrupted using a simple external magnetic field, which in turn may cause life-threatening situations [40]. Furthermore, intentional sound waves can insert malicious signals into MEMS gyroscopes [43] used in many critical applications. The security model shown in Fig 1.5(a) does not have the ability to detect or prevent

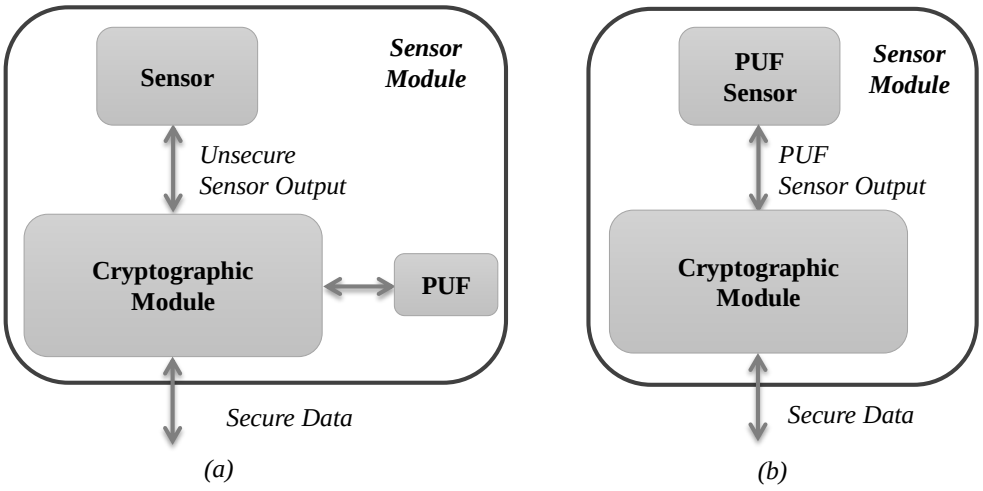

Figure 1.5: Block representation of secure sensor systems (a)using a separate PUF and (b)using a PUF sensor

this kind of direct sensor attack. In network connected sensors, the attacker can use it as weak entry point and gain some form of control over the system by manipulating the measurand.

A new architecture which extends the trust perimeter to the sensor is shown in Fig. 1.5(b). In this scheme, the unique and unclonable characteristics of the sensors are exploited to identify the sensor. Such sensors are called 'PUF sensors' and send the sensor output along with the PUF characteristics to the cryptography modules, which in turn use the PUF characteristics as an identifier to authenticate sensor output and/or derive the cryptographic key. In this scheme, as it is nearly impossible to duplicate PUF characteristics, the cryptographic module can detect and prevent direct sensor attacks.

The PUF sensor is a relatively new concept. All available PUF sensors can be divided into two different categories. The first category exploits random variations in several existing sensors, in order to derive PUF characteristics. In this scheme (shown in Fig. 1.6(a)), sensor identification and/or key generation are carried out in a separate $CH - RS$ cycle, before or along with the measurement. The sensor output ($f(m)$) is proportional to the measurand (m). Here, function $f(m)$ is the same for every sensor (not device-specific), only the CH-RS is unique. For instance, in [44], variations in impulse response and the inherent offset values of a commercially available accelerometer sensor are used as the PUF. The verifier/cryptographic module measures the offset value at 0g and/or impulse response and then it derives the cryptographic key. Similarly, [45] explores the possibility of using frequency modes, capacitances and quadrature signals of a gyroscope for generating cryptographic keys. The PUF signature is also derived from intrinsic variations in image sensors [46]. The second category uses conventional PUFs as a sensor. Here, the vulnerability of PUFs to parameters such as temperature, voltage and pressure, which is unwanted, is exploited to measure these parameters. The output of the PUF sensor ($f(m, CH)$) depends on the CH and the measurand m. Such PUF sensor implementations can be employed for the secure transfer of information over an untrusted channel, even without cryptographic modules [47]. In [48] and [49], voltage sensors exploiting the unwanted effects of voltage on a ring oscillator (RO) PUF and a glitch PUF are reported. Similarly, a PUF temperature sensor is prototyped, using an

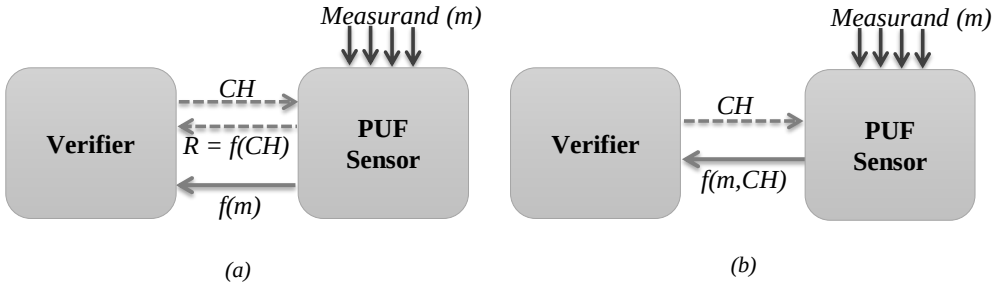

Figure 1.6: Block diagram showing two categories of PUF sensors: (a) an existing sensor is used as a PUF and (b) a conventional PUF is used as a sensor

XOR gate for the secure transfer of information over an untrusted channel [47]. The pressure sensitivity of an electrostatically actuated micro-electro-mechanical relay based NOT gates of RO PUFs is used for secure pressure measurement [50]. Another approach involves developing a dedicated, unique, and unclonable sensor, and then integrating it with a conventional PUF to form a PUF sensor. In this case, sensor design and fabrication process can be optimized to gain maximum variability. The optical PUF sensor reported in [51] is a unique and unclonable optical sensor array designed particularly for PUF sensor application. The sensor array generates unique and unclonable electrical signals when light falls on a layer with non-uniform transmittance. A conventional PUF integrated with a sensor array generates secret control logic for sensor array selection and summation. The output of the PUF sensor ($f(m, CH)$) depends on the CH given to the PUF and the intensity of light (m) on the optical signal.

1.5 Motivation

Sensors in nature are unique and unclonable. Even though researchers have mimicked various aspects, uniqueness and unclonability have not been explored to date. As already discussed, a few have tried to develop sensor arrays consisting of sensor elements with different characteristics for artificial noses, artificial ears and lateral lines; however, they have been clonable. This motivated to think about sensors with unique and unclonable characteristics (also referred as unique and unclonable sensor), as developing such sensors would result in the possibility of implementing different features of nature's sensing systems in an artificial domain.

In nature's sensing systems, the brain is tuned to the unique characteristics of sensors. Hypothetically, if such a sensor get replaced, the brain can identify it from differences in its characteristics. The sensor replacement also badly affects the sensing ability. In [52], researchers mimicked the ear replacement by modifying the shape of outer ear. The brain lost it ability to localize the sound. However, the hearing ability is regained though training. As the sensors in nature are unclonable, it is impossible to replace the sensors without the 'authorization' of the brain. The sensing system need to go through a training process in order to enrol the unique characteristics of the new sensor into brain. This incompatibility of nature's sensing systems can be exploited in artificial domain by developing sensors with unique and unclonable characteristic. If the verifier is tuned to the unique and unclonable characteristic of a particular sensor, the direct sensor attacks are impossible. The concept is similar to secure sensing module based on PUF sensor discussed in Fig. 1.5. Unlike PUF sensors, which use either minor random variations in already existing artificial sensors or a PUF device as a sensor, in unique and unclonable sensors, random variations are intentionally integrated into sensor structures to generate unique characteristics. This method does not require an additional challenge like PUF sensors. For unique and unclonable sensors, the measurand is the challenge and the sensor output is the response. Therefore, such sensors can also be used as PUFs with the measurand as a challenge. In all existing PUFs, the challenge is either a voltage signal or a light signal. A PUF with a different type of challenge can further expand the

possibilities of PUF devices.

Sensors with unique and unclonable characteristic also enable the development of sensor systems that are closer to nature's sensing systems, and those which use nonspecific sensors are far superior to artificial sensing systems. However, the capabilities of such systems are not yet fully known, so developing nature-like sensing systems, using unique and unclonable sensors, would help in understanding more about nature's way of sensing.

1.6 Objective

In this thesis, sensors with unique and unclonable characteristic, is introduced. Each sensor responds to a measurand and provides an output which is unique and different from other sensors. The unique characteristic of the sensor is difficult to duplicate. Such sensors can be used as sensor with an integrated identifier for developing highly secure sensing modules, as hardware identifiers similar to PUFs that respond to a measurand and provide sensor output as a response, and also as unique sensor elements for developing nature-like sensing systems.

The main objective of this thesis is to design and develop a unique and unclonable sensor which should have following characteristics:

- The sensor should respond to a measurand, tilt, and provide a capacitance output. Tilt is chosen here, because it can be applied easily, and without any complex system or direct contact. These features are advantageous when the sensor is used as a hardware identifier. The reasons for choosing capacitive sensing are discussed in Chapter 2 (Section 2.2.2).

- The sensor should have unique output characteristics. The overall output characteristics of the sensor may be similar, but the exact characteristics of each sensor should be different from the others. The goal is to maximize any differences in output characteristics (or uniqueness), which may make sensor identification easier.

- Similar to sensors in nature, random structural variations integrated into the sensor need to be the source of uniqueness. Such random variations are difficult to measure, model or duplicate, thereby making the sensor unclonable.

- The characteristics of each sensor should be repeatable. Each sensor should show the exact characteristics when the same measurand is applied multiple times. Various factors such as electromagnetic interference, environmental factors, and structural instability can cause drift in characteristics, and so the aim is to minimize these effects and achieve maximum repeatability.

- It is desirable to have high sensitivity, as it improves both the measuring capability and uniqueness of the sensor.

One important feature of a unique and unclonable sensor is that it should be developed using a simple fabrication process. Tolerances in the fabrication process introduce

random variabilities, which further improve the uniqueness and make sensor characteristics more unclonable. Hence, instead of using complex clean room technologies, a simple and cost-effective fabrication process needs to be developed. Furthermore, in present fabrication processes, it is only possible to develop sensors with the same characteristics in a fabrication cycle. The sensor design and fabrication process for the unique and unclonable sensor should allow the development of sensors with different characteristics in the same fabrication cycle.

1.7 Outline and Contributions of the Dissertation

Inspired by nature, sensors with unique and unclonable characteristic is proposed. The following chapters discuss the design and development of a capacitance-based, unique and unclonable tilt sensors and their applications in the artificial sensing domain.

Chapter 2 discusses the details of capacitive sensor with unique and unclonable characteristic, including sensor design, electrical modeling, simulation studies and prototype testing. A new capacitive electrode structure which can offer higher sensitivity and uniqueness to the sensor than the most commonly used interdigitated electrode structure is proposed. As sensor with unique and unclonable characteristic is a new concept, various parameters that are required to evaluate and compare the performances of such a sensor are defined in this chapter. A simple, cost-effective sensor fabrication method, developed for the proposed sensor, is also presented. This chapter also discusses various factors in the proposed sensor that will contribute to its uniqueness and unclonability, and optimization of these factors.

In **Chapter 3**, the design, modeling, simulation, fabrication and testing of a differential capacitive sensor with unique and unclonable characteristic are presented. The differential capacitive sensor is an extension of the capacitive sensor discussed in Chapter 2. This chapter mainly discusses about how the differential electrode arrangement proposed herein reduces unwanted offset capacitance and improves uniqueness, unclonability and sensitivity, compared to the dual-electrode arrangement in Chapter 2.

In **Chapter 4**, the fabrication of soft-thin conductive PDMS (CPDMS) membranes, which is used as an active functional element in miniaturized capacitive sensor (discussed in Chapter 5), is presented. This chapter mainly discusses the effect of conductive filler (Carbon black) concentration on the electrical and mechanical characteristics of CPDMS membrane, and it begins with a discussion on the current state of the art. Different methods used as part of this research for the preparation of a CPDMS composite are discussed and compared, and a simple fabrication method for thin membranes is then presented. Details on the set-ups developed for electrical and mechanical characterization, testing procedures and results are also given.

A miniaturized capacitive sensor design that can offer high uniqueness and unclonability at a reduced size is proposed in **Chapter 5**. The optimization of the sensor's structure, its dimensions and electrode structure is carried out using analytical modeling and simulations. In this chapter, the differences between single and dual capacitive electrode configurations, and square and circular membrane deflections, are discussed

in great length. The fabrication of sensor prototypes, their testing, and results are also presented.

In **Chapter 6**, applications for the proposed sensors with unique and unclonable characteristic are presented. Various possibilities in this regard, including as a PUF identifier, an identification sensor, and a sensor for developing nature-like systems, are discussed in detail.

The thesis concludes in **Chapter 7**.

Bibliographic Note

Some content from each of the chapters appears in the patent [53]. Portions of Chapter 2, Chapter 5, and Chapter 4 appear in the papers [54], [55] and [56]- [57], respectively. Portions of Chapter 3 appear in the papers [58] and [59].

2 Capacitive Sensor with Unique and Unclonable Characteristic

2.1 Introduction

In this chapter, the design and development of capacitive sensors with unique and unclonable characteristic are presented. The sensor responds to mechanical parameter tilt and provides a corresponding capacitance output. Similar to sensors in nature, the exact characteristic of each sensor are unique and different from one another, and random variations in a sensor's structure are the sources of its uniqueness. Hence, unique sensor characteristics are also unclonable, i.e. difficult to predict, model, or duplicate.

2.2 Sensor Design

The proposed sensor consists of a spring-mass-damper (inertial) system as the functional element. The functional element has unique and unclonable characteristic. Random variations, intentionally integrated into the functional element, render its characteristics unique and difficult to clone. The functional element deflects under the influence of external forces such as tilt, pressure and acceleration, and owing to unique characteristic, the functional element deflection of each sensor is unique and slightly different from the others. A suitable sensing mechanism converts this deflection into a unique output signal.

2.2.1 Functional Element

In this sensor design, shown in Fig. 2.1, a PDMS (polydimethlysiloxane) structure filled with conductive balls acts as the functional element. The conductive balls are randomly distributed inside the PDMS structure, which leads to the unique spatial arrangement of the conductive balls and results in a unique mass distribution on the functional element. Owing to the unique mass distribution, the deflection of each functional element is slightly different from the others. This function element design is motivated by previous work [60].

2.2.2 Sensing Element

A suitable sensing mechanism is required to convert the functional element deflections into electrical form. In the proposed sensor design, capacitive sensing is chosen because:

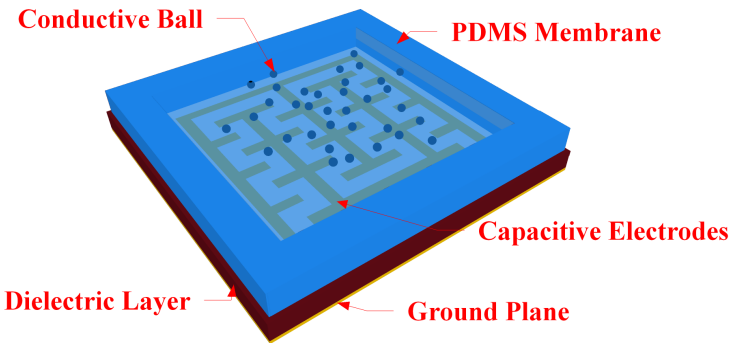

(a)

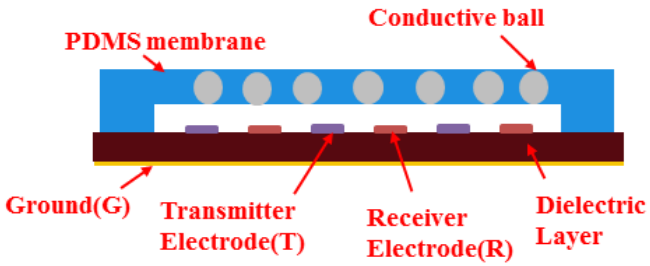

(b)

Figure 2.1: Diagram of the proposed capacitive sensor with unique and unclonable characteristic. (a) 3D view. (b) 2D Cross-sectional view

- It is a non-contact sensing technique. Capacitive electrodes can sense functional element deflections without any direct contact.
- In addition to the unique deflection of the membrane, capacitive electrodes can detect uniqueness introduced by the spatial arrangement of conductive balls which modify the electrical field lines between the capacitive electrodes. The unique spatial arrangement of these conductive balls leads to a unique electrical field pattern, which thereby results in unique sensor capacitance. The unique membrane deflection characteristic (mechanical uniqueness) along with the unique electrical field pattern (electrical uniqueness) are expected to improve the uniqueness and unclonability of the sensor.
- Capacitive sensors can detect both metals and dielectrics. As the functional element consists of both metals (conductive balls) and dielectrics (PDMS), capacitive sensing is expected to provide higher sensitivity and uniqueness.
- Capacitive electrodes are simple to fabricate. Two conductive plates, or in some cases even a single plate (single/grounded electrode capacitive sensors [61]) can form the electrode structure.

- The capacitive sensing principle is well accepted in the industry, as it is rugged, low power and less sensitive to temperature [62].

Capacitive electrode structure

In capacitive sensors, two plates, called a 'transmitter electrode' (T) and a 'receiver' electrode (R), arranged either in parallel or in planar configuration, form the electrode structure. Applying a voltage between T and R generates an electrical field. The measurand (measuring quantity) modifies the electrical field and changes capacitance between T and R. In a parallel electrode configuration, shown in Fig. 2.2(a)(i), the electrical field is confined between two parallel electrodes, and the sensing area is restricted between electrodes T and R. In the case of planar electrode configurations, both electrodes are in the same plane, which generates a fringing electrical field—as shown in Fig. 2.2 (a)(ii). The planar electrode configuration does not restrict the sensing area, and it allows measurement with a single side access. These features make planar electrodes attractive for sensing applications such as dielectric measurement, human proximity detection and

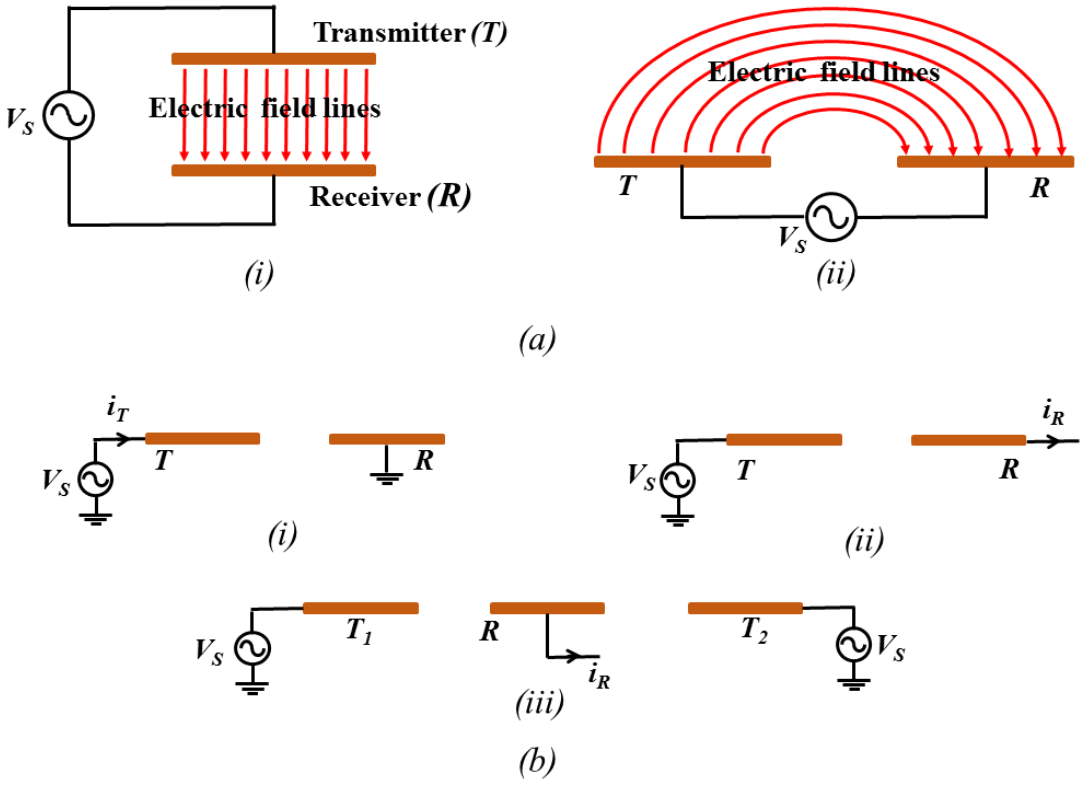

Figure 2.2: Different capacitive electrode configurations: (a) (i)Parallel electrode, (ii)planar electrode. (b) (i)single-electrode, (ii)dual-electrode, (iii)differential electrode.

touch sensors [63].

A capacitance measurement circuit converts electrode capacitance into a voltage or a current signal. Depending on the measurement principle, capacitive electrodes can be classified further as single/grounded electrode, dual-electrode and differential electrode configurations [63], all of which are illustrated in Fig.2.2 (b). In the single-electrode configuration (in Fig. 2.2 (b)(i)), a constant voltage source (V_S) excites T, and R is grounded. Capacitance between T and R is measured using transmitter current i_T. The problem with single-electrode configurations is that all the grounded planes near T act as R, whilst i_T is proportional to capacitance between T and the nearby grounded planes. Therefore, while designing an electrode structure, proper attention should be given to avoiding the effects of unwanted ground planes. On the other hand, the dual-electrode configuration (in Fig. 2.2 (b)(ii)) requires two electrodes. Here, the V_s is connected to T, and electrode capacitance is measured from receiver current i_R. Unlike the single-electrode configuration, the dual-electrode version measures capacitance between two specified terminals. Unwanted voltage sources near to R cause interference, but such unwanted effects can be removed easily by using modulation techniques [61]. The differential electrode configuration shown in Fig. 2.2 (b)(iii) is an extension of a dual-electrode configuration and consists of two transmitter electrodes, namely T_1 and T_2 and an R. Sensor capacitance is the difference between capacitances of T_1 and R (C_{T1R}) and T_2 and R (C_{T2R}). The electrodes are arranged in such a way that C_{T1R} and C_{T2R} vary in a push-pull manner, in which case taking the differential measurement increases sensitivity and cancels out any unwanted effects common to both capacitances.

In the capacitive sensor discussed in this chapter, a planar dual-electrode configuration is used. Two different electrode structures, shown in Fig. 2.3, are considered. Fig. 2.3(a)

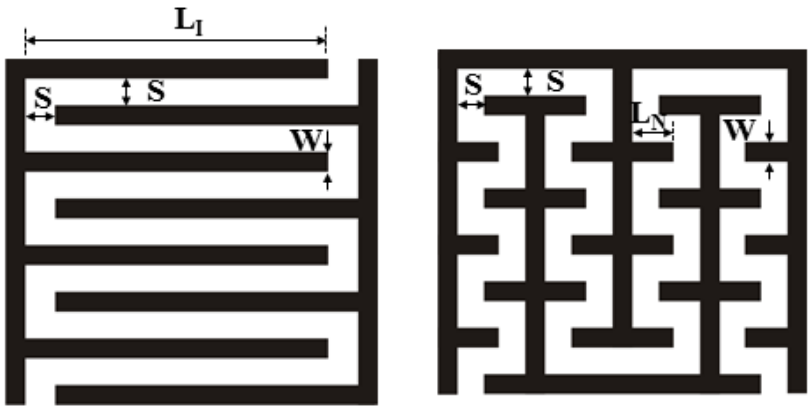

(a) (b)

Figure 2.3: Schematic of (a) Interdigitated Electrode(IDE) (b) Improved electrode structures used in capacitive sensor. Dimensions: $L_I = 9.20$ mm, $L_N = 1.15$ mm, $S = 0.80$ mm, $W = 0.60$ mm.

represents an interdigitated electrode structure (IDE). The IDE is the widely used planar dual-electrode structure for capacitive sensors because of its properties such as single-side access, a simple structure, the easy control of signal strength and imaging capability [64]. An improved electrode structure, which is expected to offer higher uniqueness and higher sensitivity to the proposed sensor, has also been also designed, as shown in Fig. 2.3(b). The idea is to increase corners in the electrode structure. As electrical field intensity in the corners is higher, there are more high-intensity spots in the sensing area above the electrode structure. Therefore, capacitance of the electrode structure is more sensitive to the conductive ball arrangement, and the sensor is expected to offer high uniqueness.

2.3 Sensor Modeling and Analysis

In order to analyze the proposed sensor design, an electrical model for the sensor was developed, a detailed diagram for which is shown in Fig. 2.4. To simplify the model, only a pair of transmitter (T)-receiver (R) electrodes and a single ball are considered. The excitation signal V_S and current-to-voltage converter (I to V), built around an operational amplifier (OA), are the components for the dual-electrode measurement set-up. When T is excited with V_S, an electrical field builds up from T to R. The functional element (PDMS filled with a conductive ball) modifies the electrical field. The PDMS structure is a dielectric insulator, while the conductive ball is a floating electrode (F). The sensor capacitance C_S between T and R is a combination of different capacitances—those which contribute to C_S are shown in Fig. 2.4. Consider the functional element is at the null position (zero deflection). C_{TF} and C_{FR} represent capacitances between terminals T and F and terminals F and R, respectively. The electrical field, below the electrode structure, through the dielectric layer introduces C_{TR}. A ground plane (G) is provided to confine these electrical fields within the sensor's structure, and G also nullifies the effect of external interference on sensor capacitance. C_{FG} is the capacitance between F and G, C_{TG} is capacitance between terminals T and G, and C_{RG} is the capacitance between R and G. As the conductive balls are randomly distributed, the ball's position and in turn C_{TF}, C_{FR}, and C_{FG} are different for each sensor structure. Sensor

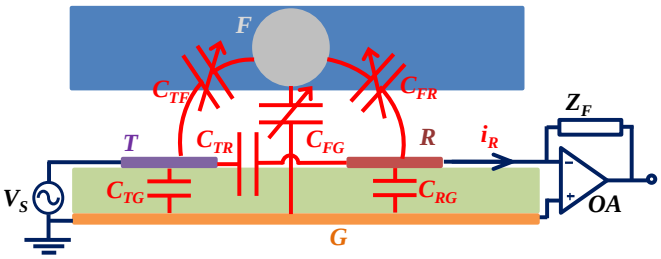

Figure 2.4: Detailed diagram showing a portion of the capacitive sensor. Various individual capacitances that contribute to sensor capacitance (C_S) are shown.

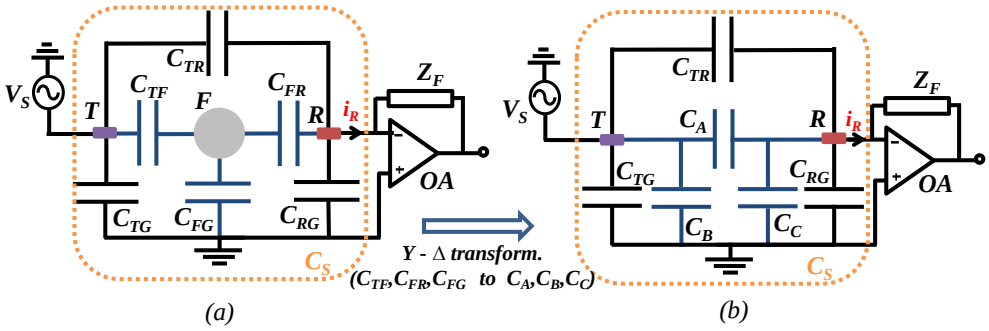

Figure 2.5: Electrical equivalent diagram of the capacitive sensor with a dual-electrode measurement set-up. (b) Electrical equivalent diagram after applying Y-Δ transformation

capacitance C_S is measured using the receiver current i_R, while the I to V converter transforms i_R into a measurable voltage signal.

The electrical equivalent diagram for C_S is shown in Fig. 2.5(a). C_{TF}, C_{FR} and C_{FG} form a Y-network. To simplify the calculations, a Y-Δ transformation is applied and the resulting circuit is shown in Fig 2.5(b). Capacitors C_A, C_B and C_C in Fig. 2.5(b) can be expressed as:

$$C_A = \frac{C_{TF}C_{FR}}{C_{TF} + C_{FR} + C_{FG}} \tag{2.1}$$

$$C_B = \frac{C_{TF}C_{FG}}{C_{TF} + C_{FR} + C_{FG}} \tag{2.2}$$

$$C_C = \frac{C_{FR}C_{FG}}{C_{TF} + C_{FR} + C_{FG}} \tag{2.3}$$

As seen in Fig. 2.5(b), C_{TG} and C_B are parallel to V_S, which supplies the current required for these capacitors. Hence, the receiver current, i_R, is independent of C_{TG} and C_B. Similarly, C_{RG} and C_C are connected across the inverting and the non-inverting terminals of OA. As the inverting terminal is at floating ground potential and the non-inverting terminal is grounded, no current flows through C_{RG} or C_C. Under these conditions, C_S can be represented as:

$$C_S = C_{TR} + C_A \tag{2.4}$$

where

$$C_A = \frac{C_{TF}C_{FR}}{C_{TF} + C_{FR} + C_{FG}} \tag{2.5}$$

The deflection of the functional element, due to the measurand, changes C_A. Its deflection towards the electrode structure increases C_{TF}, C_{FR} and C_{FG}, and C_A increases.

Similarly, the deflection of the functional element away from the electrode decreases C_A. C_S can be expressed as:

$$C_S = C_{TR} + C_A \pm \Delta C_A \tag{2.6}$$

From Equation (2.6), sensor capacitance is a parallel combination of the fixed component ($C_{TR} + C_A$) and the variable component ΔC_A. ΔC_A varies in line with the membrane movement and contains information about the measurand. $C_{TR} + C_A$ is a fixed, unwanted capacitance called 'offset capacitance' (C_{OS}). In this design, $C_{TR} + C_A >> \Delta C_A$. In capacitive sensors large offset capacitance can reduce the sensitivity of sensor systems, more details for which are given in Chapter 3, and so it is desirable to have less offset capacitance. In this sensor structure, the only way to decrease C_{OS} is to reduce the distance between T and G (using a thin dielectric layer). Under this condition, a large part of the electrical field contributing to C_{TR} is drawn towards G, which decreases fixed component C_{TR} in C_{OS}. However, the thin dielectric layer also reduces the distance between F and G, which in turn increases the capacitance C_{FG}. From Equation (2.5), an increase in denominator variable C_{FG} reduces the sensor sensitivity. Hence, in the proposed sensor design, in order to reduce offset capacitance, sensitivity needs to be sacrificed.

2.4 Simulation Studies

Various aspects of capacitive sensors with unique and unclonable characteristic have been verified using Finite Element Analysis (FEA). A commercially available software package, COMSOL Multiphysics, was used for this analysis. The proposed sensor transforms the movement of a PDMS structure filled with conductive balls into a change in capacitance. Sensor modeling requires solving both structural mechanics and electrostatics equations, and COMSOL offers an electromechanics module in this regard. The dimensions of the sensor models used in the simulations are given in Fig. 2.6. Selected

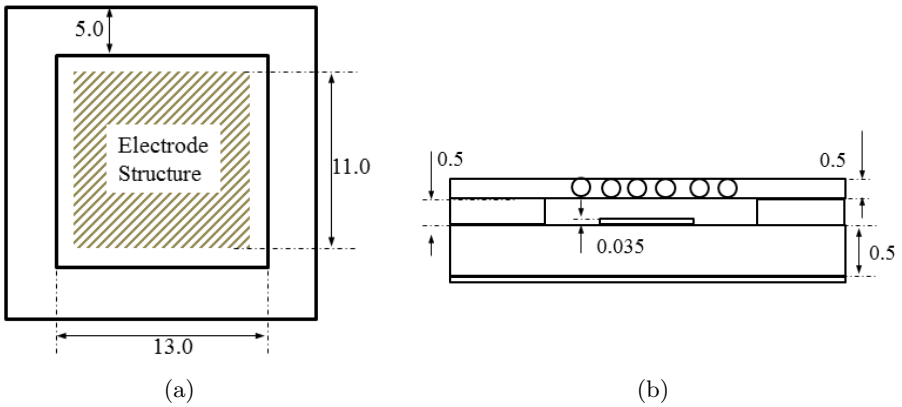

Figure 2.6: Sensor Dimensions (im mm)(a)Top view. (b)Cross-sectional view.

Table 2.1: FEA simulation details

Description	Material	Domain	Boundary
Active Element	PDMS	Linear Elastic Material, Gravity	
Distance Holder	PDMS	Linear Elastic Material, Gravity	Fixed Constraint
Electrodes	Copper		Terminal
Conductive Balls	Steel AISI 4340	Linear Elastic Dielectric, Gravity	Floating Potential
Dielectric Layer	FR4	Linear Elastic Dielectric	Fixed Constraint

materials, domain and boundary conditions are in Table 2.1. Details of the simulations and the results are discussed in the following sections.

2.4.1 Electrode structures: Interdigitated and improved

Three-dimensional models of the proposed sensor with IDE and an improved electrode were developed in COMSOL. In this model, the distance holder thickness (t_d), the active element thickness (t_a), and the conductive ball diameter (d_b) were 1.0 mm. In order to compare the sensitivity of electrode structures, a pressure load was applied to the sensors with IDE and the improved electrode. Pressure in a range of 0-100 Pa was applied to the functional element, and the sensor models were meshed and simulated. A slice plot, showing electrical field intensity, at a distance of 0.03 cm from both electrode structures,

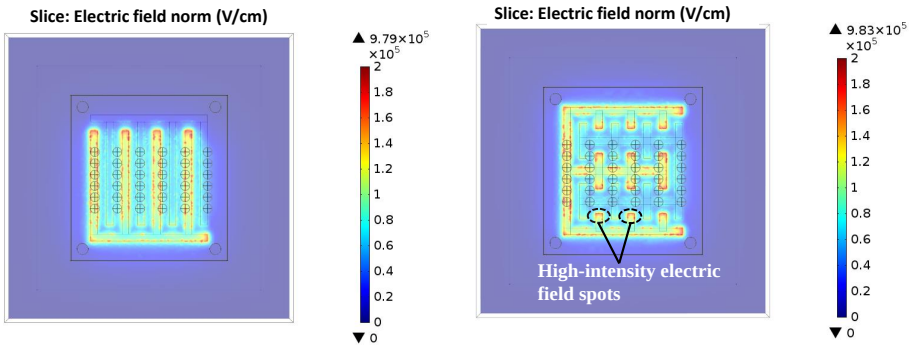

(a) (b)

Figure 2.7: Slice plot showing the electrical field intensity, at a distance of 0.03 cm from the (a)Interdigitated Electrode (IDE) structure. (b)improved electrode structure.

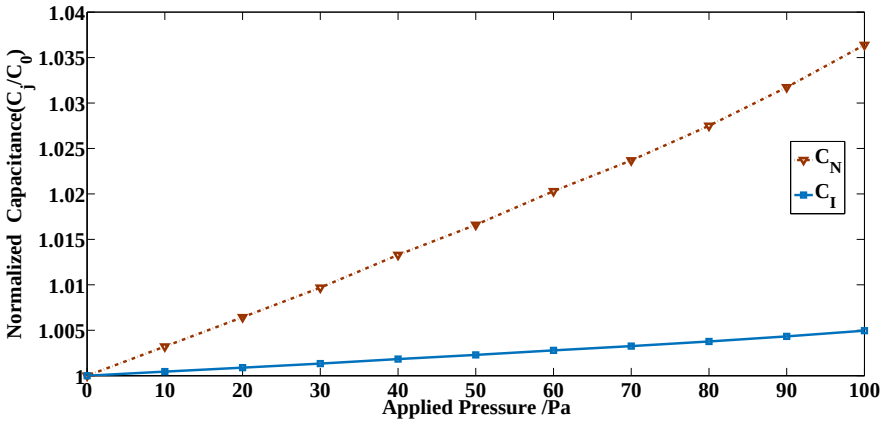

Figure 2.8: Normalized capacitance recorded from sensors with IDE (C_I) and an improved electrode (C_N) when simulated for pressure load.

when the applied pressure is 0 Pa, is illustrated in Fig.2.7. The improved electrode structure has more high-intensity electrical field spots on the edges and at the center of the electrode. At 0 Pa, functional element deflection is zero. capacitance observed at 0 Pa (C_0) is the offset capacitance of the sensor structure. The sensor with IDE and an improved electrode show C_0 of 1.120 pF and 0.9153 pF, respectively. With the increase of pressure, the membrane moves closer to the electrode structure, which thereby increases the sensor capacitance. The normalized capacitance value (normalized to C_0) recorded from the sensors with IDE (C_I) and the improved electrode (C_N) structures are plotted in Fig.2.8. The sensor with an improved electrode shows better performance.

2.4.2 Effect of the ground plane

In order to verify the effect of the ground plane on sensor sensitivity and offset capacitance, 2D structures of the proposed sensors were simulated. Three sensors with dielectric thicknesses (t_i) of 0.1 mm, 0.5 mm and 1.0 mm were simulated for a pressure load. All other sensor dimensions and simulation parameters remained the same. The normalized capacitance (normalized to C_0) recorded from the simulations is plotted in Fig. 2.9. The sensors with t_i = 1 mm, 0.5 mm and 0.1 mm showed C_0 of 1.45 pF, 0.73 pF and 0.35 pF, respectively. As expected, the offset capacitance (C_0) of the sensor capacitance reduces in line with a decrease in t_i, but the decrease in t_i affects sensor sensitivity [1].

Unlike other sensors, the sensor with t_i = 0.1 mm showed different behavior. After 60 Pa, sensor capacitance started to saturate, and when applied pressure exceeded 140 Pa, sensor capacitance started to decrease. This effect can be explained with the help of Fig. 2.10. As the dielectric layer is thin, the value of C_{FG} is higher than for sensors with thicker t_i. However, at low pressures, C_{TF} and C_{FR} are dominant. With the increase

[1]The slope of the plots in Fig. 2.9 represent sensitivity.

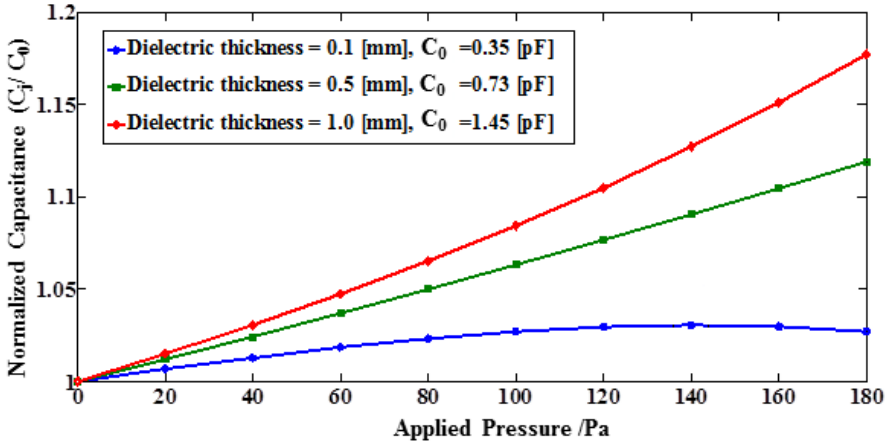

Figure 2.9: Normalized capacitance recorded from the sensor with dielectric thicknesses (t_i) of 0.1 mm, 0.5 mm and 1.0 mm for pressure load.

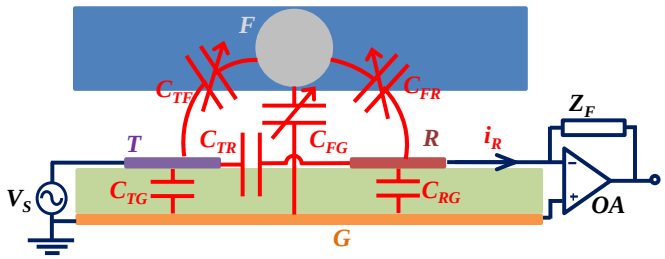

Figure 2.10: Various individual capacitances that contribute to sensor capacitance (C_S) are shown.

of pressure, the functional element moves closer to the electrode structure, and C_{FG} then starts to dominate, following which sensitivity starts to decrease. After a certain point, when the membrane moves further towards the electrode, the increase in C_{FG} is much greater than the increase in C_{TF} and C_{FR}. Under this condition, from Equation (2.5), sensor capacitance decreases in line with an increase in pressure. Further studies, discussed in later sections, show that capacitive sensors operating near this region have maximum uniqueness and sensitivity.

2.4.3 Sensor Uniqueness

The objective of this study was to verify the effect of random conductive ball distribution on sensor output. Six sensor models (SM_1 - SM_6) with different conductive ball distributions were simulated in COMSOL Multiphysics. The ball distributions are shown in Fig. 2.11. The number of conductive balls and their sizes in all SMs were the same (36

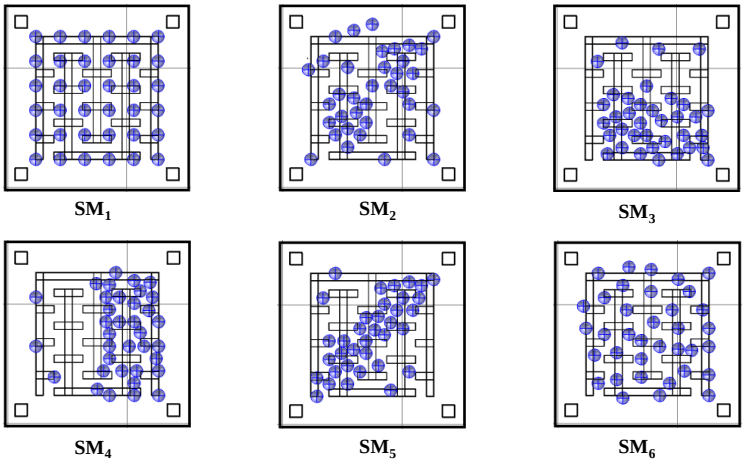

Figure 2.11: Conductive ball distributions in the six sensor models (SMs)

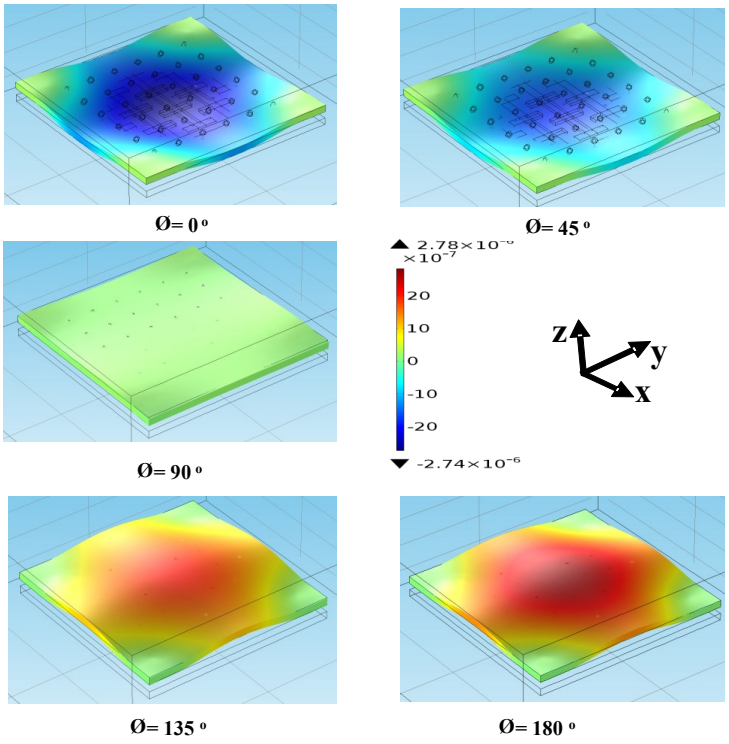

Figure 2.12: Shows the functional element deflection of SM_1 for different tilt angles. For better visualization, deflections are magnified 50 times

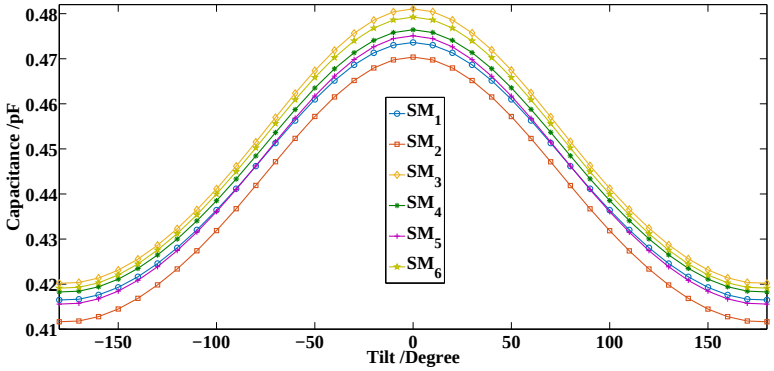

Figure 2.13: Sensor capacitance recorded from the capacitive sensors SM_1 - SM_6 at different tilt angles

conductive balls 0.5 mm in diameter), and only the spatial arrangement was different. In SM_1, the balls were arranged evenly, whereas in the other five models (SM_2- SM_6) the balls were randomly distributed. The thicknesses of the distance holder (t_d) and the active area [2] of the SMs were both 0.5 mm. The improved electrode structure (discussed in Section 2.2.2) was used. SMs were simulated for tilt, which was applied to the PDMS structure, thereby varying gravity components. In order to simulate tilt along the X-axis, Z and Y components of the gravity load were set to -9.8$\times \cos\theta$ and 9.8$\times \sin\theta$, respectively, and then θ (tilt angle) was varied from -180^o to +180^o. The Z component of gravity deflected the functional element (active area) perpendicular to sensor structure (Z axis). The Y component of gravity tended to move the functional element in a direction parallel to the sensor structure, although the clamped sides restricted this movement. Functional element deflection is proportional to the Z component of gravity and the effect of Y component is negligible. The deflection of the functional element for different tilt angles is shown in Fig. 2.12. At 0^o, as the Z component of gravity is at its maximum, the functional element is closer to the electrode structure with a maximum deflection in the negative Z direction. With tilt (clockwise or anticlockwise), the membrane moves away from the electrode. At $\pm$90^o the membrane is at the null position, i.e. functional element deflection is negligible. Further tilting moves the functional element away from the electrode, with a deflection in the positive Z-axis. The maximum deflection in the positive Z direction is seen at $\pm$180^o. Capacitances recorded for all SMs (SM_1 - SM_6) are plotted in Fig. 2.13. The SMs show maximum capacitance at 0^o. With an increase in the tilt angle, capacitance decreased and minimum capacitance was observed at 180^o. In each SM, even though the number and size of the balls were same, it's distribution was different. Owing to this difference in ball arrangements, the deflection of the functional element and electric field pattern of each SM were different. Hence, each SM showed different output characteristics. This study demonstrates that only the random distribution of conductive balls in the functional element can introduce measurably unique characteristic to sensor output. Fabrication tolerances are expected

[2] Flexible part of the PDMS structure (above the electrode) which actively takes part in sensing.

to improve this uniqueness even further, during prototype development.

2.5 Sensor Fabrication

In unique and unclonable sensors, fabrication tolerances are another source of uniqueness and unclonability. Therefore, commonly used tight tolerance fabrication processes [65], which involve clean rooms and expensive equipment, are not required for such sensors. Instead, a sensor with unique and unclonable characteristic is developed by using a simple and cost-effective fabrication process. It is also possible to develop multiple sensors with different characteristics in the same fabrication cycle.

The steps followed for the fabrication of capacitive sensors with unique and unclonable characteristic are shown in Fig. 2.14. In the sensor, the PDMS structure with conductive balls is the functional element. The PDMS, in its base form, consists of two liquid components, namely a base component (BC) and a curing agent (CA). A flexible, solid structure can be formed by adding a small amount of CA to the BC. In this fabrication process, two types of PDMS are used: Sylgard 184 [66] and Alpa-Sil Classic [67](referred to in this thesis as 'soft PDMS'). Sylgard 184 is the most popular PDMS. Different literature works discussing various properties of Sylgard 184 are available. The other PDMS Alpa-Sil classic is a softer and low-cost alternative. Alpa-Sil Classic has a Young's modulus of 250 KPa, which is much softer than Sylgard 184 (with Young's modulus of 2000 KPa). The sensitivity of the sensor depends on the stiffness of the functional element. A PDMS with a low stiffness (low Young's modulus), however, can offer better sensitivity, so the soft PDMS Alpa-Sil Classic was used to fabricate the functional element. On the other-hand, Sylgard 184 was used as a structural element for the fabrication of the master mold.

Fig. 2.14(a) shows the fabrication of the functional element. Two soft PDMS membranes, a distance holder and an active element (a membrane with randomly distributed conductive balls), were stacked together to form the functional element. Both membranes were fabricated using a master mold, which confined the soft PDMS composite within a space between the substrate and the spacer and forms the membrane. A copper plate, cut in the shape of a 4-inch wafer, served as a master mold substrate. As a result of the poor adhesion characteristics of copper, fabricated membranes can easily be peeled off from the copper substrate. A layer of Sylgard 184 acted as the spacer. The Sylgard 184 composite (mixed BC and CA in ratio 10:1) was spin-coated onto the copper substrate and kept in an oven for 30 minutes at a temperature of 100 ^{o}C, to form the spacer. After curing, a rectangular part, 5 cm $\times$ 2 cm in size, was carefully removed from the PDMS spacer. This partially removed part served as the master mold for the soft PDMS membrane fabrication. The soft PDMS composite was prepared by mixing Alpa-Sil Classic BC and CA in a ratio of 10:1. The composite was deposited into the mold. Excess soft PDMS composite was then carefully removed with the help of a knife. The curing time for Alpa-Sil classic is about 15 minutes, so structuring had to be done immediately after preparing the composite. In an active membrane element, conductive balls were randomly distributed before curing. A mask was used to limit the

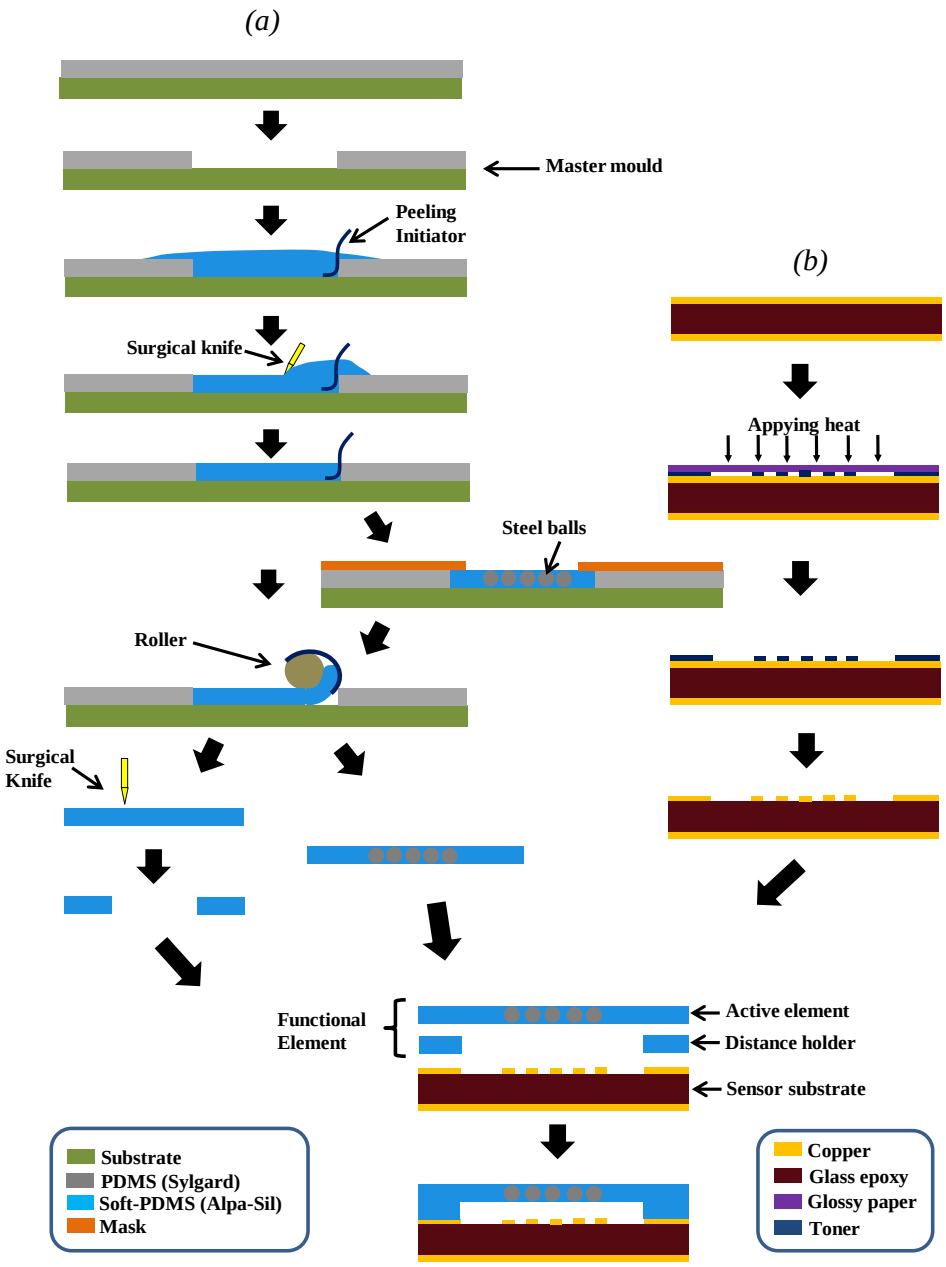

Figure 2.14: Illustration of the fabrication process for a capacitive sensor with unique and unclonable characteristic . (a) Functional element fabrication. (b) Substrate fabrication.

ball distribution within a specified region on the active membrane that contributes to the sensing process. From another fabricated membrane a rectangular part was removed which served as the distance holder. The thicknesses of the membranes were same as the spacer thickness. During membrane fabrication a piece of rectangular Scotch Tape was placed under the soft PDMS on the edge of the mold, which acted as a peeling initiator to help initiate membrane peeling which continued with the help of a soft roller (made of PDMS). The use of a peeling initiator and roller can reduce strain on the membrane, thus helping prevent breakage during peeling. It also prevents wrinkling and helps store the membrane without any contamination.

The capacitive electrode structure was fabricated on one side of a double-sided printed circuit board (PCB). The fabrication process is shown in Fig.2.14(b). The electrode structure was printed on glossy paper, using a laser printer. This glossy paper was kept above the PCB, with the printed side facing the copper layer. The PCB along with the glossy paper passed though a laminating machine, the heat and pressure from which transferred the electrode structure printed on the glossy paper to the copper layer. The copper layer was etched using an iron sulfate solution. During etching, the printed electrode structure on the copper layer served as a protective coating. The etching solution removed all copper except for the layer below the protective coating and formed the electrode structure. The protective coating was then removed, using acetone. The PCB, with an electrode etched on one side and a copper plate on the other side, served as a sensor substrate.

The three layers—the active element, the distance holder and the sensor substrate– were aligned manually and bonded together, using PDMS, to form the sensor.

2.6 Sensor Parameters

The parameters required to evaluate and compare the performances of capacitance-based unique and unclonable sensors are discussed in this section.

1) **Offset capacitance (C_{OS})**: Offset capacitance (C_{OS}) represents the fixed capacitance of the electrode structure when the functional element is at the null position (or zero deflection). In case of tilt, functional element deflection is at its minimum at $\pm 90^o$ tilt. However, there is a slight difference in capacitance at $+90^o$ and -90^o, due to random ball distribution. Capacitance at $+90^o$ tilt is considered as C_{OS}. This fixed offset value does not contain any measurement information and reduces the sensitivity of the entire sensing system. Hence, it is desirable to have a minimum C_{OS}.

2) **Maximum capacitance variation (ΔC_{max})** : The proposed sensor shows maximum capacitance at 0^o (C_0) tilt and minimum capacitance at 180^o (C_{180}) tilt. ΔC_{max} is the difference between C_0 and C_{180}. In addition, ΔC_{max} is proportional to sensor sensitivity. The objective is to achieve a maximum ΔC_{max}.

3) **Concordance correlation coefficient (ρ_c)**: The concordance correlation coefficient (ρ_c) is defined to measure the uniqueness and reliability of the proposed sensor. Uniqueness represents how effectively a sensor can identify among the group of other sensors, while reliability shows the ability of a sensor to reproduce the same output.

In devices such as PUFs, uniqueness and reliability were measured in terms of Hamming distances [68], i.e. the minimum number of substitutions required to transform one string to another. Such techniques which are more suitable for measuring the uniqueness of static digital PUFs cannot applied to analog sensor outputs. Therefore, methods such as a paired T-test [69], a Bland-Altman plot [70] and correlation coefficients [71], which are normally used to compare similarities between two measurement devices, measurement methods, etc., are considered for deriving uniqueness and reliability parameters. A paired T-test only checks whether the mean responses are the same, in which case means can be equal even when there are random variations; hence, the paired T-test is not the best choice. A Bland-Altman plot is a simple and efficient technique employed to determine how well two results match. However, any similarity needs to be derived from a graph, and a single value cannot be produced. Calculating correlations is an excellent tool for comparing (dis)similarities between two signals, as the correlation coefficient represents a single value of similarity. Its values vary from -1 to 1, and the higher the coefficient value, the more the similarity. Nonetheless, an ordinary correlation coefficient is independent of scale and bias. In order to overcome this disadvantage, Lin's proposed concordance correlation coefficient [72] is used to measure the uniqueness and reliability of the sensors with unique and unclonable characteristic. The concordance correlation coefficient between two variables can be calculated as:

$$\rho_c = \frac{2\rho\sigma_x\sigma_y}{{\sigma_x}^2 + {\sigma_y}^2 + (\mu_x - \mu_y)^2} \tag{2.7}$$

where μ_x and μ_y are the means and σ_x and σ_y are the variances of the variables. ρ is the correlation coefficient between the variables.

In order to identify a sensor from its characteristic, for the same input (or measurand) the output characteristic of each sensor should be measurably different from the others. On the other hand, each sensor should show the exact characteristic when the same input is applied multiple times. Practically, different environmental factors such as changes in temperature or humidity affect the reliability of the sensor. To evaluate uniqueness and reliability, the parameters 'inter-concordance correlation coefficient' ($inter-\rho_c$) and 'intra-concordance correlation coefficient' ($intra-\rho_c$) are defined. $Inter-\rho_c$ measures any (dis)similarity in the sensor characteristics of different sensors for the same excitation. $intra-\rho_c$ measures (dis)similarities in sensor characteristics when the same sensor is excited multiple times. $inter-\rho_c$ represents uniqueness, while $intra-\rho_c$ shows reliability. The objective is to maximize $intra-\rho_c$ (best value is 1) and minimize $inter-\rho_c$ (best value is 0).

4) C_{OS} **Spread**: The C_{OS} spread measures the extent of C_{OS} variations among a group of sensors, due to random ball distribution. C_{OS} Spread is the difference between the maximum and minimum values of C_{OS} among the sensors.

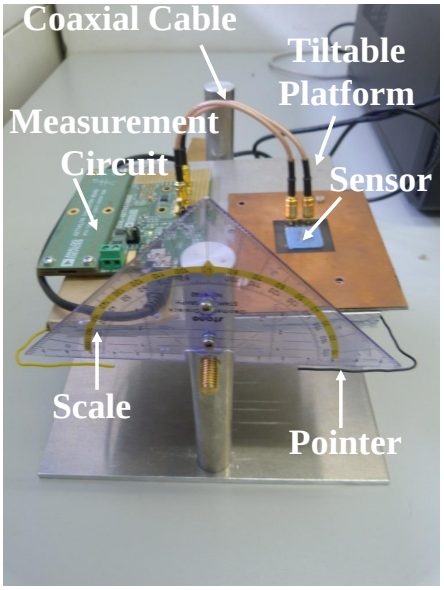

Figure 2.15: Photograph of the set-up used to evaluate the performance of the sensor for tilt

2.7 Experimental Set-up and Results

In order to validate various aspects practically, different capacitive sensors with unique and unclonable characteristic were fabricated and tested. Sensor electrode capacitances were measured with the evaluation board (AD7746) from Analog Devices [73]. The evaluation board builds around an IC AD7746 capacitance-to-digital converter which converts dual-electrode capacitance into digital voltage. The IC AD7746 has an accuracy of 4 fF, a resolution down to 4 aF and can measure changes of the capacitance up to ±4 pF. These specifications are enough to evaluate sensor prototypes. A shielded cable was used to connect sensor electrodes to the evaluation board. The shielded cable removes the effect of external interference on sensor output. Capacitances were recorded using an in-built software suite available with the evaluation board. The performances of the sensors were evaluated for tilt. A photograph of the test set-up is shown in Fig. 2.15. The sensor, along with the measurement circuit, was placed on a tilting platform. A scale was then provided to measure the tilt angle. To evaluate output characteristics, the sensors were tilted from -180^o to +180^o and the sensor electrode capacitances were recorded. Further details and test results are discussed in the following subsections. All experiments were carried out in a normal laboratory environment (22^o ± 0.5^o).

2.7.1 Interdigitated and Improved Electrode Structure

Prototype sensors with an interdigitated and improved electrode structure were fabricated. Here, the thicknesses of the distance holder (t_d) and the active element, as well as the diameter of the conductive balls, were 1.0 mm. To validate the simulation models

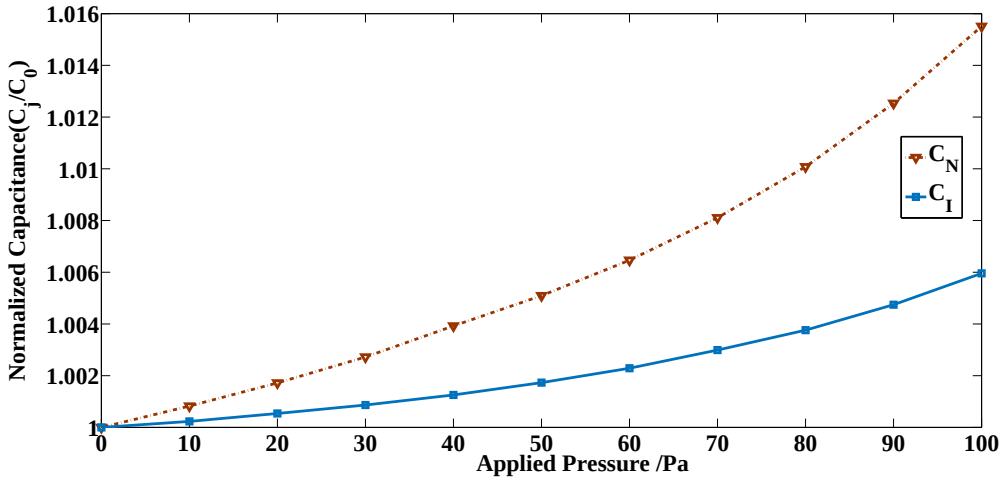

Figure 2.16: Normalized capacitance recorded from prototype sensors with IDE (C_I) and an improved electrode (C_N) for pressure load

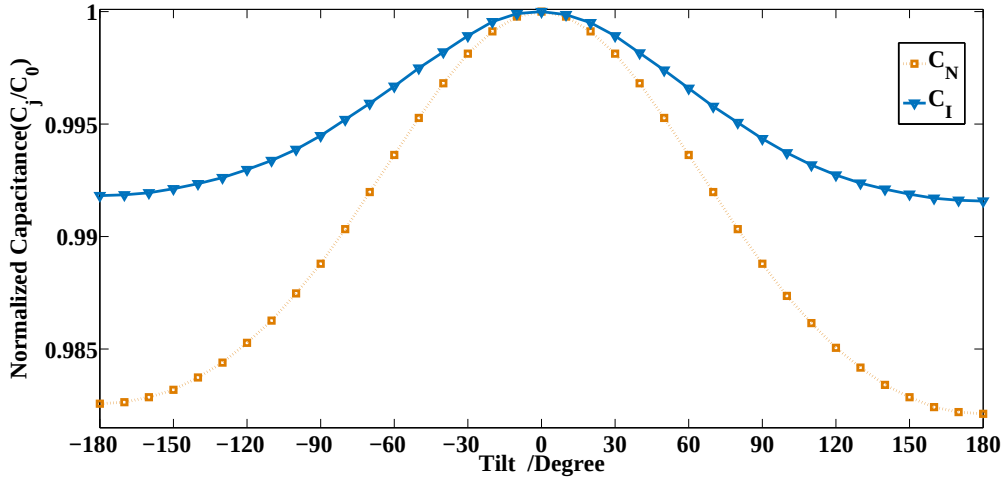

Figure 2.17: Normalized capacitance recorded from prototype sensors with IDE (C_I) and an improved electrode (C_N) for tilt

practically, a pressure load was applied to the functional element. Instead of applying pressure directly, a weight was applied to the functional element and pressure was then calculated (Pressure=Weight/Area). At 0 Pa, sensors with IDE and an improved electrode showed capacitance of 1.07 pF and 0.90 pF, respectively. The normalized capacitances recorded at different pressures from both sensors are plotted in Fig. 2.16. C_N is capacitance recorded from the sensor with the improved electrode, and C_I is sensor capacitance with IDE. The results are comparable with simulation studies. As expected, the sensor with the improved electrode showed better performance. Both sensors were also tested for tilt. The test results are presented in Fig. 2.17. The sensors showed maximum capacitance at 0^o. With tilt, in both the clockwise and anticlockwise directions, capacitance decreased and minimum capacitance was observed at $\pm 180^o$. Here also, the sensor with the improved electrode structure showed higher sensitivity.

2.7.2 Sensor Uniqueness and Reliability

In order to validate practically the effect of random conductive ball distribution on the sensor output, six sensor models (SMs), each having different ball distributions, were fabricated. t_d, t_i, and d_b were 0.5 mm in size. Ninety-three balls, 0.5 mm in diameter, were randomly distributed in each SM, SM_1 to SM_6. The numbers of conductive balls were selected such that they would fill 10% of the active functional element volume. In other words, the packing density (PD) of the conductive balls was 10%. Ball distributions in the prototype SMs are shown in Fig. 2.18. The performances of the fabricated SMs were evaluated for tilt, whereby the SMs were tilted from -180^o to +180^o and the sensor capacitances were recorded for every 10^o tilt. The recorded values are given in Fig. 2.19. Each SM showed measurably unique characteristics. The tolerances in the fabrication processes improved uniqueness in the prototype SMs, compared to simulation studies.

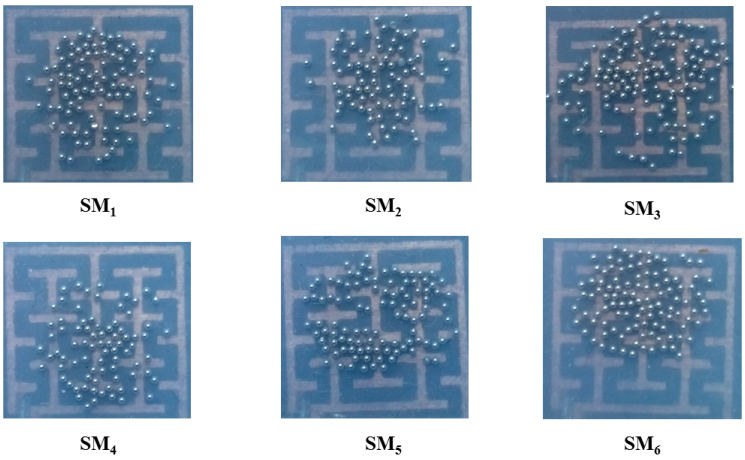

Figure 2.18: Conductive ball distribution in prototype SMs, SM_1-SM_6. Ninety-three balls are randomly distributed inside the PDMS membrane

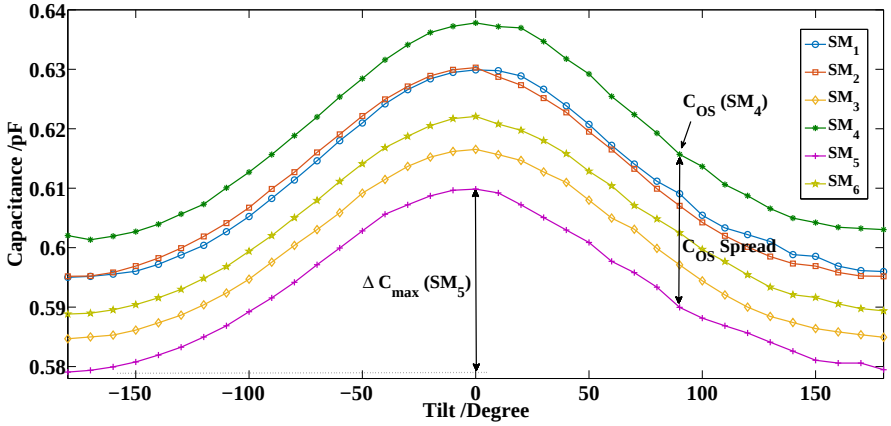

Figure 2.19: Sensor capacitance recorded from SM_1-SM_6 at different tilt angles

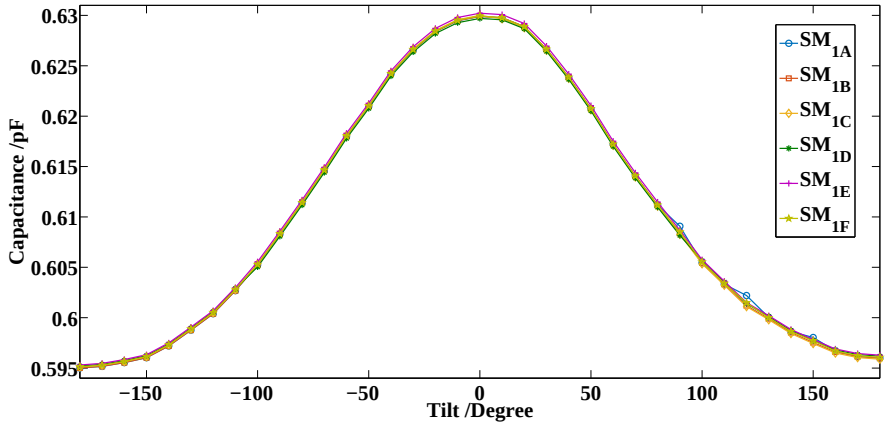

Figure 2.20: Sensor capacitance recorded from SM_1 when -180^o to +180^o tilt was repeated six times

The reliability of the SMs was also verified. Tilts on each SM were repeated six times, and in order to include the effect of environmental variations, measurements were taken 1 hour apart. The recorded capacitance values from SM_1 are shown in Fig. 2.20, and each SM showed high reliability.

The sensor parameters discussed in Section 2.6 were evaluated. SM_1 -SM_6 showed an average C_{OS} of 0.6041 pF with a C_{OS} spread of 0.0224 pF. The average ΔC_{max} was 0.03664 pF. The inter-ρ_c, calculated amongst the SM_1 -SM_6 outputs, gave a measure of uniqueness. The six SMs had 15 ($6C_2$) different combinations of ρ_c, the values for which are plotted in Fig. 2.21. Similarly, reliability was determined by calculating intra-ρ_c among SM_{1A}-SM_{1F}. All the SMs showed an intra-ρ_c of 1.000. Out of these ρ_c values, the minimum value of intra-ρ_c (worst-case reliability) and maximum value of inter-ρ_c (worst-case uniqueness) are important. While considering a large number of sensors, there is a high probability that their inter-ρ_c values will be less than the

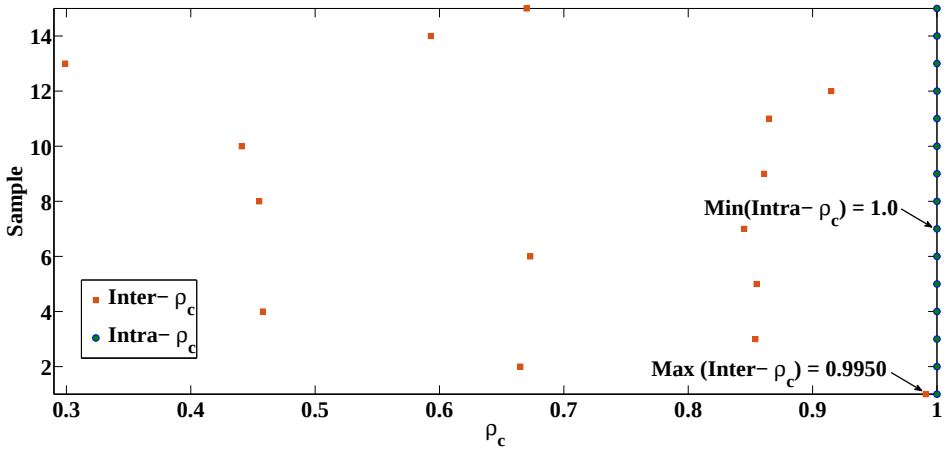

Figure 2.21: The uniqueness parameter (inter-ρ_c) and the reliability parameter (inter-ρ_c), evaluated from the capacitive sensors.

$Max(inter - \rho_c)$ of the sample SMs and their inter-ρ_c greater than the $Min(inter - \rho_c)$ sample of SMs. Therefore, in order to uniquely identify the sensor from its characteristic,

$$Min(intra - \rho_c) > Max(inter - \rho_c). \tag{2.8}$$

This implies that the worst-case reliability of the SMs should greater than the worst-case uniqueness observed among the SMs. The higher the difference, the better the uniqueness. The developed SMs showed $Min(intra - \rho_c)$ of 1.000, which is greater than $Max(inter - \rho_c)$ of 0.995.

2.7.3 Sensor Optimization

In the proposed sensor, the random distribution of conductive balls is the primary source of sensor uniqueness. Factors, namely the conductive ball's PD and its distance away from the electrode (t_d), can influence sensor uniqueness. The objective of this section is to study the effect of conductive ball PD and its distance away from the electrode structure on sensor characteristics, and then optimize these factors to acquire high degree of uniqueness and sensitivity.

2.7.4 Effect of conductive ball Packing Density (PD)

In addition to SMs with a conductive ball PD of 10%, discussed in Section 2.7.2, six SMs with a conductive ball PD of 30% (280 balls) and another six SMs with a PD of 50% (465 balls) were also fabricated. The sensors were tested for tilt. The output recorded from SMs for a 10%, 30% and 50% ball PD are in Fig. 2.22(a), Fig. 2.22(b) and Fig. 2.22(c), respectively. The sensor parameters were calculated and given in Table 2.2. Comparing SMs with a different ball PD, the following observations can be made.

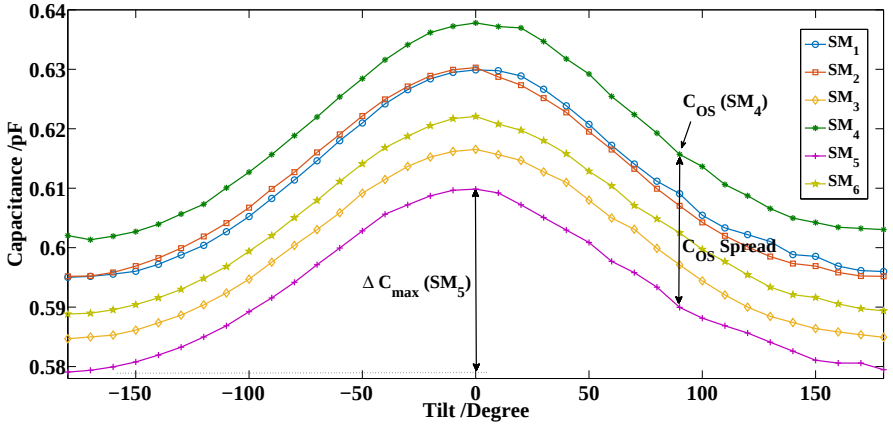

(a)

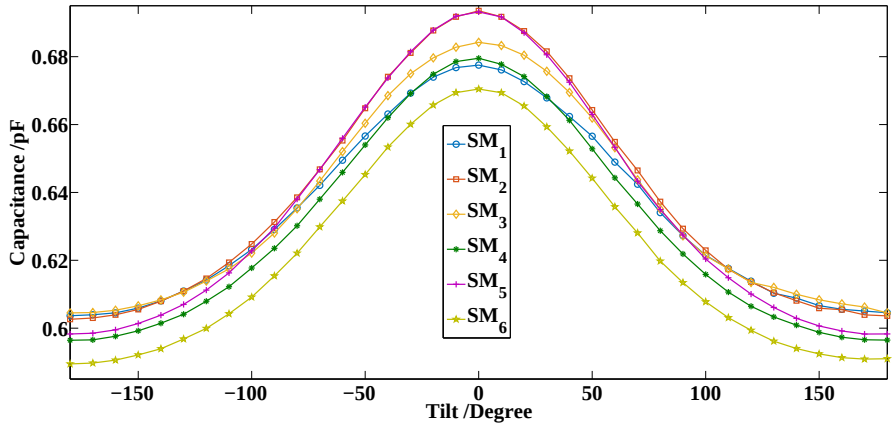

(b)

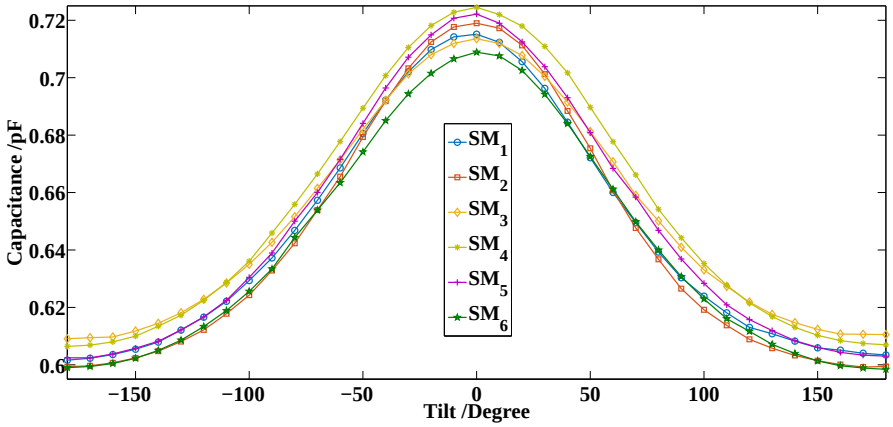

(c)

Figure 2.22: Output recorded from sensors SM_1-SM_6 for tilt (a) PD = 10%. (b) PD = 30%. (c) PD = 50%

- C_{OS} increases in line with an increase of the PD: With the increase of the number of balls, the floating electrode area increases while the dielectric membrane area decreases. This increases C_{TF} and C_{FR} (in Fig. 2.4) and accordingly increases C_A. Since $C_{OS} = C_{TR} + C_A$, C_{OS} increases.

- ΔC_{max} (which is proportional to sensitivity) of the sensor increases in line with the increase of ball PD: The increase of the number of balls increases the mass of the functional element. As functional element deflection is proportional to its mass, sensitivity therefore increases.

- C_{OS} spread decreases with the increase of ball PD: At low PD, balls are separated and individual balls are more 'visible' to the electrical field. Depending on their positions, these balls modify the electrical field pattern, which results in large variations in C_{OS} (C_{OS} spread) among the SMs. With this increase of the ball PD, the effect of spatial arrangement decreases. As the balls move closer, the 'visibility' of individual conductive balls and the way they uniquely modify the electrical field lines start to decrease, which in turn reduces C_{OS} spread.

- Variations of ΔC_{max} among the SMs are less significant at low PD: At low PD, as the number of balls are fewer, their contribution to the the mass of the functional element is negligible. Hence, the way in which ball distribution modifies functional deflection characteristics is limited, which then leads to similar sensitivities for all SMs. However, with the increase of ball PD, the mass contribution of the balls increases. In this case, ball distribution can modify the deflection characteristics of the functional element, which leads to variations in ΔC_{max} among SMs.

2.7.5 Effect of distance holder thickness (t_d)

Distance holder thickness (t_d) determines the distance between an electrode's structure and conductive balls. The effect of variations of t_d on sensor characteristics was verified. Six SMs with $t_d = 200$ μm and another six SMs with $t_d = 100$ μm were fabricated. The conductive ball PD was 30% in all cases. Capacitances recorded from the SMs for tilt are given in Fig. 2.23, whilst the sensor parameters are highlighted in Table 2.2. The following conclusions can be drawn by comparing the results.

- C_{OS} increases with a decrease of t_d: Along with the decrease of t_d, the conductive balls move closer to the electrode. In Fig. 2.4, the decrease of the distance between the balls and the electrode structure increases C_{TF} and C_{FR}, which in turn increases C_A. As $C_{OS} = C_{TR} + C_A$, C_{OS} increases.

- ΔC_{max} increases with a decrease of t_d: Electrical field strength is higher near the electrode structure. The decrease of t_d moves the functional element into the stronger electrical field region. Here, small functional element deflection can produce large changes of the electrode capacitance.

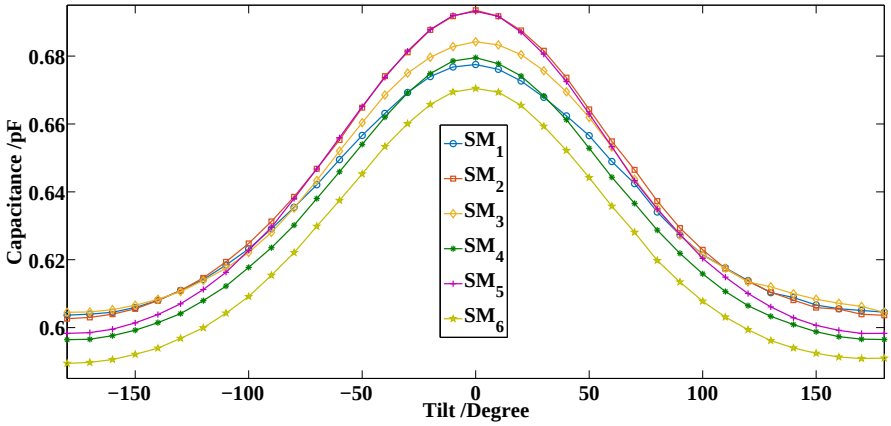

(a)

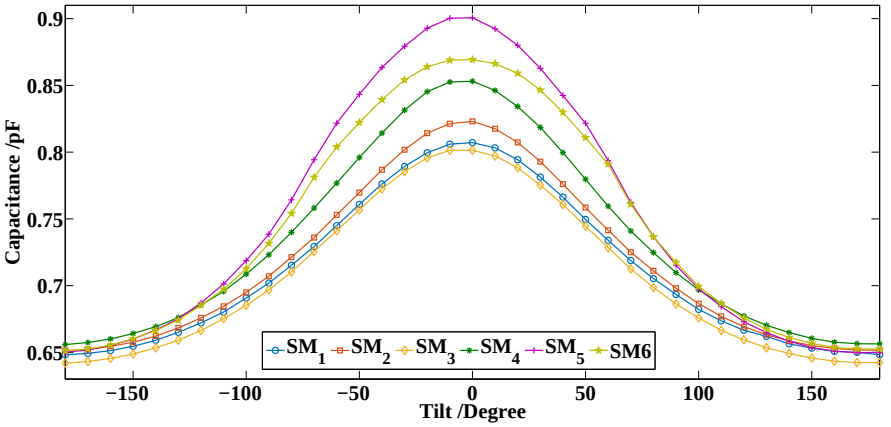

(b)

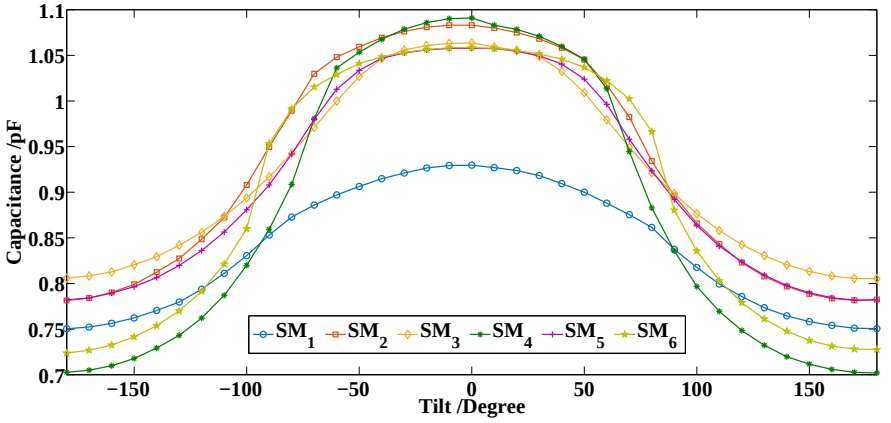

(c)

Figure 2.23: Output recorded from SMs (SM_1-SM_6) with a 30% ball PD for tilt. (a)t_d = 500 μm. (b)t_d = 200 μm. (c)t_d = 100 μm.

Table 2.2: Sensor Parameters

t_d (in μm) \ PD (in %)	Parameters	**10 (# 93)**	**30 (# 280)**	**50 (# 465)**
500	C_{OS}	0.6041	0.6332	0.6385
	ΔC_{max}	0,0336	0.0839	0.1143
	C_{OS} Spread	0.0224	0.0164	0.0130
	$Max(Inter - \rho_c)$	0.9950	0.9950	0.9960
	$Max(Intra - \rho_c)$	1.0000	1.0000	1.0000
200	C_{OS}	0.6701	0.7164	0.7854
	ΔC_{max}	0.0568	0,1927	0.3029
	C_{OS} spread	0.0537	0.0417	0.0284
	$Max(Inter - \rho_c)$	0.9900	0.9940	0.9980
	$Max(Intra - \rho_c)$	1.0000	1.0000	1.0000
100	C_{OS}	0.7939	0.9065	1.0052
	ΔC_{max}	0.1018	0.2895	0.3393
	C_{OS} Spread	0.0967	0.0999	0.0837
	$Max(Inter - \rho_c)$	0.9920	0.9850	0.9930
	$Max(Intra - \rho_c)$	1.0000	1.0000	1.0000

- C_{OS} spread among the SMs increases in line with a decrease of t_d: The spatial arrangement of balls has a greater effect in stronger electrical field regions.
- Unlike Fig. 2.23(a) and Fig. 2.23(b), a saturation tendency or a nearly flat response can be observed in Fig. 2.23(c): As explained in Section 2.3, when the membrane moves closer to the electrode, thereafter a particular point capacitance C_{FG} (in Fig. 2.4) becomes more dominant than C_{TF} and C_{FR}, which decreases sensor capacitance. When the functional element moves into this C_{FG} dominant region, sensor sensitivity decreases and shows a saturation tendency. From Fig. 2.23(c), when $t_d = 100$ μm, the functional element partially operates in C_{FG} dominant regions. The tilt at which the functional enters the C_{FG} dominant region is different for each SM, depending on random factors such as ball distribution and fabrication tolerances, and further improves uniqueness.

To validate further the effects of t_d and ball PD, sensors with ball PDs equal to 10% and 50%, and $t_d = 200$ μm and 100 μm, were fabricated and tested. The sensor parameters calculated from all the sensor models are given in Table 2.2. Similar variations in the sensor parameters were observed with t_d and ball PD variations. Among all the sensor models tested, sensors with a ball PD of 30% and $t_d = 100$ μm showed the highest differences between $Max(inter - \rho_c)$ and $Min(intra - \rho_c)$, i.e. a maximum uniqueness. With a ball PD of 30%, the effect of both spatial ball arrangement and mass distribution is present. This effect increases when reducing t_d. At $t_d = 100$ μm, the functional element moves between the C_{OS} and C_{FR} dominant regions. Further decreases in t_d

keep the functional element within the less sensitive C_{FG} dominant region. Operating the functional element in the C_{FG} dominant region might improve uniqueness, but it will also affect the sensitivity of the sensor. Hence, for the proposed sensor, $t_d = 100$ μm and ball PD= 30% can provide maximum uniqueness, without compromising sensitivity.

2.8 Unclonability of the Capacitive Sensor

The proposed capacitive sensor showed unique output characteristic. If this output characteristic is unclonable, then the proposed sensor can be used as a hardware identifier and a sensor with an integrated identifier. A device is said to be unclonable if it has the following properties.

- It is difficult to duplicate a device's characteristic, even if the exact device parameters are known.
- It is impossible to model or predict device characteristic.

In the proposed capacitive sensor, the major factor contributing to sensor uniqueness is a random conductive ball distribution. It is difficult to replicate the same ball arrangements. Again, the sensors are developed using less-tolerance fabrication processes. The fabricated membranes (distance holder and active element) showed a variation of ± 20 μm. The stiffness of the active element (of the functional element) was also different for different sensors. These random variations in the PDMS structure improves the uniqueness. Furthermore, the functional element operates near the uncertain C_{FG} dominant region. The tilt at which the functional element moves into the C_{FG} dominant region depends on variations in the functional element. All of these uncertainties introduced, due to random variations, make sensor characteristic nearly impossible to duplicate, even for a manufacturer.

It is also impossible to develop a sensor model, since the random conductive ball arrangement modifies the electrical field pattern and the functional element deflection in a unique way. The source of uniqueness is both electrical and mechanical, whilst the coupling of electrical and mechanical uniqueness makes sensor modeling difficult. Furthermore, the operation of the sensor in the C_{FG} dominant region introduces more uncertain variables, which in turn makes the sensor modeling more complex.

Considering all of these factors, there are enough reasons to assume that the proposed sensor is unclonable. The unique and unclonable output characteristic of the sensor can be used as sensor's signature.

2.9 Limitations of the Proposed Sensor Design

1. Large surface area: The active surface area of the sensor (13 mm $\times$ 13 mm) is comparatively large. In this sensor design, if the surface area is reduced, in order to maintain PD, the numbers of conductive balls also need to be reduced, which will affect the sensitivity.

2. Limited sensitivity: The maximum sensitivity that can be achieved by reducing the distance between the electrode structure and the functional element is limited. After a particular point, the functional elements enter the C_{FG} dominant region and then sensitivity starts to decrease.

3. Large offset capacitance: The sensor has large, fixed offset capacitance along with variable capacitance. Offset capacitance reduces the sensitivity of the entire sensing system. Details are discussed in the next chapter.

4. External interference: The region above the functional element is not shielded. Any interference above the functional element can affect the sensor output.

2.10 Conclusion

The design, modeling, simulation, optimization, fabrication and testing of a capacitive sensor with unique and unclonable characteristic was presented in this chapter. The sensor consists of a PDMS structure filled with randomly distributed conductive balls as the functional element. The functional element deflects under the influence of tilting. A capacitive electrode structure converts membrane deflection into a change of capacitance. The random distribution of conductive balls modifies the deflection characteristics of the functional element and electrical field pattern from the electrode structure of each sensor in a unique way, which results in unique output capacitance for each sensor. The effects of the number of conductive balls (packing density) and their distance away from the electrode structure (distance holder thickness) are verified. These parameters are optimized to acquire maximum uniqueness and sensitivity. The detailed analysis of the sensor design shows that the region above the electrode structure can be divided into C_{FG} dominant and C_{FR} dominant regions. The proposed sensor shows maximum uniqueness, unclonability and sensitivity when operated near the interface of the C_{FG} and C_{FR} dominant regions.

3 Differential Capacitive Sensor with Unique and Unclonable Characteristic

3.1 Introduction

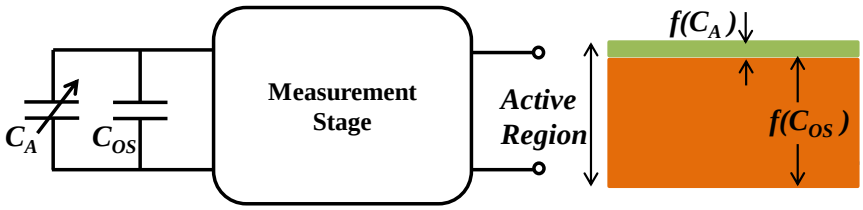

Figure 3.1: Capacitive sensing system

The capacitive sensor discussed in Chapter 2 has fixed offset capacitance (C_{OS}) in parallel with variable capacitance (ΔC_A) that varies with the measurand, in this case tilt. C_{OS} is ten times larger than ΔC_A. In capacitive sensors, large C_{OS} can degrade the performance of the sensing system.

Consider the capacitive sensing system shown in Fig. 3.1. A capacitive sensor, with a large C_{OS} and a small ΔC_A, is connected to a measurement stage. The active operating region of circuits in the measurement stage are fixed. For instance, in an operational amplifier-based capacitance measurement circuit, the active linear region of the operation amplifier is limited to the source voltage. The large C_{OS} takes up the majority of this active region and limits the amplification that can be applied to the ΔC_A. This affects the sensitivity and dynamic characteristics of the sensing systems. Hence, in capacitive sensors, it is desirable to have minimum offset capacitance.

This chapter proposes a differential capacitive sensor which will nullify offset capacitance and has high uniqueness, unclonability and sensitivity compared to the dual-electrode sensor discussed in Chapter 2. Details are discussed in the following sections.

3.2 Sensor Design

The differential capacitive sensor is shown in Fig. 3.2. The differential sensor is an extended dual-electrode sensor with an additional upper electrode structure. The terminals T_L (transmitter), R_L (receiver) and G_L (ground) form the lower electrode structure, and the T_U, R_U, and G_U terminals form the upper one. Capacitances between T_L and

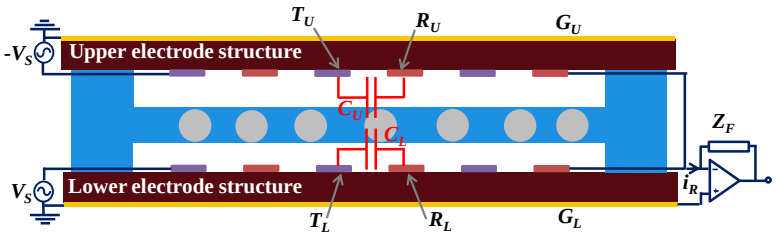

Figure 3.2: Unique and unclonable sensor with a differential capacitive electrode arrangement

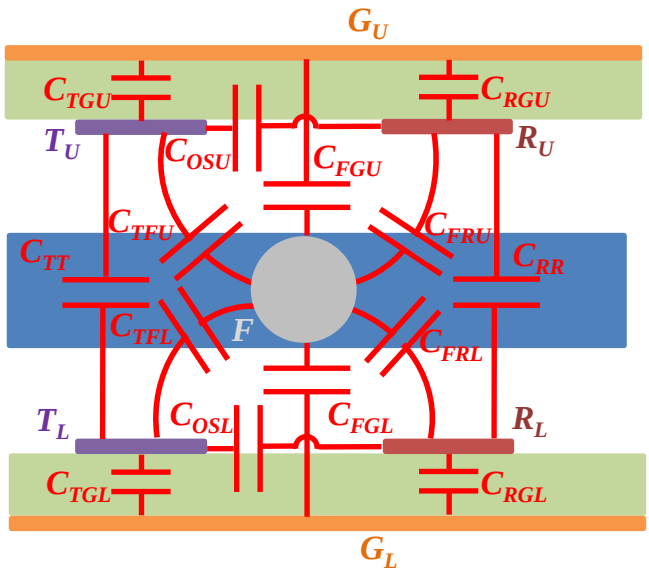

Figure 3.3: Diagram showing various capacitance components that contibutes to the sensor capacitance

R_L, and between T_U and R_U, are represented by C_L and C_U, respectively. Various capacitance components that form C_L and C_U are shown in Fig. 3.3.

Initially, consider the lower and upper electrode capacitances separately. The lower electrode capacitance C_L is a combination of the different capacitances shown in Fig. 3.4. Here, F, T_U, and R_U are floating electrodes, and they are at floating potentials. Hence, C_{TFU}, C_{FRU} and C_{OSU} (in Fig. 3.3) are neglected. Similarly, C_{TTGU} and C_{RRGU} in Fig. 3.4 represent series combinations of C_{TT} and C_{TGU}, and C_{RR} and C_{RGU} (in Fig. 3.3), respectively. As both G_U and G_L have the same ground potential, C_{TTGU}, C_{FGU} and C_{RRGU} become parallel with C_{TGL}, C_{FGL}, and C_{RGL}, respectively. Under these conditions, electrical equivalent model of the lower electrode capacitance (C_L) can be represented as in Fig. 3.4(b). C_L is similar to dual-electrode capacitance discussed in Chapter 2 (Fig. 2.4); however, the presence of the upper electrode structure increases the values of C_{TGL}, C_{FGL}, and C_{RGL}. In this case, as in Equation (2.4), C_L can be

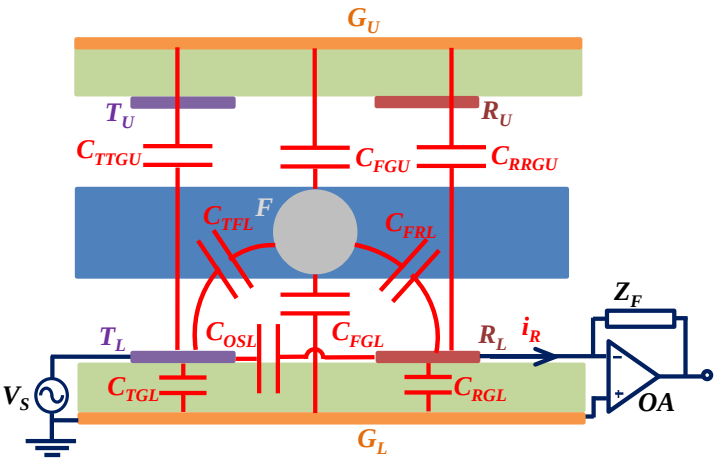

(a)

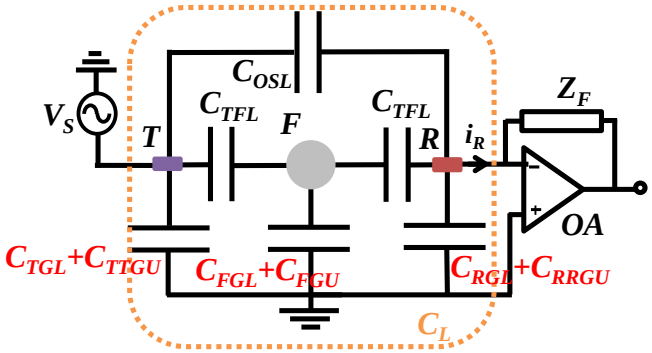

(b)

Figure 3.4: (a) Various capacitance components that form the lower electrode capacitance of a differential capacitive sensor. (b) Electrical equivalent model of the lower electrode structure

expressed as:

$$C_L = C_{OSL} + C_{AL}, \tag{3.1}$$

where C_{OSL} is the fixed offset capacitance and C_{AL} is the variable capacitance of the lower electrode structure. Here, C_{AL} is:

$$C_{AL} = \frac{C_{TFL}C_{FRL}}{C_{TFL} + C_{FRL} + (C_{FGL} + C_{FGU})} \tag{3.2}$$

The additional capacitances in the differential electrode structure, C_{TTGU} and C_{RRGU}, do not affect C_L. However, from Equation (3.2), the addition of C_{FGU} slightly reduces C_{AL}, which in turn reduces sensitivity of the sensor.

Similarly, upper electrode capacitance C_U can represented as:

$$C_U = C_{OSU} + C_{AU}, \tag{3.3}$$

where C_{OSU} and C_{AU} are the offset and variable capacitances of the upper electrode structure.

Functional element deflection changes C_L and C_U. When the membrane moves towards the lower electrode structure, C_L increases and C_U decreases, and vice versa. Under this condition, C_L and C_U can be expressed as:

$$C_L = C_{OSL} + C_{AL} \pm \Delta C_{AL}, \tag{3.4}$$

$$C_U = C_{OSU} + C_{AU} \mp \Delta C_{AU}, \tag{3.5}$$

where ΔC_{AL} and ΔC_{AU} are variations in lower and upper electrode capacitance, due to membrane deflection.

The differential capacitance measurement technique discussed in section 2.2.2 is employed to measure the sensor capacitance. T_L is excited with voltage signals V_S and T_U with -V_S. R_L and R_U are connected together. An I to V converter converts the receiver current i_R into a voltage signal. Here, i_R is proportional to $C_L - C_U$, in which case sensor capacitance C_S $(= C_L - C_U)$ will be:

$$C_S = (C_L - C_U) = (C_{OSL} - C_{OSU}) + (C_{AL} - C_{AU}) \pm (\Delta C_{AL} + \Delta C_{AU}). \tag{3.6}$$

If the dimensions of the upper and the lower structures are equal, then:

$$C_{OSL} = C_{OSU}, \tag{3.7}$$

and if their distances to the functional element are equal, then:

$$C_{AL} = C_{AU}. \tag{3.8}$$

Under these conditions, C_S can be expressed as:

$$C_S = \pm(\Delta C_{AL} + \Delta C_{AU}). \tag{3.9}$$

From Equation (3.9), the sensor with the differential electrode arrangement cancels out the unwanted offset capacitances that are common to both electrode structures. C_S only contains the variable capacitance. Here, C_S is the sum of upper and lower electrode variable capacitance. Hence, the differential electrode sensor is expected to provide higher sensitivity than the dual-electrode sensor. As C_S is independent of C_{OS}, a thick dielectric layer can be used for both the upper and the lower electrodes, which reduces the effect of C_{FG} $(C_{FGU} + C_{FGL})$ and improves their sensitivity, as discussed in section 2.3. This further improves the sensitivity of the differential sensor.

3.3 Simulation Studies

Unique and unclonable sensors with a differential capacitive electrode arrangement were simulated using the FEA software COMSOL Multiphysics. Six differential capacitive sensor models (SMs), each having a different conductive ball distribution, were simulated. Sensor dimensions, ball distributions, electrode structures, selected materials and boundary conditions were the same as for the dual-electrode SMs discussed in Chapter 2. The dimensions of the upper and lower electrode structures and their distances to the functional element were kept equal. The SMs ($SM_1 - SM_6$) were meshed and simulated for tilt. The functional element deflection in the SMs was similar to that of the dual-electrode SMs (shown in Fig. 2.12). Initially, C_L and C_U of SM_1 were simulated, separately exciting the lower (T_L = 1 V; R_L = 0 V; G_L & G_U = ground; T_U & R_U = floating) and upper (T_U = 1 V; R_U = 0 V; G_L & G_U = ground; T_L & R_L = floating) electrode structures. Under this condition, the electrical model discussed in Fig. 3.4 is valid and the sensor capacitance is similar to dual-electrode sensor capacitance. C_L and C_U simulated from SM_1 for different tilts are plotted in Fig. 3.5. At 0^o, the functional element deflects in such a way that it is as close as possible to the lower electrode structure and as far away as possible from the upper electrode structure. C_L is the maximum and C_U the minimum at 0^o. With the tilt in a clockwise or an anticlockwise direction, the functional element moves away from the lower electrode and closer to the upper electrode. C_L decreases while C_U increases. At $\pm 90^o$, as the membrane is in the null position, $C_L \approx C_U$. With further tilting, the membrane moves further away from the lower electrode and closer to the upper electrode. C_L increases and C_U decreases, reaching the minimum and maximum values, respectively, at 180^o. The sensor capacitances and sensitivities of the upper and lower electrode structures in the differential electrode sensor are slightly lower than for the dual-electrode sensor (shown in Fig. 2.13), because

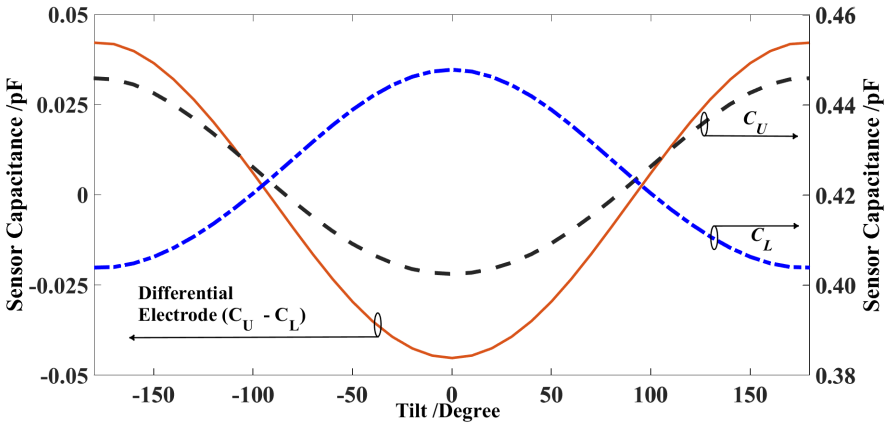

Figure 3.5: Upper electrode capacitance (C_U), lower electrode capacitance (C_L) and differential electrode capacitance (C_U - C_U) recorded from SM_1 at different tilt angles

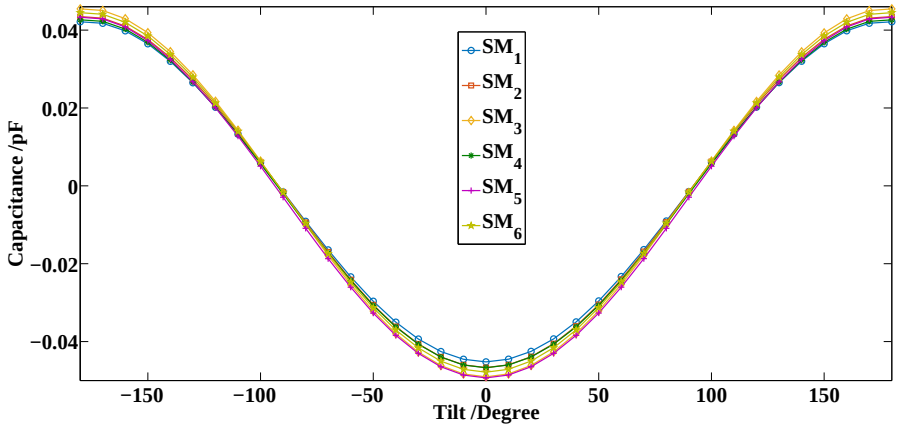

Figure 3.6: Capacitance recorded from differential electrode SMs for different tilts

of high $C_{FG}(= C_{FGL} + C_{FGL})$.

In order to simulate differential electrode arrangement, both lower and upper electrodes were simultaneously excited. Terminal T_L was set to +1 V, while the terminal T_U was at -1 V. Both R_L and R_U were at 0 V. The capacitance values for different tilt angles are shown in Fig. 3.5. The differential electrode arrangement cancels out the fixed offset capacitances of the upper and lower electrodes and adds the variable capacitances. Sensor output only contains variable capacitances that vary according to the measurand. Furthermore, the addition of the variable 'capacitance' results in a better sensitivity (ΔC_{max}). Comparing the simulation results, the differential electrode SM_1 offers a 1.5 times higher sensitivity than the dual-electrode SM_1. In the differential electrode sensor, one should note that the sign of the capacitance value only represents the direction of the current flow. The simulated output capacitances from all the SMs ($SM_1 - SM_6$), with different conductive ball arrangements, are shown in Fig. 3.6. Output of each SM is different from others.

3.4 Experimental Set-up and Results

In order to validate the differential electrode sensor design, prototype SMs were developed. An active element, two distance holders and two sensor substrates, stacked together, as shown in Fig. 3.7, formed the sensor structure. These components were fabricated using the process discussed in Section 2.5. From Chapter 2 (Section 2.7.3), the dual-electrode sensor showed optimum uniqueness and sensitivity for a conductive ball PD of 30% and a distance holder thickness of 100 μm. The same specifications were also selected for the differential electrode sensors. Six differential electrode SMs with different ball distributions were fabricated. Sensor capacitances were measured using an AD7746 evaluation board from Analog Devices [73]. The evaluation board has two channels for capacitance measurement, and its channels are configured for dual or differential electrode measurement. The SMs were tested for tilt, and the measurement

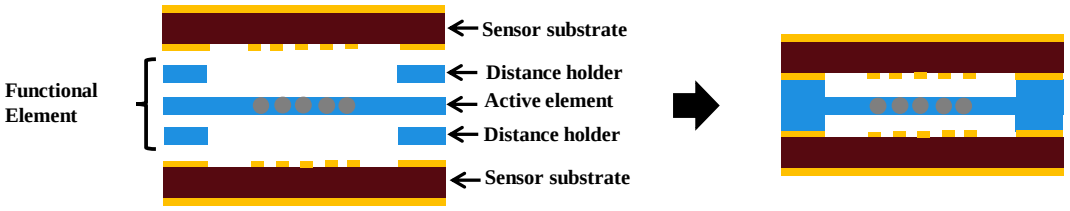

Figure 3.7: Fabrication of differential capacitive sensors with unique and unclonable characteristic. The active element, distance holders and sensor substrates were fabricated using the process discussed in Section 2.5

set-ups and the procedures were similar to the dual-electrode sensor testing discussed in Section 2.7.

Differential electrode SMs were tilted from $+180^o$ to -180^o. Initially, the upper electrode capacitance (C_U) and the lower electrode capacitance (C_L) of SM_1 were measured. The evaluation board was set for dual-electrode capacitance measurement. C_U and C_L, recorded for different tilts, are shown in Fig. 3.8. As expected, both C_U and C_L vary in a push-pull manner, in that when C_U increases, C_L decreases, and vice versa. Next, the evaluation board was set for differential measurement. The differential capacitance recorded from SM_1 is also plotted in Fig. 3.8. The differential electrode configuration cancels out unwanted offset capacitance and adds the variable component of both the upper and the lower electrodes. The output of the differential sensor only contains variable capacitance. All the differential electrode SMs, $SM_1 - SM_6$, were tested for tilt, and their outputs are shown in the Fig. 3.9. Sensor parameters (discussed in Section

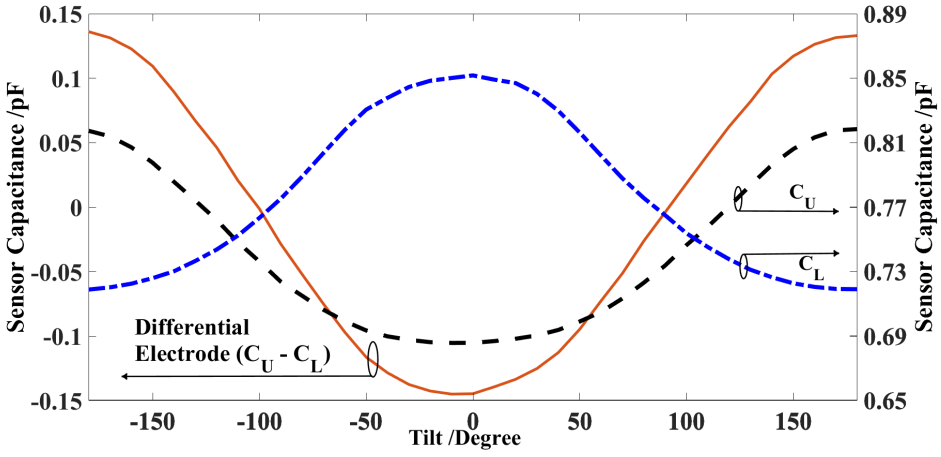

Figure 3.8: Upper electrode capacitance (C_U), lower electrode capacitance (C_L), and differential electrode capacitance (C_U - C_L) recorded from the prototype differential capacitive sensor (SM_1) at different tilt angles

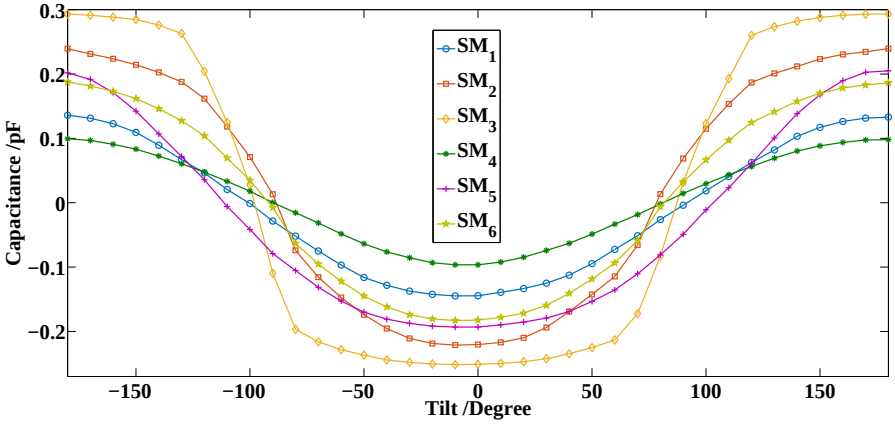

Figure 3.9: Capacitance recorded from prototype SMs, $SM_1 - SM_6$

Table 3.1: Sensor Parameters

Parameters	**dual-electrode Sensor**	**Differential Electrode Sensor**
C_{OS} (pF)	0.9065	0.0157
ΔC_{max} (pF)	0.2895	0.3752
C_{OS} Spread (pF)	0.0999	0.1177
$Max(Inter - \rho_c)$	0.9850	0.9367
$Max(Intra - \rho_c)$	1.0000	1.0000

2.6) were evaluated and the values are given in Table 3.1. The dual-electrode sensor parameters are also given. Comparing both values, the following conclusions can be drawn.

- Differential electrode arrangement reduces the offset capacitance of the sensor: In differential electrode SMs the average value of C_{OS} is 93 times lower than for the dual-electrode sensor. The C_{OS} is sensor capacitance in the null position, which in this case is the fixed offset capacitance.

- Differential electrode SMs show a high sensitivity: The average ΔC_{max} of the differential electrode SMs, which is proportional to sensor sensitivity, is 1.4 times higher than for the dual-electrode SMs.

- Differential electrode showed higher uniqueness and reliability: The $Max(Inter - \rho_c)$, recorded for the differential electrode sensor, is lower than for the dual-electrode sensor. Both sensor configurations showed a high reliability.

3.5 Advantages of a Differential Capacitive Sensor

Compared to the dual-electrode capacitive sensor discussed in Chapter 2, the differential capacitive sensor has the following advantages.

1. Very low offset: Differential electrode SMs have low offset capacitance.
2. High performance: Differential electrode SMs exhibit high sensitivity and uniqueness.
3. Zero external interference: The sensor structure sits between the upper and lower ground planes, acts as a Faraday shield, and nullifies the effect of external interference on the sensor's output.
4. Difficult to duplicate: As a result of the upper and lower ground planes, it impossible to probe the sensor's dimensions, ball numbers, distribution, etc. without destroying the sensor structure. Also, the addition of the electrode structure (compared to a dual-electrode sensor) adds more uncertain variables, which makes the sensor model more complex.
5. Cancels out the common mode error: The differential measurement technique cancels out errors due to variations in temperatures, humidity, etc. which affect both upper and lower electrode capacitance.

3.6 Conclusion

The design and development of a differential capacitive sensor with unique and unclonable characteristic has been presented. The sensor consists of a unique and unclonable functional element (a PDMS structure filled with conductive balls) sandwiched between upper and lower electrode structures. Membrane deflection changes the capacitance of the upper and lower electrode structures in a push-pull manner. A differential capacitance measurement technique is employed to measure sensor capacitances. The differential measurement canceled out offset capacitance common to both the upper and lower electrode structures and added the variable 'capacitance', which varies according to the measurand. The differential capacitive sensor offered higher sensitivity, uniqueness and unclonability, as well as lower offset capacitance compared to the dual-electrode counterpart discussed in Chapter 2.

4 Fabrication and Electromechanical Characterization of Conductive PDMS Membranes

4.1 Introduction

Poly-Di-Methyl-Siloxane (PDMS) is a silicon-based flexible elastomer which has a wide range of applications. Its unique properties, such as flexibility, biocompatibility, optical transparency, water resistance and low fabrication cost, make PDMS a suitable material for sensors, actuators, microfluidic devices, etc. [74]. However, the very high electrical resistance (in a range of 10^{15} kΩ) and the low dielectric constant ($\epsilon_r = 2.75$) of PDMS limit its use to a passive material or a structural element in most of these applications [75] [76], including the dual and differential capacitive sensors discussed in Chapter 2 and Chapter 3. In these capacitive sensors, PDMS filled with conductive balls is the functional element. Here, only the conductive balls actively participate in sensing, covering 30% of the functional element volume. PDMS constitutes the remaining 70%, which has only negligible effects on the sensing process. The whole of the functional element can actively contribute to the sensing process by making PDMS conductive. A flexible material such as PDMS with conductivity can be also used as the active element in many other applications, such as strain sensors [77], micropumps and valves [78], artificial muscles [79], electronic skin [80], etc.

The electrical conductivity of PDMS can be achieved by adding conductive fillers. The most commonly used conductive fillers for the fabrication of CPDMS are carbon black (CB) particles, silver (Ag) particles and multi-walled carbon nanotubes (MWCNTs) [81] [82]. The electromechanical properties of PDMS vary according to the type of filler and its concentration. Among the fillers, Ag particles offer maximum conductivity [83], and levels of up to 100 S/cm can be achieved by adding 90-wt% of Ag into the PDMS matrix. However, Ag particles are expensive and difficult to disperse, due to the large difference in densities between them and PDMS. MWCNTs can achieve a high electrical conductivity with a low loading percentage (about 2-wt%) [84], but it is not easy to disperse MWCNTs in PDMS, due to the high aspect ratio [1]. Furthermore MWCNTs are very expensive. Compared to Ag and MWCNTs, carbon black (CB) filler is a low-cost choice for conductive PDMS and it has been shown that conductivity of about 25 S/m can be achieved with 25-wt% of CB [85]. Furthermore, CB particles are easy to mix with PDMS, owing to their desirable wetting characteristics. In addition, the Young's modulus of CB-filled conductive PDMS is lower than that of MWCNT-filled

[1] The aspect ratio of a structure is the ratio of its height to width.

CPDMS [86]. These advantages make CB-filled conductive PDMS a suitable choice for many applications.

Different micromechatronic devices consisting of CB-filled CPDMS active elements have been reported. The flexible strain sensor, discussed in [90], consists of CPDMS as sensor electrode. In [91], CB-filled CPDMS is used as electrode material for a microfluidic device. The piezo-resistive properties of CB-filled PDMS are utilized for the development of strain [92] and pressure sensors [87]. A flexible heating element is made of CPDMS in [93]. CPDMS membranes are also used as electrodes for underwater ECG (Electrocardiography) measurements [94].

The electrical properties of CB-filled CPDMS are well-studied. Several reports discussing the CPDMS resistance variations with respect to CB concentration are available in the literature. A summary of previously reported works is given in Table 4.1. Among these reports, only a few have examined variations in mechanical properties (with variations of the CB concentration) along with electrical properties. These CPDMS showed a high Young's modulus. In addition, bulk CPDMS structures (structural thickness > 200 μm) are characterized in these studies. The behavior of bulk CPDMS is different from thin membranes [95], so these results are not useful for applications such as unique and unclonable sensors, which require a soft and thin CPDMS membrane.

This chapter discusses the fabrication and electromechanical (Young's modulus and resistivity) characterizations of soft-thin-CB filled conductive PDMS membranes. The details are given in following sections.

Table 4.1: Summary of literature data for CB-filled CPDMS

Reference	**PDMS:CB**	**PT (wt%)**	**Conductivity (S/m)**	**YM (MPa)**	**ST (μm)**
[85]	Sylgard 184: Vulcan XC72R	10	25 (at 26-wt%)	-	1000
[82]	Ecoflex 00-30: ENASCO 250P	5.5	9.1 (at 11-wt%)	-	200
[87]	Sylgard 184: Vulcan XC72	6.5	<5 (at 25-wt%)	2.5 (at 6.5-wt%)	7500
[88]	Sylgard 184: Vulcan XC72	8	0.01 (at 8-wt%)	7.0 (at 8-wt%)	10000
[89]	RTV 615: Vulcan XC72	10	.005 (at 10-wt%)	-	40
This work	Alpa-Sil Classic: Vulcan XC72	5	25 (at 23-wt%)	0.17 (at 5-wt%)	100

Abbreviations—PT: Percolation threshold; YM: Young's modulus; ST: Structural thickness.

4.2 Basics of Conductive PDMS

The incorporation of conductive fillers into a matrix (PDMS) modifies the electrical behavior of the matrix. Variations in the resistive characteristic of the matrix with filler concentration are presented in Fig. 4.1. At low filler concentrations, the filler particles are distributed inside the matrix, as shown in the Fig. 4.1, so the filler-matrix acts as an insulator. With an increase of the filler concentration, the number of filler particles inside the matrix increases and filler networks start to appear across the matrix. These networks form a continuous path for the movement of electrons across the matrix, which can be formed either through mechanical contact between particles or electron tunneling effects. The filler concentration required to create these paths can be determined with the help of the percolation theory. The main idea of this theory is the existence of a percolation threshold, defined as the minimum filler concentration at which infinite networks appear in the finite lattice [96]. In the case of conductive PDMS, different definitions of the percolation threshold exist. In [81], for instance, it is the minimum concentration of conductive fillers required to establish a continuous path for the movement of electrons across the matrix. In [82], the percolation threshold is defined as critical filler concentration, where resistivity shows a significant decrease from an insulating to a conducting material. These definitions are non-quantifiable. In this paper, the percolation threshold is considered as the minimum filler concentration at which the resistivity value moves below 10^6 Ωm [97]. A further increase of filler concentration above the percolation threshold (as seen in Fig. 4.1) sharply reduces resistivity for a narrow region and then saturates at a minimum value.

Similarly, fillers inside the matrix modify the mechanical properties of the matrix. The addition of fillers to a matrix such as PDMS modify its mesh characteristics, which changes mechanical properties of the matrix such as viscosity, surface profile, Young's modulus, etc. Variations of the electrical and mechanical characteristics of a PDMS matrix with carbon black filler concentrations are discussed in the following sections.

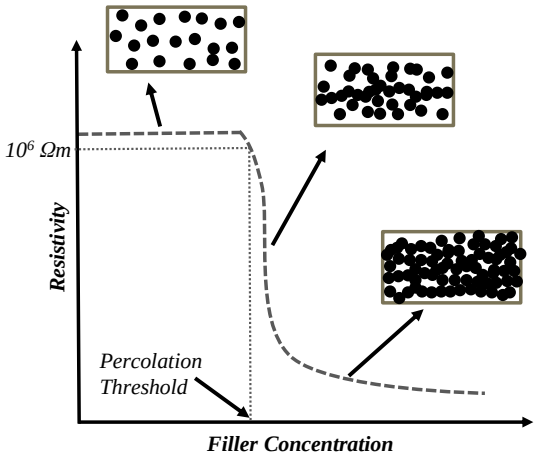

Figure 4.1: Membrane resistivity variations with conductive filler concentrations

4.3 CPDMS Composite Preparation

The CPDMS composite required for the fabrication of membranes was prepared by mixing CB fillers in a PDMS matrix. A soft PDMS Alpa-Sil Classic from Alpina was used for the preparation of CPDMS. Alpa-Sil Classic has a Young's modulus of 160 kPa, which is much lower than the most commonly used Sylgard 184 (about 2 MPa). Carbon black, Vulcan XC72 from Cabot [98], was used as filler. It has a particle size of about 50 nm.

Three different methods were used for the preparation of CPDMS composites.

4.3.1 CB-PDMS Composite Preparation

In this method, CB particles and PDMS were mixed directly. Because of the easy wetting characteristics of CB particles and the low viscosity of PDMS, it is possible to achieve conductivity by direct mixing of CB and PDMS. CB-PDMS composite preparation steps are discussed below.

1. A required amount of PDMS base was placed in a vessel.

2. The desired amount of CB particles were added to the PDMS base. In the experiments discussed below, CB concentration varied from 3-wt% to 17-wt% of the PDMS base. The CB-PDMS base mixture was mixed for 30 minutes, with the help of a mixer.

3. A cross-linking agent (CA) was added to the PDMS base at a ratio of PDMS base: CA of 10:1. The mixture was mixed for 5 minutes. Next, the composite was ready for processing. The pot life [2] of Alpa-Sil classic is about 15 minutes, so the preparation should be done immediately prior to processing. A small amount of isopropanol can be optionally added, to increase the pot life.

The test results (discussed in later sections) showed that CPDMS membranes fabricated as explained above had a poor surface profile and high resistivity. In the composite, the dispersion of CB particles inside the PDMS was poor and the CB particles were agglomerated together to form large particles.

In order to improve the dispersion of CB in PDMS, a solvent was used along with the CB and the PDMS. The solvent should improve the dispersion of CB particles and prevent the formation of large particles. Two types of solvents were considered: Solvents which are not soluble in PDMS (polar solvent) and solvents which are soluble (non-polar). Details of the composite preparation process are discussed below.

4.3.2 CB-Methanol-PDMS Composite Preparation

In this method, the polar solvent methanol [99] was used. It has the following advantages.

[2] Pot life is the time the PDMS retains its processing properties after final preparation

- Due to low solubility in PDMS [100], methanol can be removed easily after dispersing CB filler in CPDMS. Hence, during membrane fabrication, only a very small amount of methanol remains in the composite, which prevents changes in membrane dimensions due to solvent evaporation during fabrication.
- Methanol inhibits the cross-linking of PDMS and allows more time for patterning.
- Methanol is inexpensive and easily available.
- Considering safety, cost and environmental factors, methanol is listed as a 'recommended' solvent [101].
- Excess methanol can be reused after processing, which makes the fabrication process more cost-effective and environmentally friendly.

The steps followed for the preparation of CB-Methanol-PDMS composite were:

1. The required amount (the same as in the first method) of CB fillers was placed in a vessel. Methanol (three times the volume of CB) was added to the CB fillers. The mixture was ultra-sonicated for 15 minutes and then stirred for 1 hour with the help of a magnetic stirrer. The CB fillers were (partially) dissolved in methanol.
2. The PDMS base was immediately added to the CB-Methanol mixture. The composite was then stirred for another 30 minutes. As the composite was highly viscous, hand-mixing was carried out. During the process, the CB-PDMS base mixture started to settle on the bottom of the vessel and the methanol floated above the mixture. Excess methanol was poured-off the CB-PDMS base mixture.
3. The required amount of CA (PDMS:CA in a ratio of 10:1) was added to the CB-Methanol-PDMS base mixture and mixed for another 5 minutes.

4.3.3 CB-Toluene-PDMS Composite Preparation

In this composite preparation, toluene [102] was used as a solvent. Unlike methanol, toluene is soluble in PDMS [100], and it is not possible to separate PDMS and toluene after mixing. Hence, a different fabrication method was followed.

1. A required amount of CB particles (3-wt% to 23-wt% of the PDMS base) was added to the PDMS base component.
2. A small amount of toluene (1/10th volume of CB) was added to the CB-PDMS base mixture, which made the mixture less viscous. The CB-Toluene-PDMS base was stirred for 1 hour, using a magnetic stirrer.
3. The required amount of CA (PDMS base:CA in a ratio of 10:1) was added to the CB-Toluene-PDMS base mixture and mixed for another 5 minutes.

The composite prepared using this method was less viscous compared to the previous method (using methanol). Therefore, structuring using the CB-Toluene-PDMS composite was much easier than creating the CB-Methanol-PDMS composite.

4.4 Fabrication of Thin CPDMS Membranes

CPDMS composites prepared using the methods discussed above were highly viscous. Hence, they could not be spin-coated to fabricate a thin membrane. The steps followed for the fabricating of thin CPDMS membrane are illustrated in Fig 4.2. A printed circuit board (PCB), cut in the shape of a 4-inch wafer and shown in Fig. 4.2(a), was used as a substrate for the fabrication of CPDMS membranes. As a result of the poor adhesion of the PDMS to metal, fabricated CPDMS membranes can be easily peeled off from the PCB. Initially, a pure PDMS (Sylgard 184) was prepared by mixing the base component and the CA at a ratio of 10:1 and kept for 30 minutes to remove air bubbles. Next, the PDMS was deposited on the PCB substrate (shown in Fig. 4.2(b)) by spin-coating at a speed of 800 rpm for 15 s. The PCB substrate (with a deposited PDMS layer) was placed in an oven for 30 minutes at 80 ^{o}C. After curing the PDMS layer, a rectangular section was removed, thereby creating a master mold for the fabrication of CPDMS membranes, as illustrated in Fig 4.2(c). A piece of rectangular Scotch Tape was attached to the edge of the substrate as a peeling initiator, which helped peel off the CPDMS membrane after fabrication. The CPDMS composite was deposited into the mold and then spread across the region with a knife, as shown in Fig. 4.2(d). Similar fabrication procedures were used for CB-PDMS, CB-Methanol-PDMS and CB-Toluene-PDMS composites. The CB-PDMS and CB-Toluene-PDMS composites cross-link at room temperature; however, to remove excess toluene, CB-Toluene-PDMS was kept in an oven at 120 ^{o}C. On the other hand, in CB-Methanol-PDMS composites, methanol prevents PDMS cross-linking, so the composite was kept in an oven at 70 ^{o}C for 30 minutes. At this temperature the methanol evaporated and the PDMS composite started to cross-link. After curing, the CPDMS membrane was removed with the help of the peeling initiator and a roller made

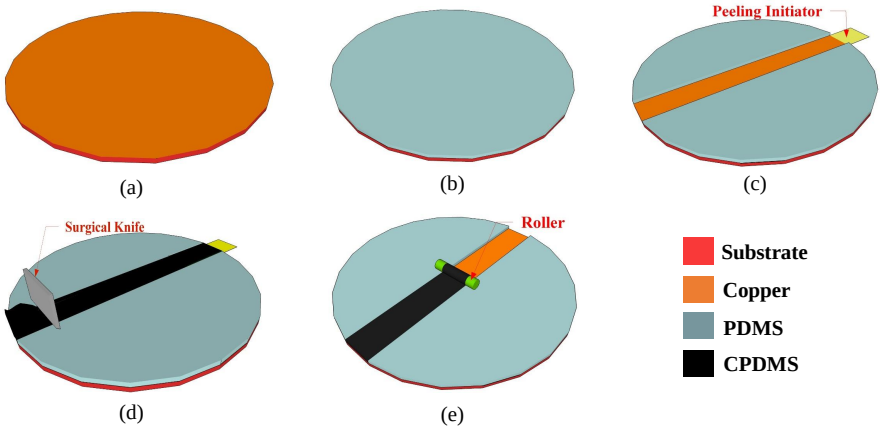

Figure 4.2: Fabrication process for soft, thin CPDMS membranes. (a) Template for membrane fabrication. (b) and (c) Patterning of the master mold. (d) Fabrication of CPDMS membranes. (e) Peeling off the fabricated membrane with the help of a peeling initiator and a roller.

of PDMS. The peeling initiator helped to lift the CPDMS membrane, which was then rolled off the substrate, as shown in Fig. 4.2(d). The roller helped to reduce the force on the membrane and prevent the membrane from tearing during peeling [103]. In addition, it prevented wrinkling and helped to store the membrane without contamination.

Magnified photographs (5x) of the fabricated CPDMS membranes, using CB-PDMS, CB-Methanol-PDMS and CB-Toluene-PDMS composites, with a CB concentration of 11-wt%, are shown in Fig. 4.3(a)(i), Fig. 4.3(a)(ii) and Fig. 4.3(a)(iii), respectively. The surface profile of the membranes, measured using a contact-type surface profilometer (Veeco Dektak 6M), is presented in Fig. 4.3(b). In the CB-PDMS composite, CB particles sticked together to form large particles which were responsible for the knife traces on the membrane. The use of a solvent improved the dispersion of CB in PDMS

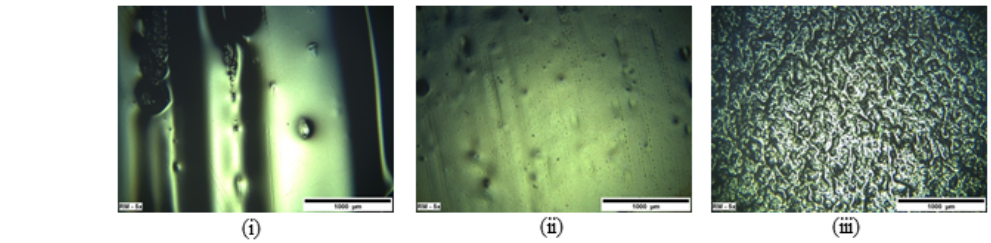

(a)

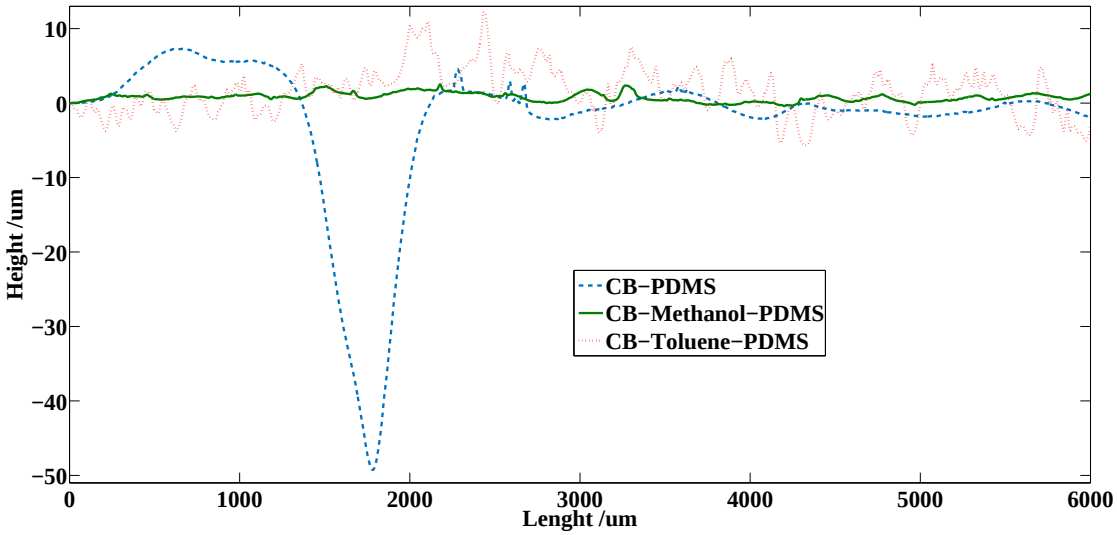

(b)

Figure 4.3: (a)Magnified photograph (5x) of the CPDMS (11-wt% CB) membrane fabricated from (i)CB-PDMS composite (ii)CB-Methanol-PDMS and (iii)CB-Toluene-PDMS composites. (b)Surface profile of the membranes in Fig. 4.3(a)

and prevented the formation of large CB particles. Hence, surface profiles of the membranes fabricated using CB-Methanol-PDMS and CB-Toluene-PDMS composites were much smoother compared to the CB-PDMS membranes. Comparing Fig. 4.3(a)(ii) and Fig. 4.3(a)(iii), membranes fabricated using methanol had a better surface profile. However, because of their better dispersion and low viscosity, the membrane fabrication process was much easier when using CB-Toluene-PDMS. The average thickness of CPDMS membranes fabricated using this method was also evaluated. Membranes fabricated using the CB-Methanol-PDMS composite had a thickness of 100±20 μm. The membrane fabricated using the CB-Toluene-PDMS composite was 70±20 μm thick. The membrane fabricated from CB-Toluene-PDMS composite was thinner because of excess toluene evaporating.

4.5 Resistive Characterization of the CPDMS membranes

4.5.1 Measurement Set-up

A simple two-point resistance measurement was used to characterize the fabricated membranes. The template used to measure the resistances of the membranes is shown in Fig. 4.4. It was etched out of a printed circuit board, using a standard etching procedure, and consisted of four measuring areas (S_1, S_2, S_3 and S_4). The CPDMS membranes were placed on top of these measuring areas. Two electrodes were provided on each measuring area to connect the CPDMS membrane to the measurement circuit. Suitable dimensional markings were given in the measuring areas, in order to ensure that all the membrane samples had the same surface area. A constant DC voltage source, V, was

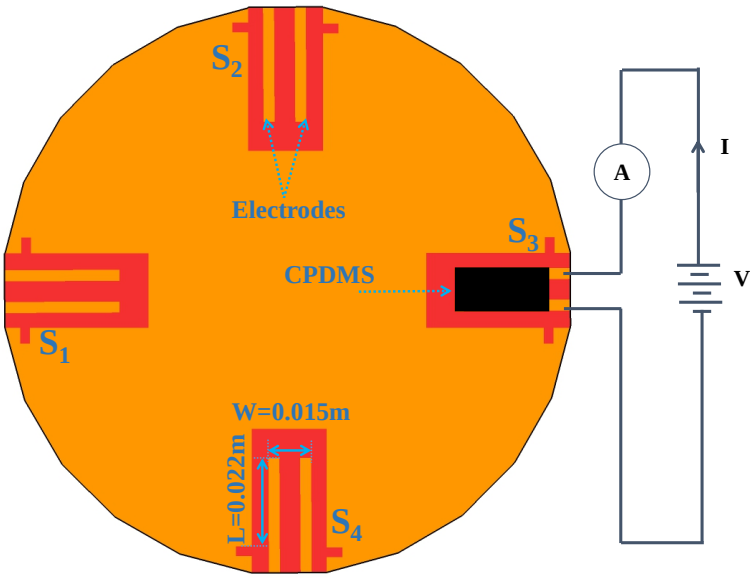

Figure 4.4: Set-up for measuring the CPDMS membrane resistance

connected across the membrane. Current (I) through the membrane was measured using an ammeter (A) connected in a series. The membrane resistance (R_m) can be evaluated using Ohm's law ($R_m = V/I$). The membrane resistivity (ρ_m) was calculated using the following formula:

$$\rho_m = R_m \frac{L.t}{W} \tag{4.1}$$

where W is the distance between copper electrodes, L is the length of the copper electrode, and t is the thickness of the CPDMS membrane.

4.5.2 Resistivity Variation with CB Concentration

The resistivity of CPDMS membranes fabricated using the different composites (discussed in Section 4.3) with different CB concentrations was evaluated. The fabricated membranes were kept on the measurement template. Voltage (V) varied from 0 to 30 V and the current through the membranes was recorded from ammeter (A). CPDMS membranes (with CB concentrations more than the percolation threshold) showed resistor-like linear characteristics. The voltage-current (V-I) characteristics of the membranes fabricated using CB-Methanol-PDMS composite with CB concentrations of 5-wt%, 11-wt%, and 17-wt% are shown in Fig. 4.5. The slope of the $V - I$ characteristics represents R_m. The ρ_m of the CPDMS membranes was evaluated using Equation (4.1). The ρ_m of the membranes fabricated from CB-PDMS, CB-Methanol-PDMS and CB-Toluene-PDMS for different CB concentrations is plotted in Fig. 4.6(a), Fig. 4.6(b) and Fig. 4.6(c), respectively. For each concentration, average resistivity and variations among the eight membrane samples are shown. Membranes fabricated from the CB-PDMS composite became conductive when CB concentration reached 11-wt%, while membranes using CB-Methanol-PDMS or CB-Toluene-PDMS composite showed this behavior at

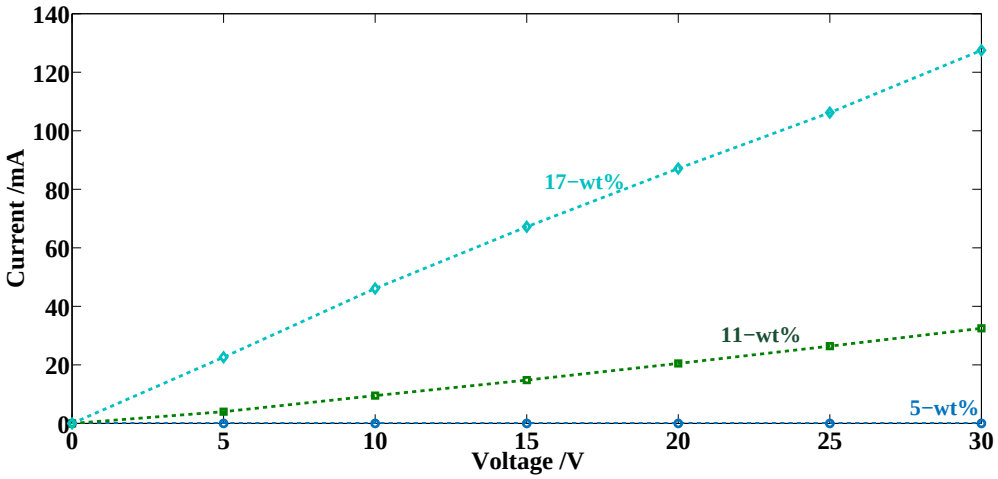

Figure 4.5: Voltage-current relationship recorded for CPDMS membranes fabricated using CB-Methanol-PDMS composite for different CB concentrations.

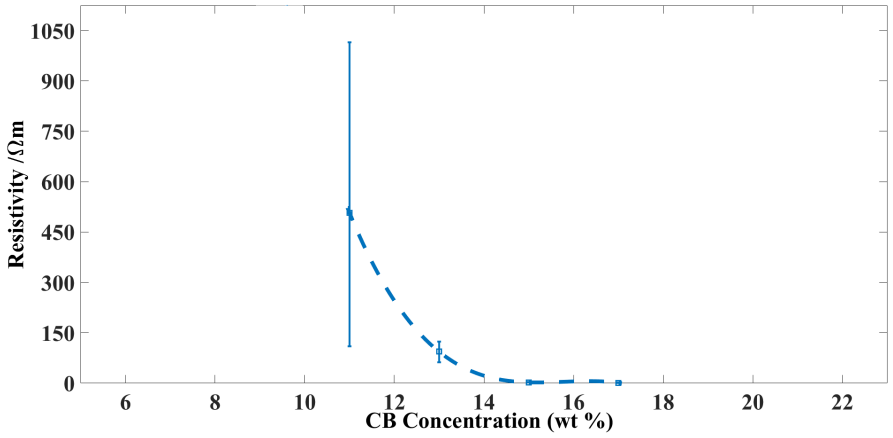

(a)

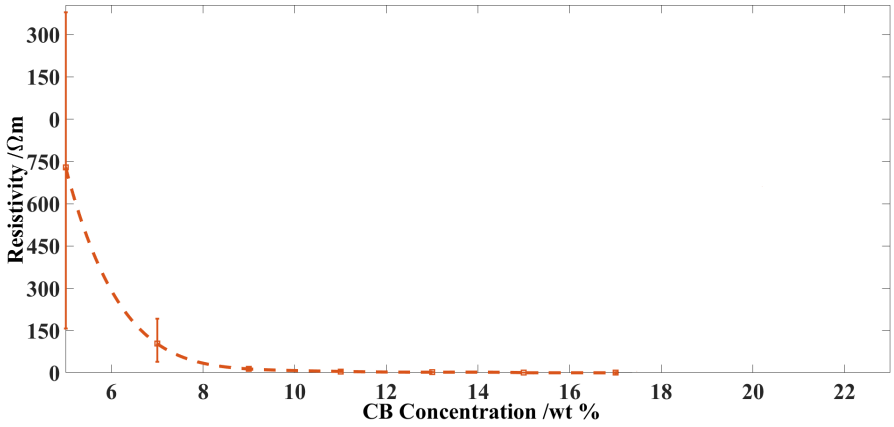

(b)

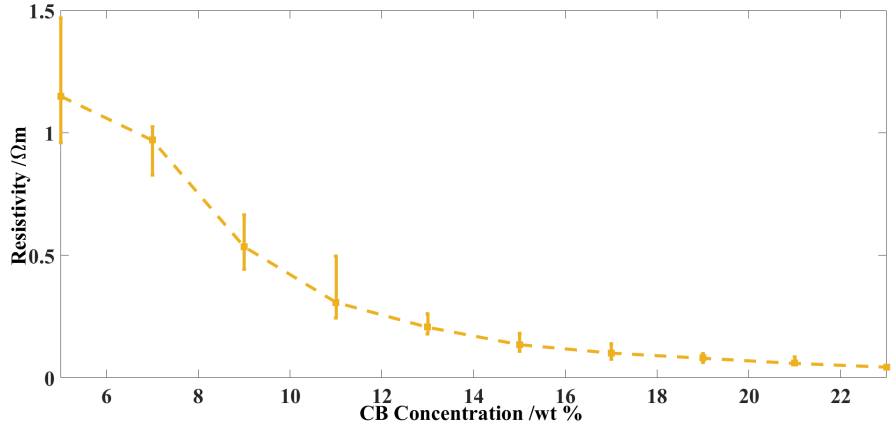

(c)

Figure 4.6: Variation in resistivity of membranes fabricated using (a) CB-PDMS (b) CB-Methanol-PDMS and (c) CB-Toluene-PDMS, for different CB concentrations.

a much lower CB concentration of 5-wt%. Further increases of CB concentration decreased the resistivity. Comparing Fig. 4.6(a), Fig. 4.6(b), and Fig. 4.6(c), it is clear that membranes fabricated from CB-Methanol-PDMS and CB-Toluene-PDMS had a lower percolation threshold than membranes fabricated using a CB-PDMS composite. In addition, for the same CB concentration, membranes fabricated with CB-Toluene-PDMS showed much lower resistivity than CB-Methanol-PDMS, which was lower than the membrane fabricated using CB-PDMS. The result showed that the use of solvent improved the dispersion of CB particles in PDMS. Within the solvents, toluene (a non-polar solvent), which is soluble in PDMS, showed better dispersion than the methanol (polar solvent).

4.5.3 Resistance Variation with Pressure

Theory and Modeling

Pressure sensitivity of CB filled silicone composites are well studied [104]- [106]. It has been shown that the piezoresistivity of CB filled PDMS is due to variation of separation between CB particles.

The piezoresistivity of CPDMS can be explained using Fig. 4.7. Let's assume l_{z0} and l_{x0} are inter-particle separation along Z-axis and X-axis, respectively, under zero pressure. From [105],

$$l_{z0} = l_{y0} = d[(\frac{\pi}{6\phi})^{(1/3)} - 1], \tag{4.2}$$

where d and ϕ are the diameter and volume fraction of the filler particles. The application of pressure deforms the CPDMS membrane and varies the inter-particle separation. The inter-particle separations under pressure along Z axis will be

$$l_z = l_{z0}(1 - \epsilon_z) \tag{4.3}$$

and

$$l_x = l_{x0}(1 + \mu\epsilon_z), \tag{4.4}$$

where ϵ_z is the strain of CPDMS membrane along Z axis, and μ is the Poisson's ratio. From Equations (4.3) and (4.4), l_{z0} decreases to l_z, while l_{x0} increases to l_x. In case

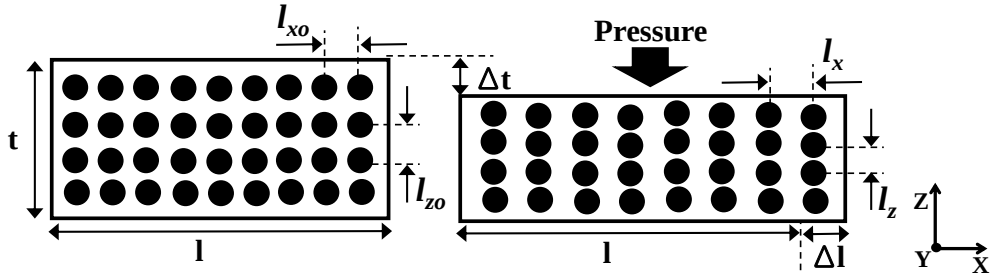

Figure 4.7: Variation in inter-particle separation due to applied pressure.

of resistance measurement using planar electrodes, the effect of l_{x0} is dominant. Under this condition, resistance between CB particles can be expressed as [105]

$$R = R_0 \frac{l_x}{l_{x0}} e^{\gamma(l_x - l_{x0})}, \tag{4.5}$$

where

$$\gamma = \frac{4\pi}{h}\sqrt{2m\phi}. \tag{4.6}$$

Here, R_0 is resistance between CB particle under zero pressure, h is the Plank's constant, m is the electron mass and ϕ the height of the potential barrier between the adjacent particle. From Equation (4.5), as $l_x > l_{x0}$, resistances of the membrane increases with increase of pressure. Furthermore, with the increase of CB concentration, l_{x0} and l_{z0} decreases, which reduces R_0 and R. Hence, at high CB concentrations the CPDMS membranes are expected to show lower sensitivity to pressure variations.

Experimental Setup and Results

CPDMS membranes with a thickness of 250 μm were used for the experiment. The membranes fabricated from CB-Methanol-PDMS composite are considered as the best choice for sensor applications because of its better surface profile, environment friendliness, cost-effectiveness, etc. (details are discussed in Section 5.5), hence only those membranes were tested for piezoresistiviy. The set-up developed for verifying the piezoresistivity of the CPDMS membranes is shown in Fig. 4.8. It consisted of a known mass (m) placed on a supporting platform. The force on the platform is $F = mg$, where g is acceleration due

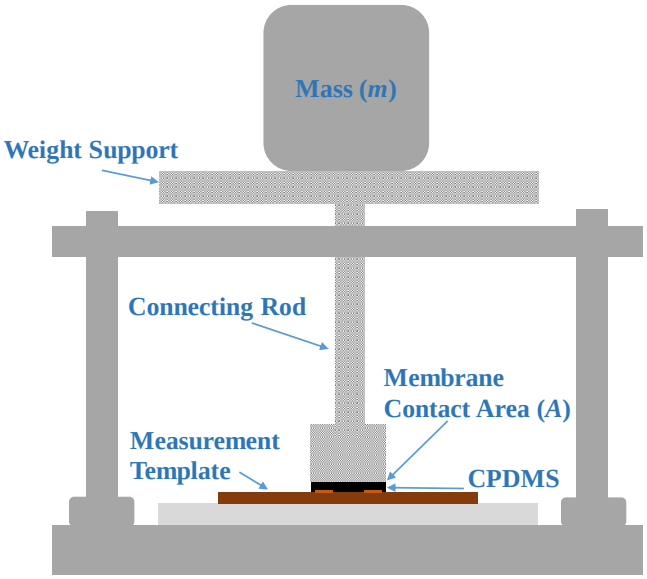

Figure 4.8: Set-up used for applying pressure to CPDMS membranes

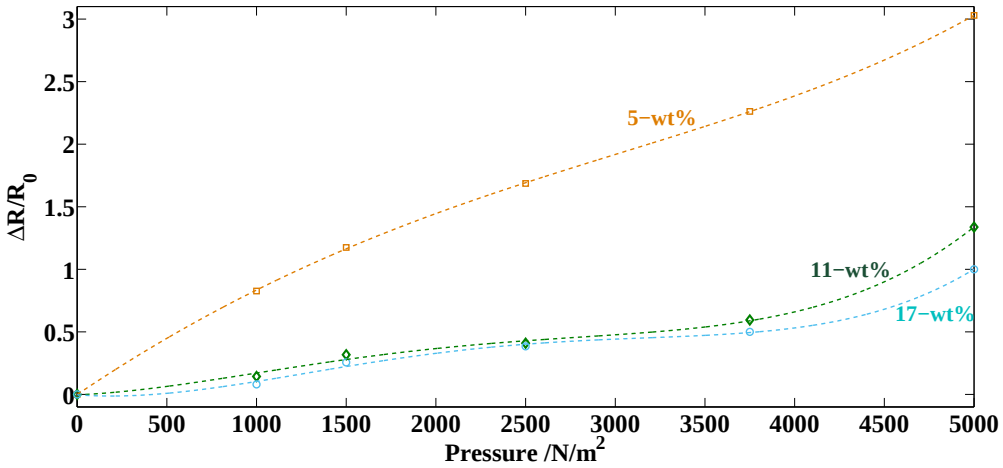

Figure 4.9: Relative change of the resistance recorded for a soft CPDMS membrane with an increase of pressure

to gravity. The platform was connected to one end of a connecting rod, the other end of which had a surface area A, which transferred F to the membranes on the measurement template. F was distributed equally on the membrane. Pressure acting on the membrane could be calculated using the formula $P = F/A$. An insulating tape was attached to the surface area, to electrically insulate the set-up from the membranes. Different pressure loads were applied to the CPDMS membrane by varying m. The corresponding resistance was measured using the two-point resistance measurement method. The relative change of the resistance recorded from the membranes with applied pressure is shown in Fig. 4.9. As expected, the resistance of the CPDMS membrane increases with increase of pressure, and the pressure sensitivity of the membrane resistance decreases with increase in CB concentration.

4.5.4 Resistance Variation with Temperature

The thermal stability of CPDMS membranes is important for unique and unclonable sensor applications, and so the effect of ambient temperature variations on the membrane resistance is discussed in this section. CPDMS membranes with a thickness of 250 μm were fabricated using CB-Methanol-PDMS composites. The membranes were attached to the measurement template and kept in an oven, the temperature of which was increased from 30^{o}C to 110^{o}C. The membrane resistance was measured at increments of 20^{o}C, using the same two-point measurement method. In order to make sure the temperature of the membrane was the same as the oven, the membranes were kept at a certain temperature for 30 minutes, before taking the measurements. The relative change of the resistance recorded for membranes fabricated with different CB concentrations is shown in Fig. 4.10. Two effects need to be considered while analyzing the results:

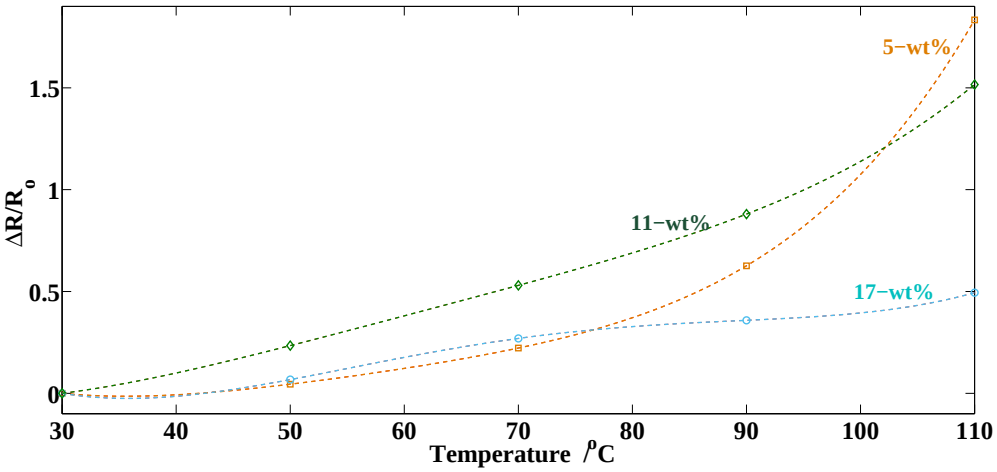

Figure 4.10: Relative change of the resistance recorded for CPDMS membranes following an increase of ambient temperature

1. Negative Temperature Coefficient (NTC) of CB-filled PDMS: The tunneling current in the CB filled PDMS increases with an increase of temperature, which results in a decrease of the CPDMS membrane resistance [107].

2. Thermal expansion of PDMS: Similar to the pressure, a variation of temperature varies the stain on the PDMS, and changes the inter-particle separation. In this case, the inter-particle separation can be expressed

$$l_x = l_{x0}(1 + \alpha \Delta T), \tag{4.7}$$

where l_{x0} is the initial inter-particle separation, α is the temperature expansion coefficient of PDMS and ΔT is the change in temperature. The increase in temperature, increases the distance between CB particles, and from Equation (4.5), it subsequently increase the membrane resistance.

From Fig. 4.10, the effects of thermal expansions were dominant for higher CB concentrations, 11-wt% and 17-wt%. Hence, the CPDMS membrane resistance increased in line with temperature. Furthermore, because of lower inter-particle distance, the variation of the membrane resistance with respect to temperature decreases with increase in CB concentration. The membrane at the percolation threshold showed different behavior. At lower temperatures, the membrane resistance was insensitive to temperature variations, while at high temperatures resistance variation was high. The reason could be, at low temperatures the NTC effect might cancel out the effect of thermal expansion. With an increase of temperature, the thermal expansion effect started to dominate, and resistance increased accordingly.

In order to ensure that the measurement set-up had no effect on the recorded output, a standard resistor of almost the same resistance as that of the membranes was connected to the measurement template. The template was kept in the oven and the

same measurement procedure was carried out. Constant resistance was measured at all temperature levels, so the outputs recorded in Fig. 4.10 show the effect of temperature on a conductive membrane alone and are independent of the measurement set-up.

4.5.5 Resistance Variation over Time

The stability of the CPDMS membrane resistance over time was studied. The resistance of the fabricated membranes was recorded in a laboratory environment for a period of five days. The outputs recorded are shown in Fig. 4.11. Resistance decreased within the first three days and then settled down to a constant value. PDMS might not have been completely cured and it may take a few days to fully cross-link it, because of methanol, or the absorption of atmospheric moisture reached a limit. This study showed that the CPDMS membrane needs to be fabricated at least three days before using it for any application.

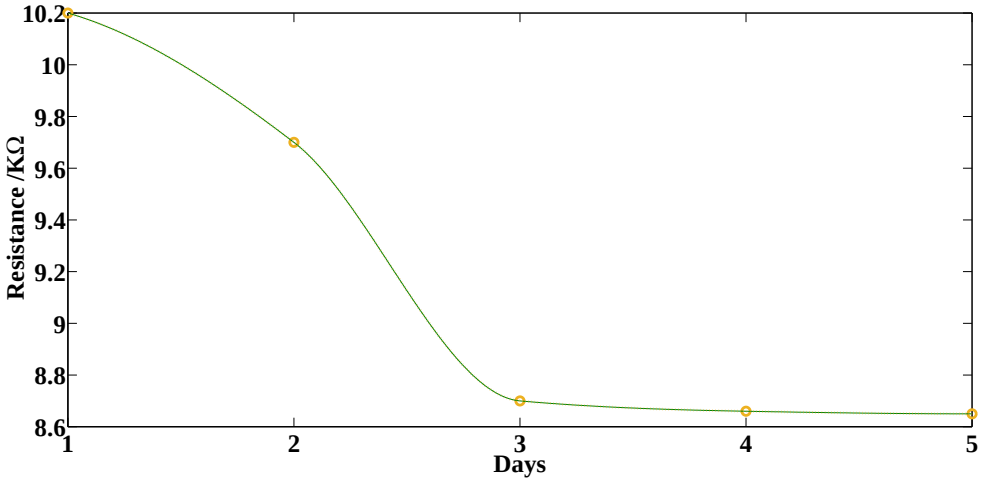

Figure 4.11: Resistance of the membrane recorded for a duration of five days.

4.6 Mechanical Characteristics

The mechanical characteristics of soft, thin CPDMS membranes are discussed in this section. The CB particle inside PDMS modifies the mechanical properties of the membrane. Mechanical properties such as the Young's modulus, elastic limit and fracture point of the membrane can be derived from the stress-strain relationship.

4.6.1 Measurement Set-up and Procedure

The most common way to measure the stress-strain relationship of a material is via uniaxial tensile testing [108], which measures variations in the length of the material being tested, against an applied force. A simple uniaxial tensile testing set-up, shown

in Fig. 4.12, was developed for this study. Device specifications were customized to characterize thin, soft membranes. A sample membrane can be loaded between a fixed and movable grip. The markings in the grips help to align the membrane properly. The fixed grip is attached to the frame. The movable grip is connected to a cord through a dynamometer. The membrane can be mechanically loaded by manually pulling a cord. Under this condition, stress on the membrane is given as:

$$\sigma_m = \frac{F}{A}, \tag{4.8}$$

where F is the force applied to the membrane and A is the area on which the force is applied. F can be read from the dynamometer, and A can be calculated by multiplying gauge width (W) and membrane thickness (t). Any variation in membrane length can be read by a ruler. Strain can be calculated using Equation (4.9).

$$\epsilon = \frac{L - L_0}{L_0}. \tag{4.9}$$

Here, L_0 is the initial length when F is zero. L is the length of the membrane after applying F.

The stress-strain relationship of a membrane can be determined using the following steps:

1. Load the sample between the fixed and movable grips.

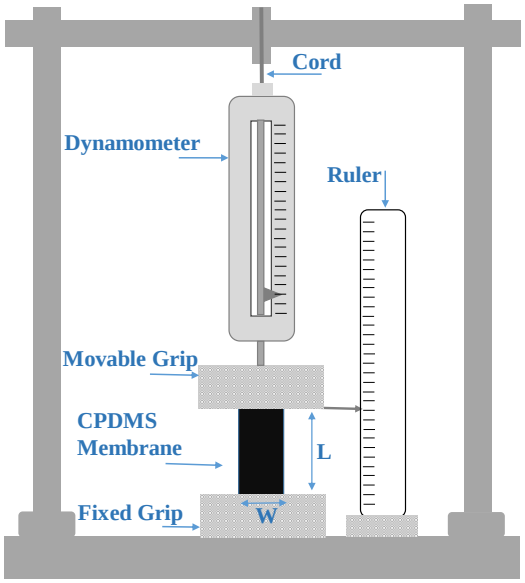

Figure 4.12: Uniaxial tensile test set-up built for measuring the stress-strain characteristics of CPDMS membranes

2. Pull the cord until the membrane is straight and not sagging. Record the dynamometer reading as offset force. Also, note the initial length, L_0, from the ruler.

3. Increase force on the membrane by pulling the cord and recording the gauge length (L) of the membrane for every increment of 0.1 N force.

4. Evaluate strain and stress values using Equations (4.8) and (4.9).

For any material at low strain values, the stress-strain relationship is linear. This region is called the 'elastic region', within which deformation is reversible after releasing force. According to Hooke's law, the slope of the elastic region gives the value of the Young's modulus. After this region, stress-strain the material loses its elasticity and the relationship is non-linear.

The developed tensile testing device was validated before characterizing a CPDMS membrane. A pure PDMS membrane, 2.5 cm × 1.5 cm × 0.5 cm in size, was fabricated by mixing PDMS Sylgard 184 to a ratio of 10:1 and cross-linked at 125^{o}C. With the measurement set-up, the membrane showed an average Young's modulus of 2.42 MPa, which was comparable with the value of 2.46 MPa, determined using a commercially available tensile testing device in [109]. This showed that the developed test set-up was accurate and could be used for measuring stress-strain characteristics for CPDMS membranes.

4.6.2 Young's Modulus Variation with CB Concentration

The mechanical characteristics of CPDMS membranes were studied. Similar CPDMS membrane samples, fabricated for electrical characterization, were used for mechanical

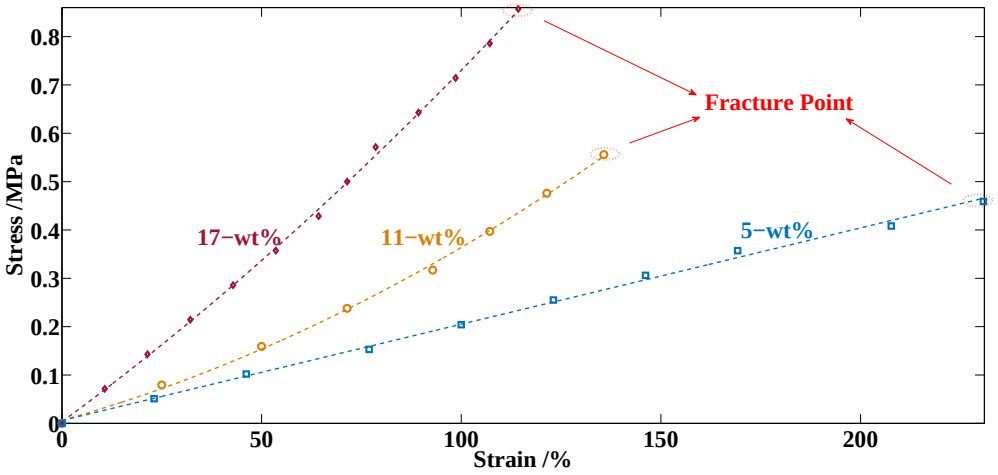

Figure 4.13: Stress-strain relationship recorded for the CPDMS membrane, fabricated using CB-Methanol-PDMS composite

characterization. As the membranes fabricated from CB-PDMS showed very poor resistivity, surface profile and high percolation threshold, those membranes are not suitable for sensing applications. Hence, only membranes fabricated from CB-Methanol-PDMS and CB-Toluene-PDMS composite were characterized. The stress-strain values recorded for the CPDMS membrane made of CB-Methanol-PDMS composites, with CB concentrations 5-wt%, 11-wt%, and 17-wt%, are plotted in Fig. 4.13. The elasticity of the membrane dropped down with an increase of CB concentration. A PDMS membrane with 5-wt% CB was strained up to 240%, while membranes with a 17-wt% CB concentration broke when the strain reached a value of about 120%. Since high CB concentration increases the stiffness of a membrane, it can withstand higher stresses before breaking at lower strain values. These results are in a good agreement with expectations. The linear elastic region of the membranes was up to 50% strain. Beyond this limit, mechanical deformations were not reversible. Strain on the membrane expanded the PDMS and increased the inter-particle distance, which resulted in increase of resistivity. When the membrane was strained beyond the linear elastic limit, this change in resistivity was not reversible, and in some cases it destroyed the conductivity property of the membrane. Hence, stress on the membrane should always be below the elastic limit. The initiator-roller arrangement used in the fabrication process helped reduce stress on the membrane while peeling. Similar results were also observed from a membrane fabricated using CB-Toluene composite. The Young's moduli of the CPDMS membranes fabricated using both composites for different CB concentrations were evaluated from the slope of the linear elastic region of the stress-strain graph, plotted in Fig. 4.14. At each concentration, the average and deviation of the Young's modulus for each of the eight membrane samples is shown. The Young's modulus of the CPDMS membrane increased exponentially with an increase of CB concentration. The membrane fabricated from CB-Methanol-PDMS composite showed a slightly lower Young's modulus than the

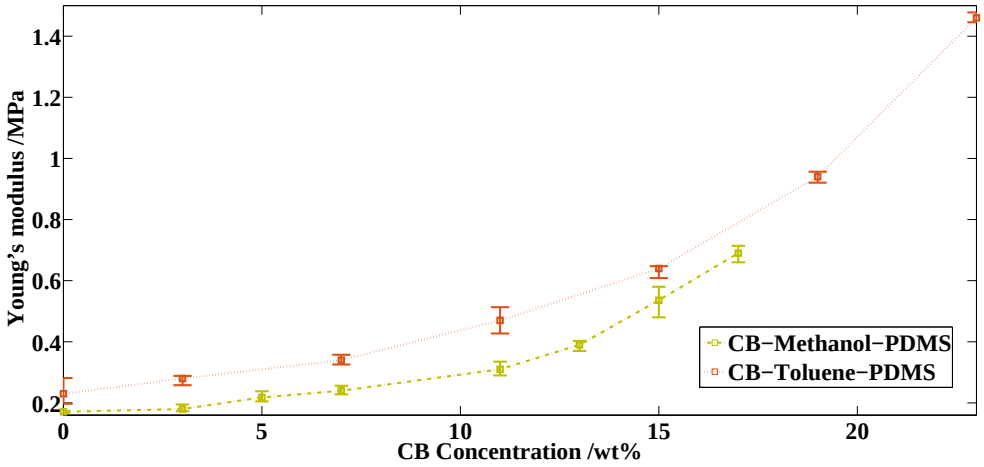

Figure 4.14: Youngs modulus variation in the CPDMS membrane for different CB concentrations

membrane fabricated from CB-Toluene-PDMS composite, possibly either because of the presence of un-evaporated toluene in the membrane or an error due to limited resolution of the measurement set-up.

4.7 Applications of CPDMS Membrane

The main application of the thin-soft CPDMS membranes, is in miniaturized capacitive sensors. CPDMS membranes are used as active functional element in miniaturized capacitive sensors. The details are discussed in the next chapter.

Apart from unique and unclonable sensors, the fabrication process and results discussed in this chapter are useful for developing CPDMS structures/elements for other applications. Some of the applications for which the CPDMS may be considered are given below:

- As discussed in Section 4.5.3, CPDMS at the percolation threshold showed high piezo-resistivity, so it can be considered for developing flexible strain gauge sensors, pressure sensors, etc.
- As discussed in Section 4.5.4, the resistance of the CPDMS varied according to temperature. This characteristic of the membrane can be utilized for developing flexible temperature sensors.
- CPDMS with a high CB concentration offered high conductivity. At a CB concentration of 23-wt% the CPDMS membrane (CB-Toluene-PDMS composite) exhibited a conductivity of 28 S/m and a Young's modulus of 1.4 MPa. These membranes can be used as flexible electrodes in applications such as wearable devices.

4.8 Conclusion

The fabrication and characterization of soft, thin conductive PDMS membranes is reported. CPDMS composite was prepared by mixing CB fillers into a PDMS matrix. The composite was then patterned to a soft, thin, conductive membrane using a simple fabrication process. In this study, three different types of CPDMS composites were prepared: CB-PDMS, CB-Methanol-PDMS and CB-Toluene-PDMS composites. Membranes fabricated using these composites, all with different CB concentrations, were characterized to determine and compare their electromechanical properties. Variations in the electromechanical properties of the CPDMS membrane with a CB concentration were also studied. The experimental results showed that the addition of solvents (methanol/toluene) during composite preparation improved the dispersion of CB particles in PDMS, and membranes fabricated using these composites showed better surface profiles. Furthermore, membranes prepared using CB-PDMS composite became conductive (percolation threshold) when the CB concentration was 11-wt%, while membranes prepared using CB-Methanol-PDMS and CB-Toluene-PDMS composites exhibited this

behavior at a much lower CB concentration of 5-wt%. With a further increase of CB concentration:

- The resistivity of the membrane decreased and saturated to a constant value.
- The Young's modulus of the membrane exponentially increased.

Membranes fabricated from CB-Methanol-PDMS composite showed better surface profiles and lower Young's moduli, while the membrane fabricated using CB-Toluene-PDMS composite showed lower resistivity. These electromechanical characteristics are later (in next Chapter) used to determine the optimum CB concentration in CPDMS membrane for miniaturized capacitive sensors.

5 Miniaturized Capacitive Sensor with Unique and Unclonable Characteristic

5.1 Introduction

The dual/differential electrode capacitive sensor structures discussed in Chapter 2 and Chapter 3 have relatively large surface areas. Reducing surface area affects the sensitivity and the uniqueness of the sensor. The presence of the C_{FG} dominant region restricts sensitivity improvements by reducing the distance between the electrode and conductive balls (t_d) and/or increasing the mass of the functional element. Therefore, dual/differential electrode sensor designs are unsuitable for many space-limited applications.

In dual/differential electrode sensors, only conductive balls actively participate in sensing, covering 30% of the active functional element volume. The PDMS constitutes the remaining 70%. As the dielectric constant (ϵ_r) of the PDMS is low ($\epsilon_r = 2.75$), 70% of the active functional element volume has only negligible effects. Increasing the number of conductive balls increases their density in the active functional element and results in higher sensitivity. However, it reduces the uniqueness of the sensor.

This chapter presents design of a miniaturized capacitive sensor with unique and unclonable characteristic. The sensor uses a CPDMS (discussed in Chapter 4) structure with conductive balls as the functional element. Here, the whole active region of the functional element actively contributes to the sensing process, which helps to achieve higher sensitivity alongside a reduction in size. Details of the sensor design, analytical model, simulation studies, fabrication and results are discussed in the following sections.

5.2 Sensor Design

5.2.1 Sensor Structure

The detailed 2D structure of the miniaturized capacitive sensor is shown in the Fig. 5.1. The sensor uses a CPDMS structure with conductive balls as the functional element. These balls are randomly distributed on the functional element. The sensor substrate consists of four electrodes: A transmitter (T), a receiver (R), ground (G), and ground/guard (Gr). The functional element is attached to the sensor substrate and electrically connected to R. As the functional element is conductive, it has the same potential as R. The CPDMS membrane above the T is the active area of the functional element, and T and the CPDMS membrane form a parallel plate capacitor. External forces such as pressure, tilt or acceleration deflect the CPDMS membrane. Owing to

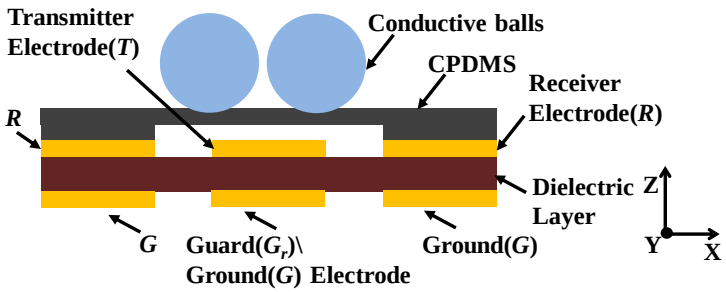

Figure 5.1: Cross sectional view of miniaturized capacitive sensor structure

random ball distribution, the deflection of the CPDMS membrane for the same force is unique for each sensor. This deflection of the CPDMS membrane varies in its distance from T, which in turn changes capacitance between them. G is provided to reduce the effect of external interference. The sensor also consists of an additional electrode (Gr) so that the same sensor structure can be used as both, single-electrode and dual-electrode sensor. Details are presented in section 5.2.3.

5.2.2 Functional Element: Square and circular

To understand better the deflection characteristics of the CPDMS membrane, a force diagram is presented in Fig. 5.2(a). In the case of tilt, the only force acting on the CPDMS membrane is gravitational force F_g, which can be resolved into the following

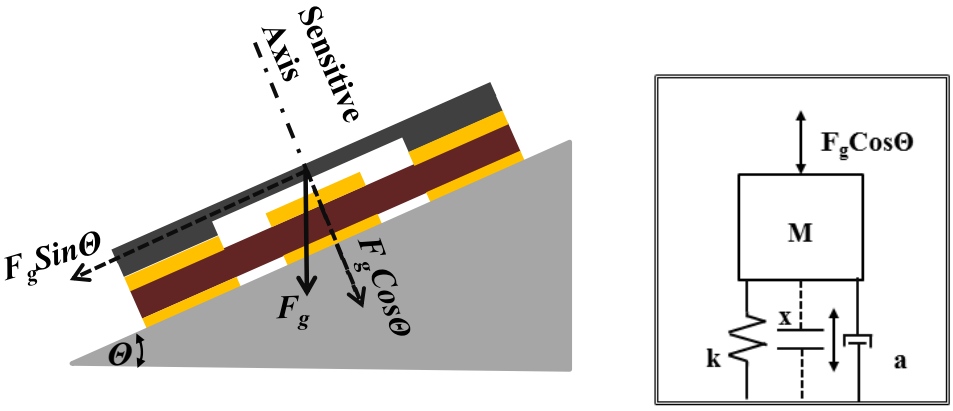

(a) (b)

Figure 5.2: (a)Force diagram: (b) Mechanical equivalent model of the miniaturized capacitive sensor

components:

$$F_n = F_g \cos\theta \tag{5.1}$$

and

$$F_p = F_g \sin\theta \tag{5.2}$$

where θ is the tilt angle. F_g is always constant, while its components F_n and F_p vary with the tilt angle θ. F_n moves the CPDMS membrane perpendicular to the sensor structure. F_p tends to move the CPDMS membrane parallel to the sensor structure, but the clamped sides restrict any movement. Hence, CPDMS membrane movement due to F_p is neglected. In this case, the CPDMS membrane can be viewed as a spring-mass-damper system with a perpendicular force F_n applied to it, as shown in Fig. 5.2(b). Tilt varies the magnitude of F_n, which in turn changes the position (x) of the mass. The model shown in Fig. 5.2(b) is also valid for pressure and acceleration ($\pm Z$ axis), in which case F_n represents force caused by pressure or acceleration.

The movement of the mass through tilting deflects the CPDMS membrane. The deflection profile of the CPDMS membrane depends on its shape (of the active area) and mass distribution. Both square and circular CPDMS membranes are considered for the miniaturized sensor. To study the effect of shape on the deflection of the CPDMS membrane, it is assumed that the total mass is equally distributed on the active area of the CPDMS membrane. The deflection of square and circular CPDMS membranes, when a perpendicular force is applied, is:

$$w_s(x,y) = w_{s0}(1 - 4\frac{x^2}{L_m^2})^2(1 - 4\frac{y^2}{L_m^2})^2 \tag{5.3}$$

and

$$w_c(r) = w_{c0}(1 - \frac{r^2}{R_m^2})^2, \tag{5.4}$$

respectively [110]. Here, $w_s(x,y)$ is the deflection of the square CPDMS membrane at coordinates x and y, L_m is the length of the square CPDMS membrane, w_{s0} is deflection at the center ($x = 0, y = 0$) for the square CPDMS membrane, $w_c(r)$ is the deflection of the circular CPDMS membrane at radius r from the center, R_m is the radius of the circular CPDMS membrane and w_{s0} is deflection at the center ($r = 0$) for the circular CPDMS membrane. For both CPDMS membranes, deflection is at its maximum in the center. Deflection in the center, for the square and circular CPDMS membranes [110], is:

$$w_{s0} = \frac{L_m^4(1-\mu^2)}{66E_Y t^3 A}F \tag{5.5}$$

and

$$w_{c0} = \frac{3R_m^4(1-\mu^2)}{16E_Y t^3 A}F \tag{5.6}$$

where μ is the Poisson's ratio, E_Y is the Young's modulus, t is the thickness and A is the area of the CPDMS membrane. F is the force acting on the CPDMS membrane.

For tilt, (5.5) and (5.6) are modified as:

$$w_{s0} = \frac{L_m^4(1-\mu^2)}{66E_Y t^3 A} F_g Cos\theta \tag{5.7}$$

and

$$w_{c0} = \frac{3R_m^4(1-\mu^2)}{16E_Y t^3 A} F_g Cos\theta \tag{5.8}$$

Using equations (5.3) and (5.4), the average deflection of the square and circular CPDMS membranes can be evaluated as:

$$w_{s(avg)} = \frac{\iint_{-L_m/2}^{+L_m/2} w_s(x,y)dxdy}{L_m^2} = \frac{64}{225} w_{s0} \tag{5.9}$$

and

$$w_{c(avg)} = \frac{\int_0^{R_m} 2\pi r w_c(r)dr}{\pi R_m^2} = \frac{1}{3} w_{c0}. \tag{5.10}$$

After substituting equations (5.7) and (5.8), Equations (5.9) and (5.10) will be:

$$w_{s(avg)} = \frac{64L_m^4(1-\mu^2)}{14850E_Y t^3 A} F_g Cos\theta \tag{5.11}$$

and

$$w_{c(avg)} = \frac{3R_m^4(1-\mu^2)}{48E_Y t^3 A} F_g Cos\theta. \tag{5.12}$$

From equations (5.11) and (5.12), using the same area, the circular CPDMS membrane has a 1.4 times higher average deflection than the square CPDMS membrane. Hence, for the miniaturized capacitive sensor, the circular CPDMS membrane is expected to offer better sensitivity.

5.2.3 Electrode configurations: Single and dual-electrode

Capacitive electrodes convert the functional element deflection into a change in capacitance. As discussed in Section 2.2.2, depending on the measurement technique, capacitive sensors can be either single- or dual-electrode sensors. In a single-electrode configuration, one of the two electrodes is grounded, whereas in the dual-electrode version neither of the electrodes is grounded. The effectiveness of both electrode configurations for converting the deflection of the functional element into a change in capacitance is evaluated herein.

The electrical equivalent model of the proposed sensor is shown in Fig. 5.3. C_{TP} represents capacitance between terminal T and the CPDMS membrane, when the CPDMS membrane is in the null position. The deflection of the CPDMS membrane, due to tilt, changes C_{TP}. The movement of the CPDMS membrane towards T decreases the distance between them, and C_{TP} increases. Similarly, the movement of the CPDMS membrane away from T decreases C_{TP}. Therefore, capacitance between T and the CPDMS membrane can be represented as $C_{TP} \pm \Delta C_{TP}$. ΔC_{TP} is the change in capacitance due to

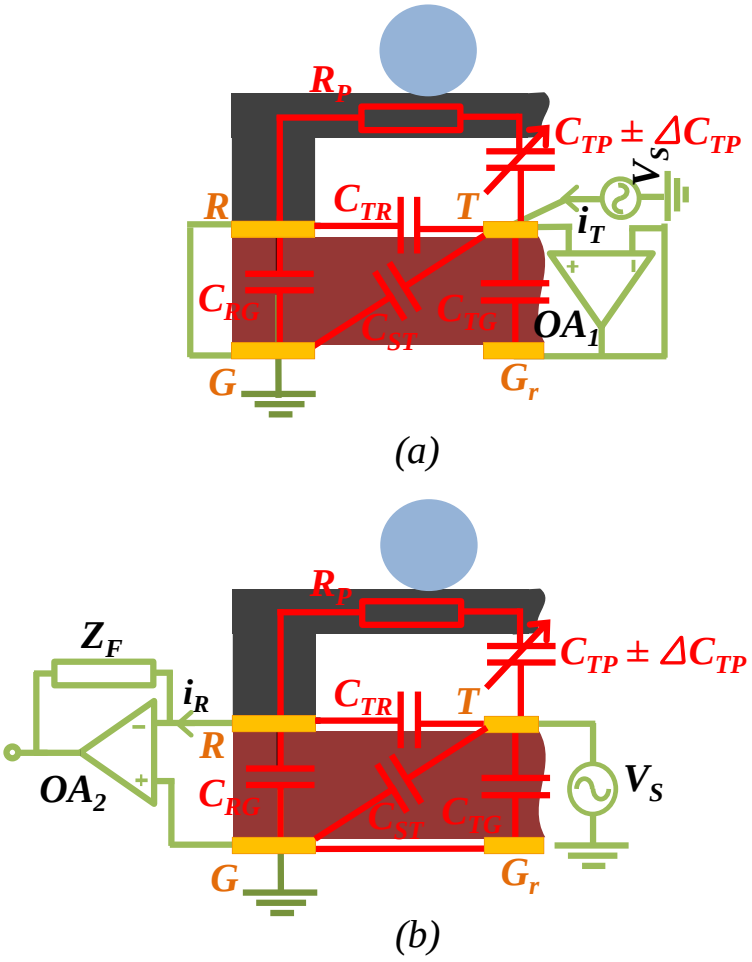

Figure 5.3: Electrical equivalent of the miniaturized capacitive sensor with (a) Single (or grounded) electrode configuration. (b) Dual-electrode configuration

tilt. The other capacitors C_{TR}, C_{TG}, C_{ST} and C_{RG} represent capacitances between the terminals T and R, T and G_r, T and G, and R and G, respectively. These capacitors are constant. In this model, leakage resistance across the capacitors is neglected. The functional element is fabricated using CPDMS, which is not a pure conductor and does have some resistance. The resistor R_P represents the resistance of the CPDMS functional element.

Fig. 5.3(a) shows the electrical equivalent of the miniaturized sensor with a single-electrode measurement configuration. Here, T is excited by a sinusoidal signal V_S, while R is grounded. Sensor capacitance is measured from the transmitter current i_T. In the single-electrode measurement configuration, G_r is set as a guard electrode [111]. A voltage follower (OA_1) drives G_r and keeps it at the same potential as that of T. As both T and G_r have equal potential, no current flows through C_{TG}. Hence, the sensor

capacitance is independent of the fixed C_{TG}. Similarly, as R is connected to G, C_{RG} also has no effect on the sensor capacitance. Under these conditions, if R_P is neglected, the sensor capacitance C_S can be expressed as:

$$C_S = C_{TR} + C_{ST} + C_{TP} \pm \Delta C_{TP}. \tag{5.13}$$

C_S is a parallel combination of the variable capacitance ΔC_{TP} and the fixed capacitances C_{TR}, C_{ST}, and C_{TP}.

The electrical equivalent of a miniaturized sensor with a dual-electrode measurement configuration is highlighted in Fig. 5.3(b). Here, sensor capacitance is measured using the receiver current i_R. The capacitors C_{TG} and C_{ST} are connected across V_S. Hence, the receiver current i_R is independent of these capacitors. To measure i_R, R is connected to the inverting terminal of the current-to-voltage converter (built around OA_2). As the inverting terminal of the converter has floating ground potential and G is grounded, no current flows through C_{RG}. Hence, in a dual-electrode set-up, the sensor capacitance is:

$$C_S = C_{TR} + C_{TP} \pm \Delta C_{TP}, \tag{5.14}$$

where C_{TR} and C_{TP} are the fixed components and ΔC_{TP} is the variable component. Comparing Equations (5.14) and (5.13), the dual-electrode measurement configuration leads to a sensor capacitance independent of the fixed capacitor C_{ST}, as compared to single-electrode configurations. In the miniaturized sensor, the dual-electrode configuration is expected to have less fixed capacitance, without a reduction in sensitivity and an additional guard electrode.

5.2.4 Sensor capacitance

The circular CPDMS membrane (functional element) and the dual-electrode configuration can offer better performance for the miniaturized sensor. Hence, in order to develop an analytical model of sensor capacitance (C_S), a sensor with a circular CPDMS membrane and a dual-electrode configuration is considered. T and the CPDMS membrane form a parallel plate capacitor, as shown in Fig. 5.4. When the membrane is in the null position, the capacitance between T and the CPDMS membrane is:

$$C_{TP} = \epsilon_0 \frac{A}{d_0} \tag{5.15}$$

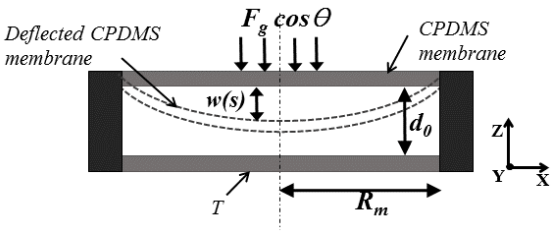

Figure 5.4: Cross-sectional view of the sensor, showing CPDMS membrane deflection

where ϵ_0 is the permittivity of free space, A is the surface area of the CPDMS membrane and d_0 is the distance between T and the CPDMS membrane.

The tilt along X-axis deflects the membrane in the Z and Y directions. As the deflection in the Y (also X) direction is restricted and the CPDMS membrane moves parallel to T, capacitance change due to membrane deflection along the sensor's parallel axes (X and Y) is small and negligible. The sensor is only sensitive to the deflection of a membrane perpendicular to the sensor structure (Z-axis). Membrane deflection along the Z-axis varies the distance between T and the CPDMS membrane, as shown in Fig. 5.4, and changes capacitance. The capacitance between T and the CPDMS membrane can be calculated as:

$$C_{TP} \pm \Delta C_{TP} = \epsilon_0 \iint \frac{dS}{d_0 - w(S)} \tag{5.16}$$

where C_{TP} is capacitance between T and the CPDMS membrane when the membrane is in the null position, ΔC_{TP} is the change in C_{TP} due to membrane deflection and $w(S)$ is deflection of the CPDMS membrane surface S along the Z-axis. In case of a circular structural element, Equation (5.4) can be substituted for $w(S)$, in which case Equation (5.16) will be modified to:

$$C_{TP} \pm \Delta C_{TP} = 2\pi\epsilon_0 \int_0^{R_m} \frac{rdr}{d_0 - w_{co}(1 - \frac{r^2}{R_m^2})^2} = \begin{cases} \dfrac{\pi\epsilon_0 R_m^2 arctanh\sqrt{\frac{w_{co}}{d_0}}}{\sqrt{w_{c0}d_0}}, & \text{if } w_{c0} \geqslant 0. \\ \dfrac{\pi\epsilon_0 R_m^2 arctan\sqrt{\frac{w_{co}}{d_0}}}{\sqrt{w_{c0}d_0}}, & \text{otherwise.} \end{cases} \tag{5.17}$$

From Equation (5.14), the C_S of a dual-electrode sensor can be expressed as:

$$C_S = \begin{cases} C_{TR} + \dfrac{\pi\epsilon_0 R_m^2 arctanh\sqrt{\frac{w_{co}}{d_0}}}{\sqrt{w_{c0}d_0}}, & \text{if } w_{c0} \geqslant 0. \\ C_{TR} + \dfrac{\pi\epsilon_0 R_m^2 arctan\sqrt{\frac{w_{co}}{d_0}}}{\sqrt{w_{c0}d_0}}, & \text{otherwise.} \end{cases} \tag{5.18}$$

5.3 Simulation Studies

Various aspects of the miniaturized capacitive sensor design were verified using the FEA software package COMSOL Multiphysics. Sensor dimensions are given in Fig. 5.5. Selected materials, domain and boundary conditions are illustrated in Table 5.1. As the material CPDMS is not available in the COMSOL library, PDMS was selected and the electrical (conductivity) and mechanical (Young's modulus) properties were suitably modified.

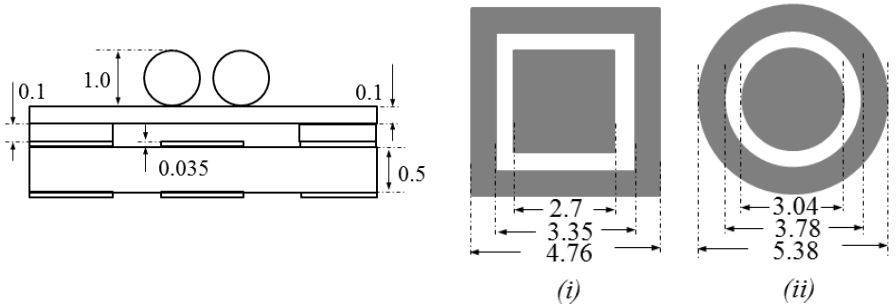

Figure 5.5: (a)Sensor dimensions (Cross-sectional view). (b)Electrode dimensions (top view): (i)Square electrode. (ii)Circular electrode; all dimensions in mm

Table 5.1: FEA Simulation Details

Description	**Material**	**Domain**	**Boundary**
Active Element	CPDMS	Linear Elastic Dielectric, Gravity	
Distance Holder	CPDMS	Linear Elastic Dielectric, Gravity	Fixed Constraint
Electrodes $(T, R, G, G_r\ )$	Copper		Terminal
Conductive Balls	Steel AISI 4340	Linear Elastic Dielectric, Gravity	Floating Potential
Dielectric Layer	FR4	Linear Elastic Dielectric	Fixed Constraint

5.3.1 Functional Element Deflection Analysis

Three-dimensional structures of the proposed sensors with square and circular functional elements were simulated in COMSOL Multiphysics. The sensor with the square functional element had a square-shaped electrode structure, and the one with the circular functional element used circular-shaped electrodes. Both electrode structures and their dimensions are given in Fig. 5.5(b). All corresponding areas for both sensors (square and circular) were kept equal; for instance, the surface area of the square and circular functional elements were kept the same, and the surface area of the square and circular electrodes were kept the same. In the analytical model, it was assumed that the mass is equally distributed over the membrane. Hence, the boundary conditions were set such that the mass on the functional element is equally distributed. The gravity load was applied to the functional element and tilt was simulated by varying the gravity components. A tilt from -180^o to +180^o was simulated. The simulated deflections of the

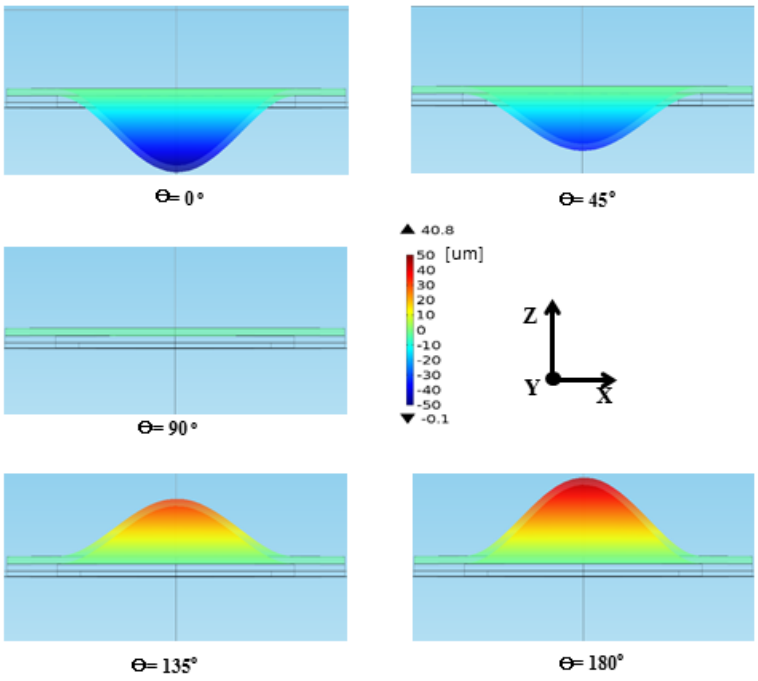

Figure 5.6: Simulation of deflection of circular functional element along the Z-axis, at different tilt angles. For better visualization, deflections are magnified 20 times.

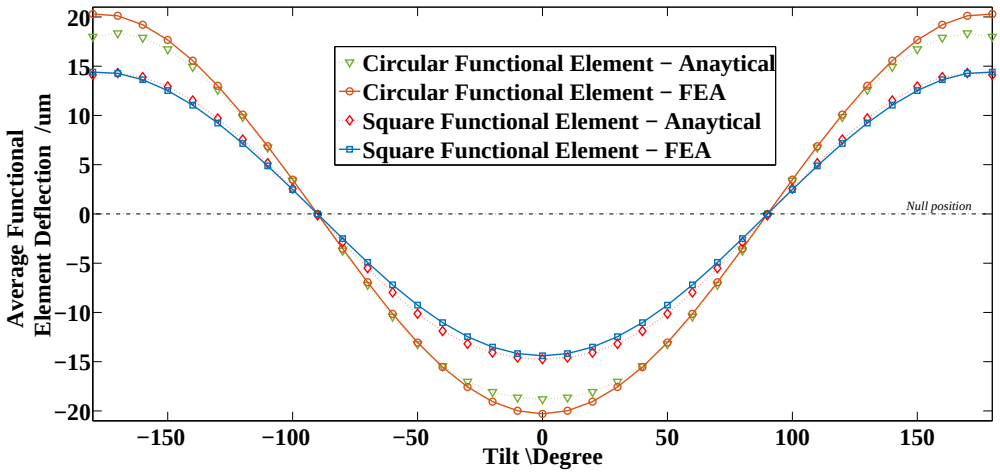

Figure 5.7: Average deflection of the square and circular functional elements along the sensitive axis at various tilt angles.

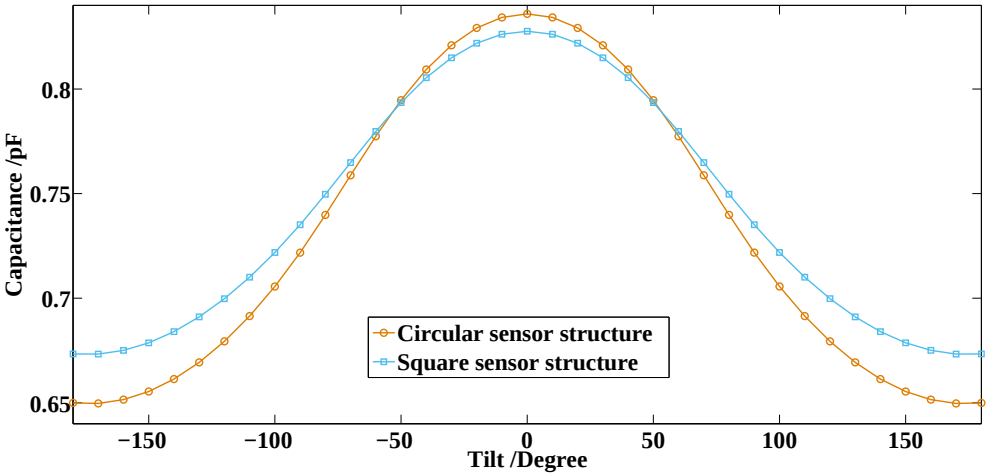

Figure 5.8: Capacitances recorded from the square and circular sensor structures at various tilt angles

circular functional element for various tilt angles along the Z-axis are shown in Fig. 5.6. The average deflections of the functional elements are given in Fig. 5.7. The change of the sensor capacitance, due to the deflection of the functional element, is shown in Fig. 5.8. At $\pm 90^o$, the CPDMS membrane's (functional element) deflection is 0 μm. With an increase of tilt, the average deflection along the positive Z-axis increases. The distance between T and the CPDMS membrane also increases, which in turn decreases sensor capacitance. Similarly, a tilt angle lower than 90^o results in an increase of the average deflection of the CPDMS membrane along the negative Z-axis. That is, the CPDMS membrane moves closer to T, which increases the sensor capacitance. The deflection of the CPDMS membranes perpendicular to the sensitive axis ($\pm$X axis and $\pm$Y axis) and variations of capacitances due to these deflections were also simulated, but, as expected, these deflections were negligible. The functional element deflection calculated from the analytical model discussed in Section 5.2.2 is also plotted in Fig. 5.7. The FEA results are comparable with the analytical model. The average deflection of the circular functional element (FEA and analytical) is 1.4 times higher than the square functional element. Hence, the sensor with the circular structure showed a 1.2 times better sensitivity than the sensor with a square structure.

5.3.2 Single and Dual-Electrode Sensor Capacitance

This section verifies the effectiveness of both the single and the dual-electrode configurations on sensing deflections of the functional element. Here, the sensor with the circular functional element was considered. T was set to 1 V, R to 0 V and G was grounded. In the single-electrode configuration, G_r was at 1 V, while for the dual-electrode G_r was grounded. The sensor with both electrode configurations was simulated for tilt. At

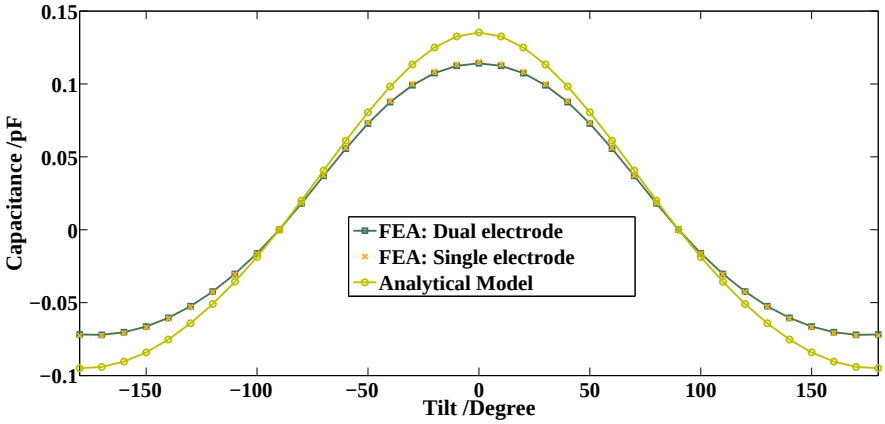

Figure 5.9: Variable capacitance(ΔC_{TP}) recorded from single- and dual-electrode sensors. The variable capacitance value obtained from the analytical model is also plotted

$+90^o$, the dual- and the single-electrode sensor showed capacitance (C_S) of 0.834 pF and 1.115 pF, respectively. At $+90^o$, the membrane was in the null position and the variable capacitance component ΔC_{TP} (in equation (5.13) and (5.14)) were zero. C_S at $\pm 90^o$ is the fixed (offset) capacitance of the sensor structure. As discussed above, for a sensor with a single-electrode configuration, the offset capacitance was $C_{TR} + C_{ST} + C_{TP}$, whereas for the sensor with the dual-electrode the offset capacitance was $C_{TR} + C_{TP}$. The higher capacitance observed for the single-electrode sensor at $+90^o$ was the result of additional C_{ST}. The variable capacitance (ΔC_{TP}), i.e. sensor capacitance after canceling offset capacitance, of both the single- and the dual-electrode sensor is plotted in Fig. 5.9. The variable capacitance ΔC_{TP} is equal in both cases. ΔC_{TP} calculated from the analytical model developed in Section 5.2.4 is also plotted in Fig. 5.9. The results of the analytical and the FEA models are similar. Any slight variation is because, the effect of R_p and deflecting the functional element in directions perpendicular to the sensitive axis are neglected in analytical model. This study shows that the dual-electrode sensor has less offset capacitance while maintaining the same sensitivity, without an additional guard electrode, compared to the single-electrode sensor. Hence, the dual-electrode configuration is considered the better choice for the proposed miniaturized capacitive sensor.

5.3.3 Sensor Uniqueness

In the simulations discussed above, the mass of the functional element was equally distributed. In this study, to introduce unique characteristics, four conductive balls were randomly distributed on the circular functional element. These balls distribute the functional element mass in a random and unique manner. Six sensor models SM_1 to SM_6, with different conductive ball arrangements, were simulated. Their ball arrangements are illustrated in Fig. 5.10. The simulated values of dual-electrode capacitance from

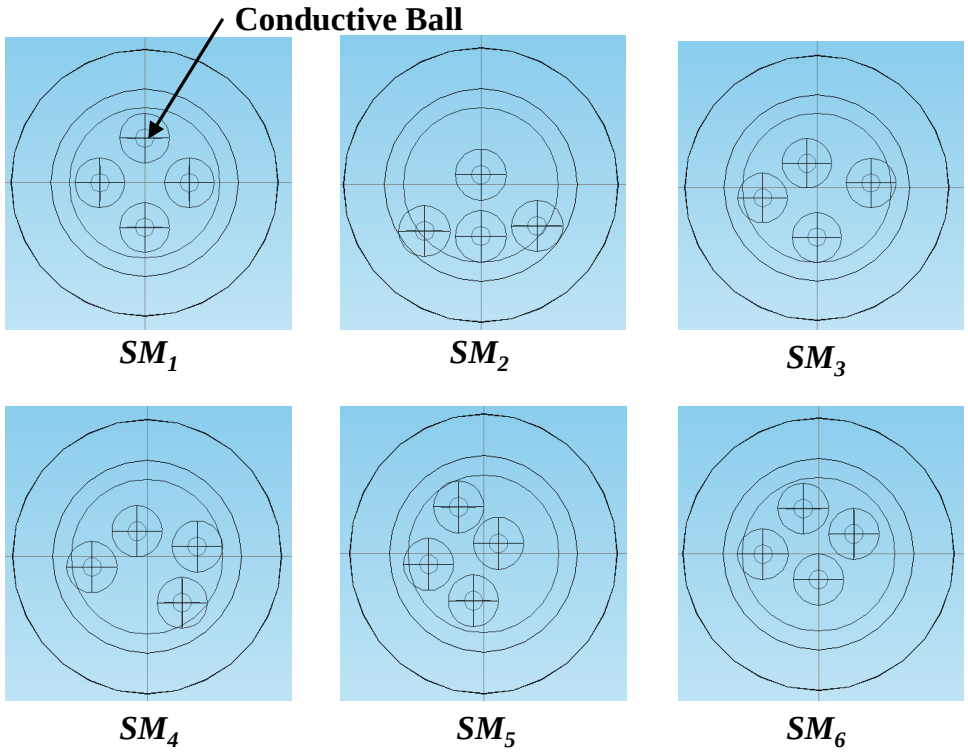

Figure 5.10: Ball arrangements in six sensor models (SMs).

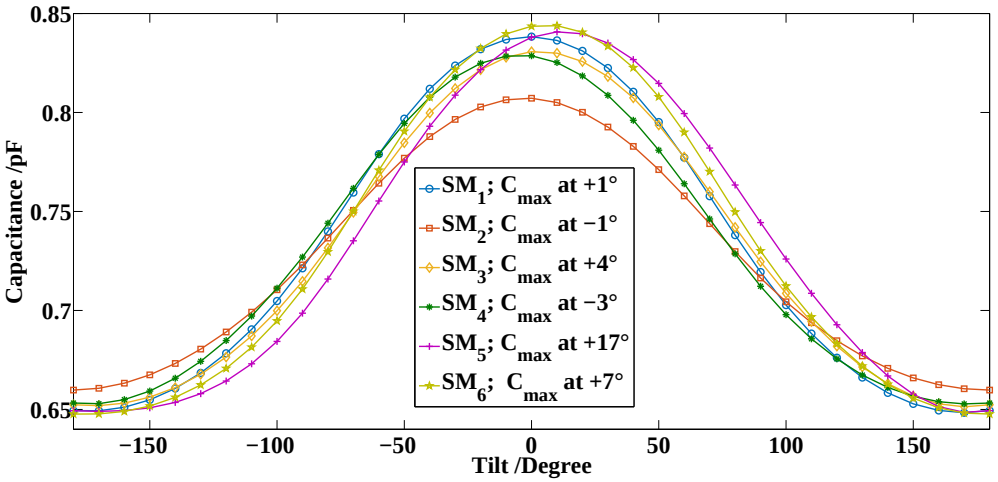

Figure 5.11: Capacitances recorded from $SM_1 - SM_6$ at various tilt angles

SM_1 to SM_6 for various tilt angles is plotted in Fig. 5.11. Owing to the different mass distributions, the deflection characteristic of each functional element is different, and so the different models showed unique output characteristics.

When the mass on the functional element was equally distributed, the maximum deflection of the functional element was 0^o and $\pm 180^o$ (in Fig. 5.9). The sensor showed maximum and minimum capacitance at 0^o and $\pm 180^o$, respectively. In $SM_1 - SM_6$, the random arrangement of the balls modified the weight distribution of the functional element. Therefore, the angle at which the sensor showed maximum (and minimum) capacitance varied, which actually improves the uniqueness of the sensor. The tilt at which each SM showed maximum capacitance was evaluated (using a curve fitting technique) and is shown in Fig. 5.11. The simulation results show that the random distribution of conductive balls alone can introduce high uniqueness in sensor characteristics.

5.4 Sensor Fabrication

A simple and cost-effective fabrication process designed for the miniaturized capacitive sensor is shown in Fig. 5.12. It does not require clean rooms or expensive equipment, and the fabrication process is similar to that employed for the dual-electrode sensor discussed in Chapter 2 (Section 2.5). The miniaturized capacitive sensor uses the CPDMS structure with conductive balls as the functional element. The CPDMS structure was fabricated using CPDMS membranes. The CPDMS composite for the membrane fabrication was prepared by mixing PDMS with carbon black (CB) particles. A solvent was used to improve the dispersion of CB in PDMS. The CB-PDMS composite was deposited into a master mold and then cured to form CPDMS membranes, which were then rolled out using a peeling initiator-roller arrangement. The detailed fabrication process and characterization of CPDMS membranes are discussed in the previous chapter. Each sensor required two CPDMS membranes—one as the active element and the other one as the distance holder. In the active element four conductive balls were randomly distributed. Prior to distribution, the balls were dipped in PDMS, which acted as an adhesive to attach the balls to the CPDMS membrane. A mask was used to limit the ball distribution region within the active area of the functional element. A circular hole was punched through the distance holder, using a mechanical puncher. During punching, the CPDMS membrane was sandwiched between two protective layers (as in Fig. 5.12). Thick layers of PDMS were used as protective layers to prevent breakage, contamination and stretching of the CPDMS membrane, as stretching beyond a certain limit can destroy electromechanical properties of the CPDMS membrane. The sensor substrate was fabricated on a two-sided printed circuit board (PCB). Electrode structures were first printed on glossy paper and then transferred to the PCB, using a laminating machine. The PCB was etched to form the electrode structure. The active element, the distance holder and the sensor substrate layer, were aligned manually and bonded together, using a CPDMS composite, to form the sensor structure.

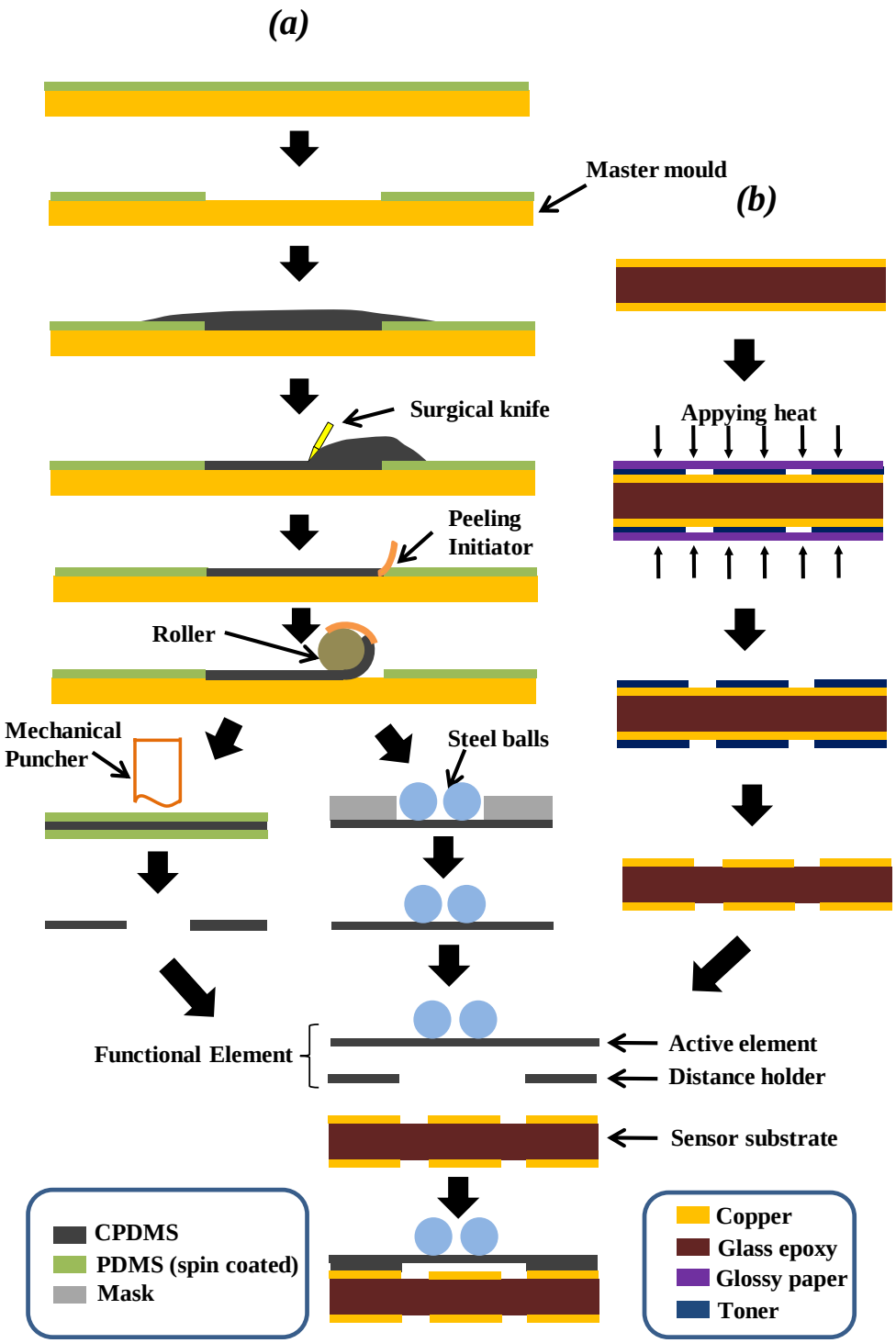

Figure 5.12: Illustration of how a miniaturized capacitive sensor is fabricated. (a)Functional element fabrication. (b) Substrate fabrication

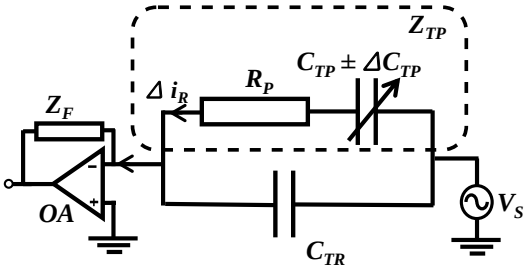

Figure 5.13: Electrical equivalent model of the miniaturized capacitive sensor

5.5 Optimum CB Concentration in CPDMS Structure

The electromechanical properties (resistivity and Young's modulus) of CPDMS structure varies with CB concentration. In order to find the optimum CB concentration for the miniaturized capacitive sensor, the effects of these parameters are analyzed using the electrical equivalent model of the miniaturized sensor. As discussed in Section 5.2.3, a miniaturized capacitive sensor is a parallel combination of the fixed capacitance C_{TR} and the variable capacitance $C_{TP} \pm \Delta C_{TP}$, along with series R_P (resistance of the CPDMS membrane). The electrical equivalent diagram is shown in Fig 5.13. $C_{TP} \pm \Delta C_{TP}$ with R_P formed the variable impedance component Z_{TP} of the sensor output, which can be expressed as:

$$Z_{TP} = \frac{1}{j\omega(C_{TP} \pm \Delta C_{TP})} + R_P \tag{5.19}$$

where ω is the angular frequency of V_S. The dual-electrode measurement set-up measured the Z_{TP} by measuring current Δi_R, which in turn was proportional to $\mid Z_{TP} \mid$ ($\Delta i_R = V_S / \mid Z_{TP} \mid$):

$$\mid Z_{TP} \mid = \sqrt{\frac{1}{(\omega(C_{TP} \pm \Delta C_{TP}))^2} + (R_P)^2} \tag{5.20}$$

From Chapter 4, the increase of CB concentration reduced R_P. From Equation (5.20), this reduced $\mid Z_{TP} \mid$ and in turn increased Δi_R. However, an increase of CB concentration also increased the Young's modulus of the membrane. From Equation (5.8), an increase of the Young's modulus reduced the deflection sensitivity of the membrane and in turn limited the variation in $C_{TP} \pm \Delta C_{TP}$ (equation (5.17)) in relation to tilt.

In order to find optimum CB concentration for the CPDMS membrane, $\mid Z_{TP} \mid$ was evaluated by substituting resistivity and Young's modulus values (evaluated in Chapter 4) at various tilt angles. The variation in $\mid Z_{TP} \mid$ evaluated for CB-Methanol-PDMS membranes, for CB concentrations at 3-wt%, 5-wt%, and 7-wt%, are given in Fig. 5.14. Maximum impedance variation was obtained at a CB concentration of 5-wt% (percolation threshold). Below the percolation threshold, a high value of R_P limited $\mid Z_{TP} \mid$ variation. Once the membrane started conducting, as $\frac{1}{(\omega C_{TP})^2} >> (R_P)^2$, the effect

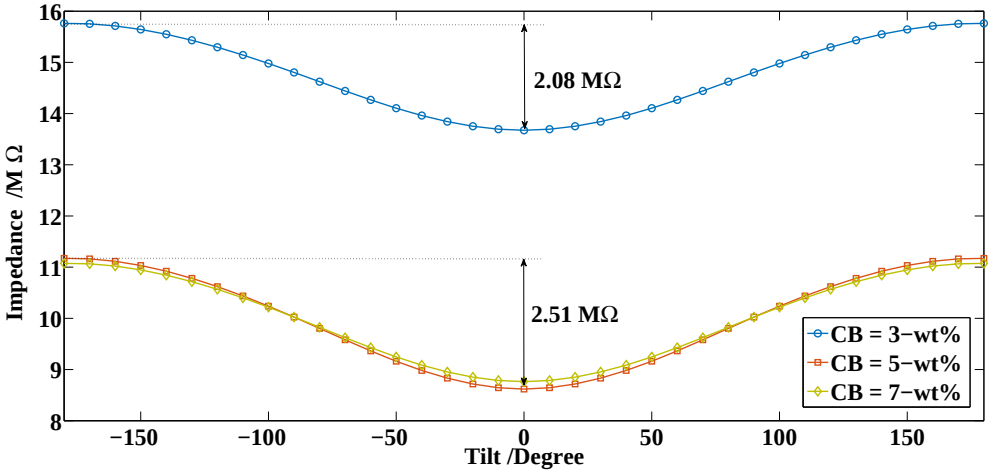

Figure 5.14: Variable impedance ($\mid Z_{TP} \mid$) of the miniaturized capacitive sensor for various tilt angles

of membrane resistivity was negligible. Under this condition, Z_P only depended on the Young's modulus of the CPDMS membrane. The Young's Modulus was minimal at the percolation threshold (5-wt% CB concentration), so, for the miniaturized capacitive sensor, CPDMS membranes at the percolation threshold were optimal.

Comparing CPDMS membranes, fabricated using CB-Methanol-PDMS and CB-Toluene-PDMS composites, for a miniaturized capacitive sensor, the CPDMS membrane fabricated using CB-Methanol-PDMS was better because of following reasons:

- It showed a slightly lower Young's modulus, so miniaturized capacitive sensor using CB-Methanol-PDMS membranes can offer better sensitivity.
- As sensor sensitivity is independent of a membrane's resistivity values, the low resistivity of CB-Toluene-PDMS membranes is not an advantage for miniaturized capacitive sensor.
- The surface profile of the membrane fabricated using CB-Methanol-PDMS was better.
- The membrane fabrication process is cost-effective and environmentally friendly, as discussed in Section 4.3.2.

5.6 Experimental Set-ups and Results

In order to validate practically the miniaturized sensor design, six circular sensor structures ($SM_1 - SM_2$), each having different ball arrangements, were fabricated. The tilt measurement set-up discussed in Chapter 2 was used for testing SMs. Dual-electrode sensor capacitances were measured with an AD7746 evaluation board, and all the experiments were carried out at room temperature ($22^oC \pm 0.5^oC$).

5.6.1 Sensor Stability and Reliability

The stability of the sensor output was verified. SM_1, along with the measurement circuit, was attached to a tilt-able platform. Sensor output at 0^o tilt was recorded for about 14 minutes (10,000 sample points at a 77 ms rate). At 0^o the sensor showed average capacitance of 1.080 pF with a maximum variation (uncertainty) $\pm$ of 0.003 pF. Factors such as humidity and temperature variations, external electromagnetic interference and noise in the measurement system contributed to these variations. $\pm$ 0.003 pF was considered the tolerance for the sensor output. Then, an impulse tilt of $+90^o$ was applied and the output was recorded for another 14 minutes. Again, the sensor was tilted for another $+90^o$ and its output was recorded for another 14 minutes. Recorded capacitances at tilt angles 0^o, $+90^o$, and $+180^o$ are shown in Fig. 5.15. It has been observed that, after applying the tilt, sensor output takes a certain amount of time (called 'settling time') before settling down to a stable value. Here, settling time is considered as the time taken by the sensor output to reach and settle within the tolerance limit ($\pm$ 0.003 pF) of the saturation value, after applying the tilt. The settling time evaluated from the recorded output is also shown in the Fig. 5.15. At $+90^o$, the sensor output took 0.5 seconds to reach a stable value, while at $+180^o$, the output took 52 seconds to saturate. This difference in settling times might be due to the change in behavior of CPDMS membrane in different electric field strength. Further investigation need to be carried out in this direction. In all of the following experiments, to make sure that the sensor outputs reached the saturation value, output capacitances were recorded 52 seconds after tilting.

The reliability of the prototype sensor was also verified. SM_1 was tilted from -180^o to $+180^o$ and the output was recorded for every 10^o tilt. The experiment was repeated six times ($SM_{1A} - SM_{1F}$), with an hour in between each measurement series. The recorded sensor capacitances are plotted in Fig. 5.16. SM_1 showed high reliability. Any

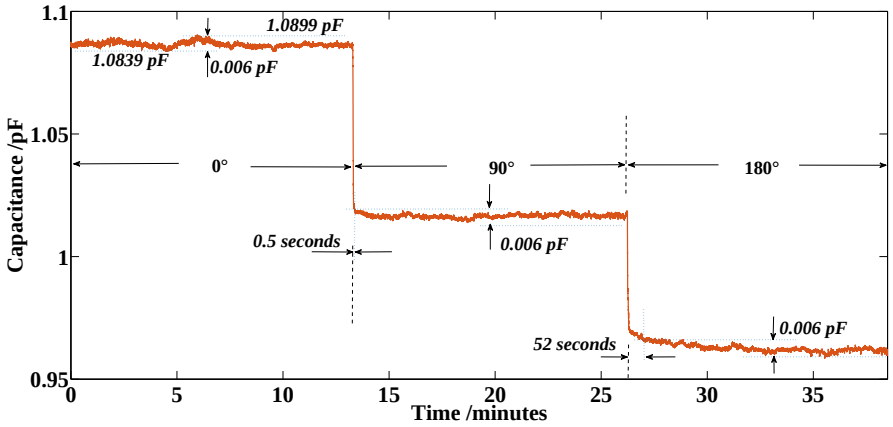

Figure 5.15: Sensor output was recorded to verify sensor stability at different tilt angles. The time required to stabilize sensor output after applying an impulse tilt was also evaluated

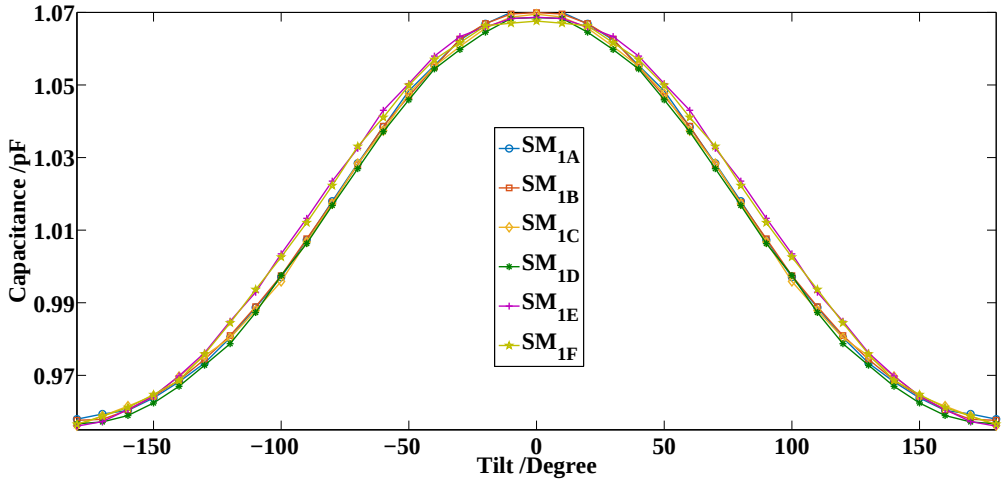

Figure 5.16: Sensor capacitance recorded when sensor SM_1 was tilted six times

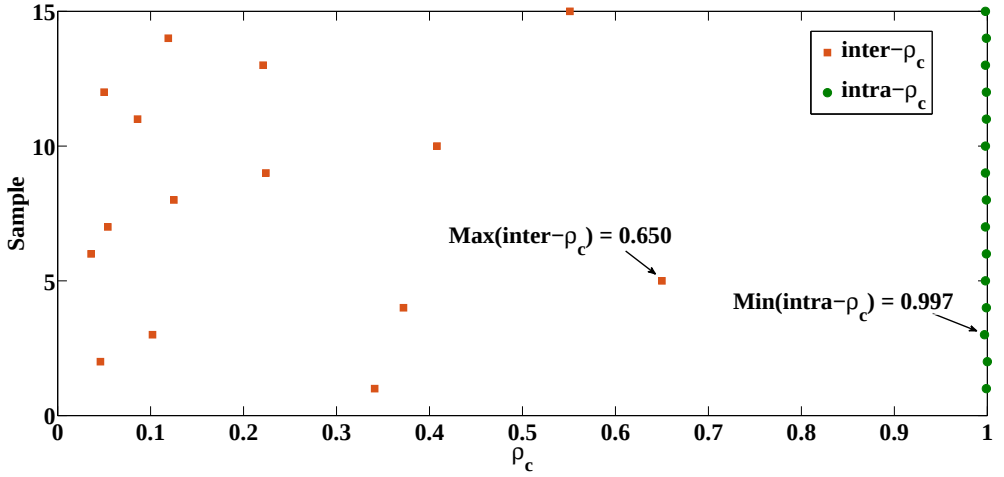

Figure 5.17: The uniqueness parameters $inter - \rho_c$ and the reliability parameter $intra - \rho_c$, evaluated from miniaturized capacitive sensor

slight variations in capacitances are due to tolerances of the sensor output and parallax error [1] in the measurement system. The reliability parameter intra-ρ_c was evaluated in relation to the six sensor outputs. The values are plotted in Fig. 5.17. SM_1 exhibited a worst-case reliability ($Min(intra - \rho_c)$) of 0.9970.

5.6.2 Sensor Uniqueness

Six SMs ($SM_1 - SM_6$) with different conductive ball arrangements were tested for tilt. The outputs recorded from the SMs are plotted in Fig. 5.18. Each SM showed unique

[1] A parallax error is the perceived shift in an object's position as it is viewed from different angles [112].

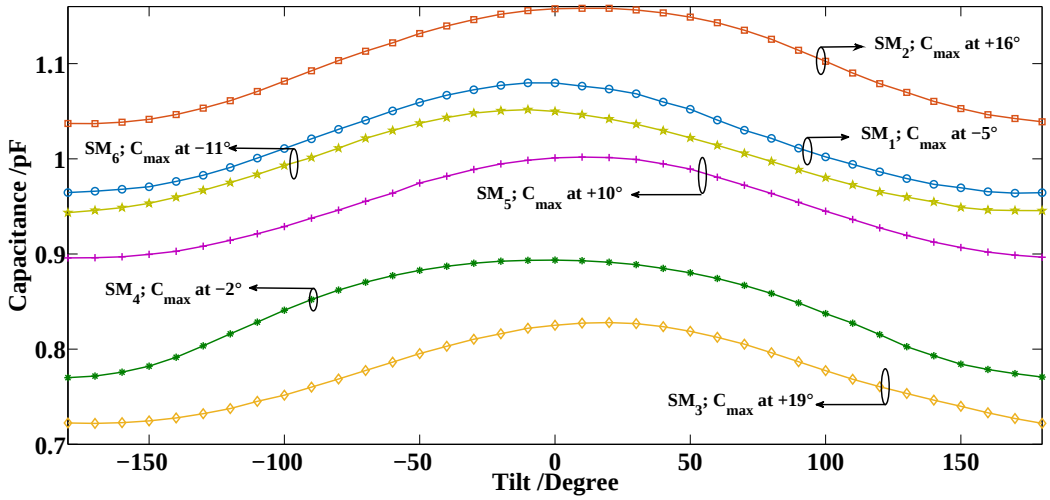

Figure 5.18: Sensor capacitances recorded from SM_1 to SM_6 at different tilt angles

output characteristics. Sensor parameters (discussed in Section 2.6) were evaluated and are given in Table 5.2. Dual-electrode sensor parameters are also in the same table for comparison. The SMs showed an average C_{OS} of 0.9505 pF with a C_{OS} spread of 0.3273 pF. The sensitivity parameter, ΔC_{max}, is 0.1232 pF. Sensitivity is high, considering that the active area of the sensor's functional element is 15 times smaller than that of the dual-electrode sensor. The uniqueness parameter $inter - \rho_c$ was also evaluated, and plotted in Fig. 5.17. The sensor shows a very high level of uniqueness, with the worst case in this regard being $Max(Inter - \rho_c)$ at 0.6500. These values are much better than for the dual-electrode sensors. The factors that contributed to the high uniqueness of the miniaturized sensor are given below.

- The sensor has a thin active element (100 μm), and the mass contribution of the balls is much higher than the CPDMS membrane. In addition, the random distribution of the balls uniquely modified the CPDMS membrane's deflection characteristics, resulting in unique output characteristics. The tilt at which average

Table 5.2: Sensor Parameters

Parameters	**dual-electrode Sensor**	**Miniaturized Sensor**
Active Surface area(mm^2)	169	11.22
C_{OS} (pF)	0.9065	0.9505
ΔC_{max} (pF)	0.2895	0.1232
C_{OS} Spread (pF)	0.0999	0.3273
$Max(Inter - \rho_c)$	0.9850	0.6500
$Min(Intra - \rho_c)$	1.000	0.9970

membrane deflection is at a maximum also varies in line with ball distribution. Hence, unlike the dual-electrode sensor, each sensor showed maximum (also minimum) capacitance at different tilt angles, which further improves the uniqueness of the sensor. The tilt at which each SM showed maximum capacitance is shown in Fig. 5.18.

- The sensor consists of a CPDMS membrane as the active functional element. Tolerances during CPDMS membrane fabrication alter the electromechanical characteristics (Young's modulus) and thickness of the membranes, as discussed in the previous chapter. The thickness variation of the distance holder varied capacitance C_{TP} between T and the CPDMS membrane (in Fig. 5.3), whilst variations in the Young's modulus and the thickness of the active element affect the membrane's deflection characteristics. These random variations in the CPDMS membrane characteristics helped to achieve high uniqueness in the miniaturized sensor.

5.7 Advantages of Miniaturized Sensor Design

1. Small surface area: The active surface area of the miniaturized sensor is 15 times smaller than that of the dual-electrode sensor.

2. High uniqueness: The miniaturized sensor shows very high uniqueness compared to the dual-electrode sensor.

3. High Unclonability: Random variations in a sensor's structures, especially variations in the CPDMS membrane's characteristics, are difficult to measure, model and duplicate. Hence, cloning the sensor is impossible.

4. Sensitivity is not limited: In the dual-electrode sensor design, the C_{FG} dominant region limits sensitivity. In the miniaturized sensor, as the C_{FG} dominant region is not present, sensor sensitivity can be improved by decreasing distance holder thickness and increasing the mass of the functional element. Therefore, sensor dimensions including size of the balls can be reduced further, without affecting sensitivity.

5.8 Limitations of the Miniaturized Sensor Design

1. High offset capacitance: The miniaturized sensor has a very high fixed offset capacitance. However, the differential measurement technique discussed in Chapter 3 can be considered for the miniaturized sensor, to cancel out any offset capacitance.

2. High settling time: The miniaturized sensor has a high settling time, which limits its dynamic performance. Further investigations need to be carried out in this direction.

5.9 Conclusion

Design of a miniaturized capacitive sensor with unique and unclonable characteristic has been presented. The sensor consists of a CPDMS structure with randomly distributed conductive balls as the functional element which, connected to the receiver electrode (R), forms a parallel plate capacitor with the transmitter electrode (T) below it. A measurand, such as tilt, deflects the functional element, which in turn alters the distance between T and the functional element and changes sensor capacitance. As a result of the random distribution of the balls and random variations in CPDMS membranes, each sensor shows unique characteristics that cannot be duplicated. The whole active area of the functional element takes part actively in sensing, which helps achieve high sensitivity and uniqueness with a reduced surface area. The proposed design also offers the possibility of further reducing sensor size, without affecting sensitivity or uniqueness, so the miniaturized sensor is suitable for space-limited applications such as portable devices and smart cards.

6 Prospective Applications of Sensors with Unique and Unclonable Characteristic

6.1 Introduction

As discussed in Chapter 1, the main motivation behind the development of sensors with unique and unclonable characteristic is that they can be used:

- As hardware identifiers, similar to a PUF.
- As sensors with an integrated identifier.
- As sensor elements with unique and random characteristics for developing nature-like sensor arrays.

The specific applications of capacitance-based unique and unclonable sensors are discussed in the following sections.

6.2 Sensor with Unique and Unclonable Characteristic as an Identifier in Smart Cards

As already discussed in Chapter 1 (section 1.4.1), the traditional way to store secret identification codes/keys in memory, inside resource-limited devices such as smart cards, is vulnerable to different types of attack. Once the information is known, these cards can be easily duplicated, and even the most advanced 'chip-and-pin' cards, which have microcomputer and cryptographic algorithms, can be cloned [113] [114]. Researchers are therefore considering hardware-based identifiers such as PUFs, to enhance the security of smart cards.

Smart cards using an optical PUF as an identifier are currently available [115] [116]. The optical PUF integrated into the smart card is challenged with laser beams, to which the PUF generates a unique response. The verifier uses the unique response to identify the smart card. Such PUF-based smart cards are difficult to clone, and they thus provide better security than memory-based techniques. The main drawback of an optical PUF, though, is that it requires a complex and optical laser system for applying the challenge. Furthermore, the area of the smart card casing above the PUF sensor needs to be transparent. Even small scratches in the transparent region can affect sensor responses and the transparent region also limits the aesthetics of the card (such as print design, company logo, etc.).

The sensor with unique and unclonable characteristic proposed herein can be used as a hardware identifier in smart cards for applications such as payments, access control, and electronic passports. Compared to other PUFs, sensors with unique and unclonable characteristic have the following advantages.

- The challenge to the sensor can be applied by a simple tilting set-up.
- The source of uniqueness is both electrical and mechanical, so the sensor is difficult to model and duplicate.
- The sensor can be integrated fully within the card structure.
- It does not require any electrical contact for applying the challenge. It is also possible to read the response using a non-contact method (discussed in Section 6.2.1).

These features make the proposed unique and unclonable sensor a better hardware identifier for smart card application than optical PUFs. The large thicknesses of the proposed sensor structures (900 μm) limits its use in application such as such as payment cards (credit card), which has a thickness of only 760 μm [117]. For such application, the thickness of the sensor structure can be reduced by replacing the balls with smaller balls of higher density, or by using a greater number of smaller balls.

6.2.1 Sensor Implementations in Smart Cards

The three possible unique and unclonable sensor implementations in smart cards are shown in Fig. 6.1. In the first implementation (shown in Fig. 6.1(a)), the sensor structure (both the functional element and the electrode structure) is inside the smart card. The verifier sends a random tilt (or a set of tilts) as a challenge to the smart card. The smart card, along with the sensor, tilts and the sensor generates a unique capacitance output. The verifier reads this capacitance and compares it with values enrolled in its memory for authentication. The second implementation is shown in Fig. 6.1(b). Here, only the functional element is inside the smart card. For the tilt challenge, the functional element deflects. The capacitive electrode structure is in the verifier and it converts the membrane deflection into a change of the capacitance. The advantages of this implementation are that it is a non-constant response measurement and the sensor design in the smart card is simple. However, the significant distance between the electrode structure and the functional element limits sensor sensitivity and uniqueness. Furthermore, factors such as contamination of the card structure, scratches, etc. can affect the measurement. The third implementation (shown in Fig. 6.1(c)) is a combination of the first two implementations, whereby electrode structures inside both the smart card and the verifier measure the deflection of the membrane.

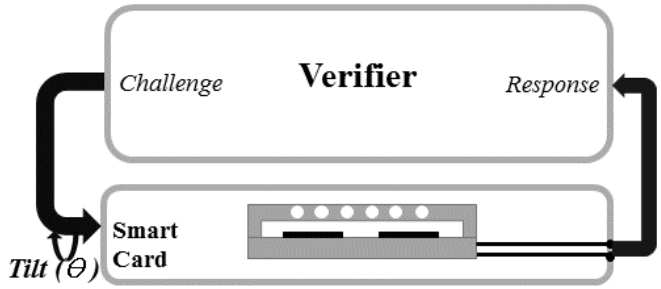

(a)

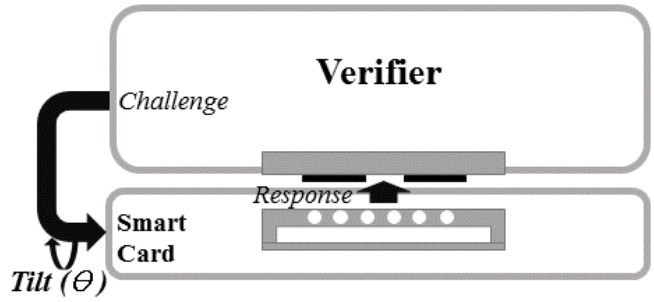

(b)

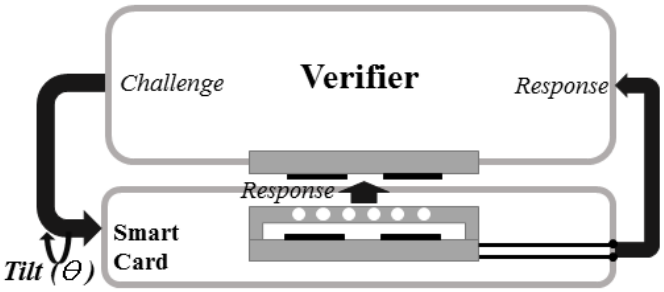

(c)

Figure 6.1: Possible unique and unclonable sensor implementations in smart cards (a) Both the functional element and the electrode structure inside a smart card. (b) The functional element is inside the smart card; the electrode structure in the verifier. (c) Functional element inside the smart card; electrode structures are in the smart card and the verifier

6.2.2 Authentication using Unique and Unclonable Sensor-based Smart Cards

Simple two-factor authentication, using a smart card with a unique and unclonable sensor, is now discussed. Generally, two-factor authentication is considered a strong technique for different applications such as payments, e-passports, etc., as it verifies 'something you have' (e.g. a smart card) along with 'something you know' (eg. a password or PIN) or 'something you are' (eg. facial image, fingerprint, or iris scan) [118] to identify and authenticate a person. The system and method for the proposed two-factor authentication are shown in Fig. 6.2. The system consists of a terminal into which the user inserts their smart card. In order to verify the user (something you know), the terminal prompts the user to enter a personal identification number (PIN) through the user interface. Alternatively, a fingerprint or iris scan (something you are) can be used for this purpose. In the meantime, the card interface reads the necessary user account information either stored inside the smart card or displayed on the card's surface and then sends it to the terminal controller, which in turn sends the PIN along with the user's account information to the server. The server controller then checks whether the PIN matches with the one enrolled for the account. In the case of a positive match, the user is authenticated. The next step is to verify the smart card (something you have). The random number generator (RNG) generates a number which represents the trajectory of the smart card rotation. This trajectory information is unpredictable and will be different for each transaction. The server controller sends this random trajectory information to the actuator via a terminal controller. The actuator then translates the

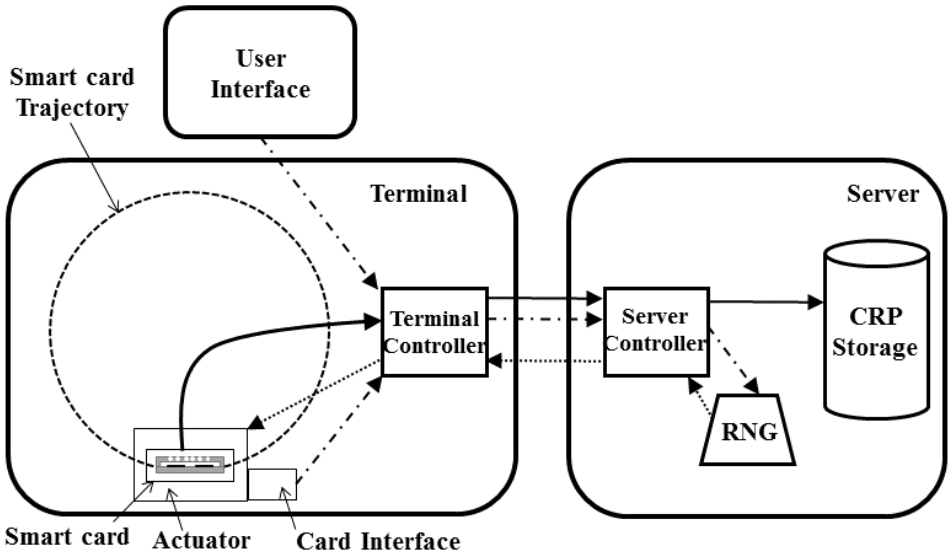

Figure 6.2: System and method for two-factor authentication using a smart card with a unique and unclonable sensor

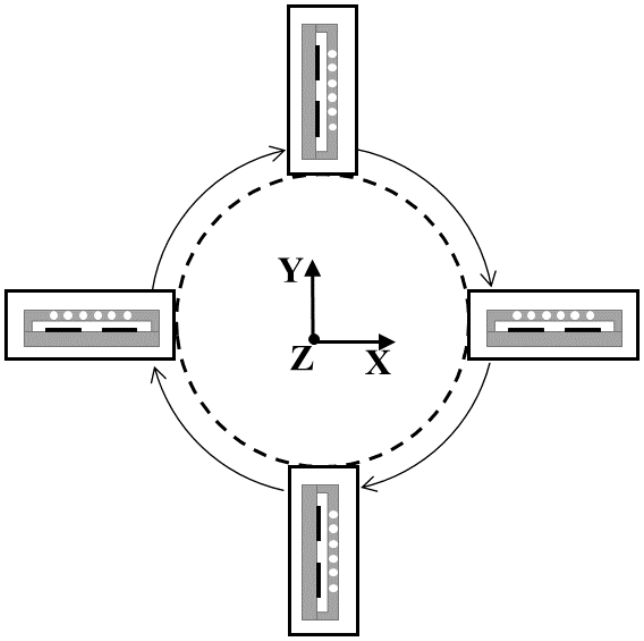

Figure 6.3: Diagram representing the rotation of a smart card in a circular trajectory along the Z-axis

trajectory information and tilts the smart card along the trajectory. Here, a circular trajectory is considered.

A detailed diagram showing the tilt of a smart card along a circular trajectory is shown in Fig. 6.3. Depending on the trajectory information, the actuator tilts the smart card along a specified angle and orientation. For instance, the first four digits of the trajectory information represent the four angles at which the card needs to be tilted along the Z-axis, and the next three digits represent the orientation of the sensor in the Y-axis. Alternatively, trajectory information represents small sections along the trajectory where the card needs to be rotated. At the specified angles or sections, the capacitance of the unique and unclonable sensor is recorded and sent to the server, which then compares the capacitance values with data enrolled in the challenge response pair (CPR) table. In the case of a positive match, further actions can be carried out. On the other hand, a mismatch, either during the PIN or the smart card verification phase, can result in card/user blocking. The two-factor authentication technique discussed here is a simple, lightweight authentication technique which does not require memory processing power, source, etc. inside the smart card. This is just one possibility, and the authentication process can be modified, depending on the application and security requirements. For example, for high-speed transactions, the PIN can be stored inside the card. In this case, offline PIN verification can be done without any server transaction, though the smart card would require its own in-built memory and processing capability. For low-security applications, PIN verification can be avoided altogether. Alternatively, instead

of a random trajectory, the card can always be rotated along a predefined trajectory (for example 0^o to 180^o), which would reduce the amount of server transactions and make the authentication process simpler and faster.

A unique and unclonable sensor can also be used alongside already existing smart card technologies such as chip and pin. These advanced smart cards have their own storage, processing power and application software and use cryptographic techniques for secure data communication. One application where a unique and unclonable sensor can be used in such a card is dynamic secret key generation for cryptography algorithms. When the user inserts the smart card, the terminal sends random or predefined tilt challenges to the smart card. Depending on the tilt angles, the sensor generates a unique capacitance output. The card controller stores the output temporarily in memory and the cryptographic module uses these data as a secret key (or generation of secret key) for encrypting sensitive information available in the smart card. The encrypted information is then sent to a server which can derive the key from the tilt angles and challenge response information stored in the server's database. Using this key, the server decrypts the encrypted information stored on the smart card. The memory is erased before removing the card from the terminal. In this method, as the key is dynamically generated, there is no need to store the key information permanently in memory, which protects the smart card from various types of memory-based attacks—something that is possible in available smart cards. Another application in which a unique and unclonable sensor can be used is offline PIN verification. In current smart cards, for offline PIN verification, the terminal sends the user-entered PIN to the smart card. The card compares this PIN with the PIN stored in its memory. In unique and unclonable sensor-based offline PIN verification, the terminal translates the PIN into a smart card tilt. The card controller then stores the sensor's capacitance at different tilt angles to temporary memory. This capacitance value is compared with a value previously enrolled in protected, non-volatile memory. In the case of a positive match, further action is carried out. The advantage of this method is that there is no need to send PIN information from a terminal to the smart card. PIN generation and comparison take place within the smart card's physical layer, which improves card safety.

6.3 Sensor as a Hardware Identifier in Tilt Gesture-based Keyless Systems

One of the main advantages of the sensor with unique and unclonable characteristic is that it can be challenged by a tilt force. Unlike optical or voltage challenge-based PUFs, the proposed sensor does not require any electronic circuits or complex optical systems to apply a challenge. Even a simple tilt hand gesture can be used to apply tilt—a feature utilized in tilt gesture-based keyless systems. Further details are discussed in this section.

Owners use keyless systems to gain access to modern-day vehicles and gain authorization to drive [119] [120]. These systems basically replace more traditional physical locks and keys. First-generation keyless systems (called 'remote keyless entry' (RKE))

used a hand-held electronic key (called a fob) for locking and unlocking a vehicle. The user carried the fob and needed to press a button, corresponding to a particular action. This triggered communication between the fob and the vehicle. The microcomputer in the fob encrypted a secret code (either a fixed or a rolling code) stored in the memory and sent it to the vehicle. The vehicle would then decrypt the information, verify the validity of the code, and perform the required action. The main disadvantage of the RKE system is that a user action (pushing a button) is required. Hence, the user always needs to search for the keys to lock or unlock the vehicle.

The passive keyless system has removed the interface between the user and the key (pushing a button), and made vehicle entry and driver authentication more convenient [121] [122]. The system automatically checks the proximity of an electronic identifier (EID) and performs the required action. Such systems generally employ a challenge-response technique to verify the EID's proximity. The vehicle sends a random number/challenge to the EID, either periodically or when the door handle is operated. If the EID is present in the proximity of the vehicle (say 2 m), it receives the challenge and encrypts the information using a secret key available in memory. The encrypted challenge is sent back to the vehicle as a response. In the meantime, the vehicle encrypts the challenge, using the secret key available in its database. The vehicle compares its response with the response from the EID. In the case of a positive match, the vehicle performs the necessary operation.

Passive keyless systems are highly vulnerable to relay attacks [123] in which the attacker bridges the large gap between the vehicle and the EID using two transceivers, as shown in Fig. 6.4. The attacker places transceiver A near the vehicle and transceiver B near the EID. When the attacker operates the vehicle door, the vehicle generates a challenge (C). Transceiver A modulates C and transmits it to transceiver B, which is placed near the EID. Transceiver B demodulates the signal and sends C to the EID, which then generates a response (R) and sends it back to transceiver B. Transceiver B then modulates R and sends it to transceiver A, which demodulates the signal and sends R to the vehicle. The vehicle performs the required action, expecting that the user holding the EID is in close proximity.

A gesture-based keyless system, which has the advantage of being both a passive and an active keyless system, is proposed. The idea is to integrate the unique and unclonable sensor with associated circuitry into a smart wrist watch/band and use the watch

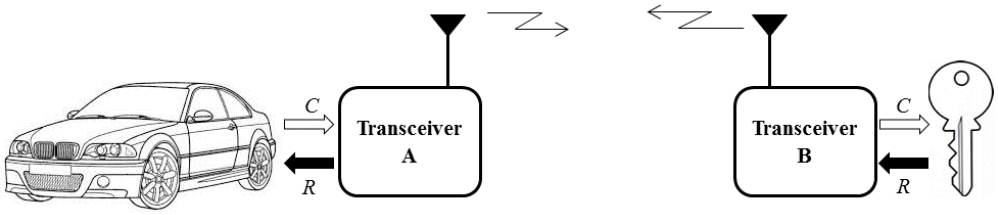

Figure 6.4: Relay attack in passive keyless systems.

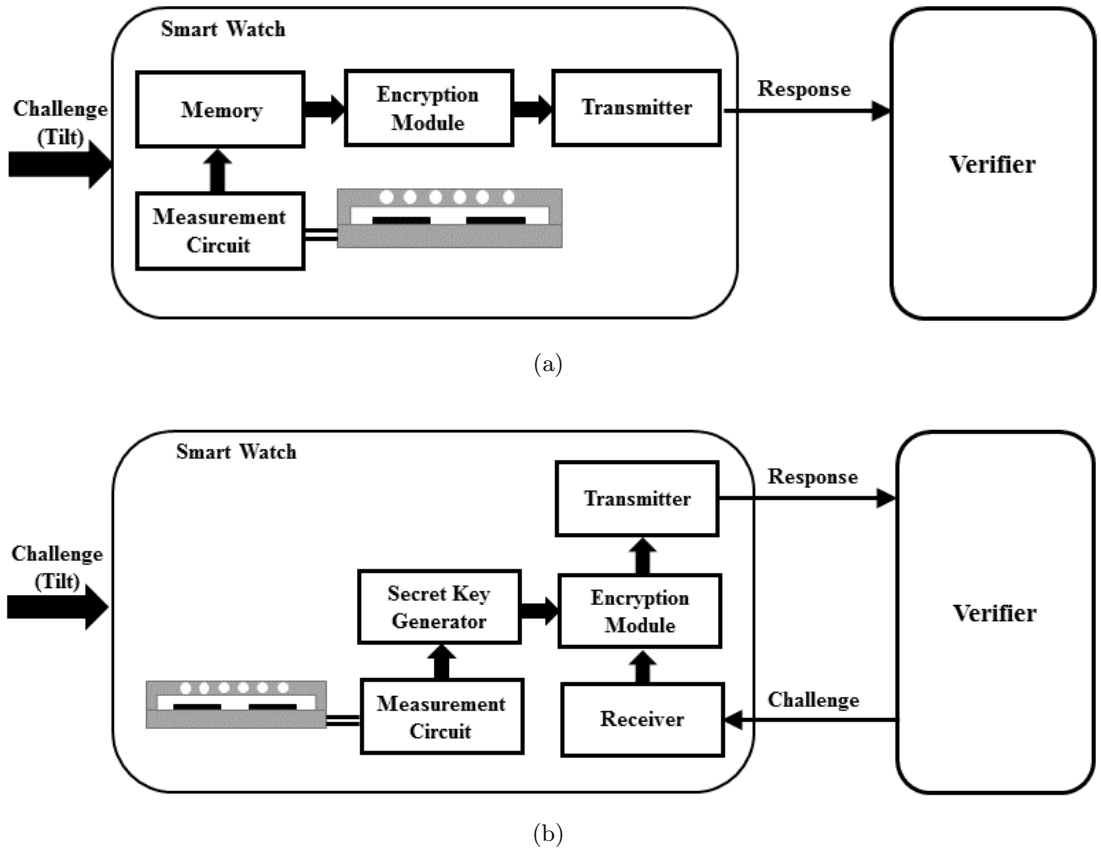

Figure 6.5: Block diagram of gesture-based keyless systems, using sensors with unique and unclonable characteristic. (a) The sensor generates a unique identifier. (b)The sensor generates a secret key for encryption

as an EID. Two types of EID implementation, using a unique and unclonable sensor, are discussed. The first implementation is shown in Fig. 6.5(a). The tilt gesture in a predefined pattern (challenge) generates a unique sensor output. The encryption module encrypts the output and transmits it to the verifier (e.g. a vehicle). Upon receiving the information, the verifier decrypts and compares it with the value stored in its database. The unique sensor output, associated with the particular tilt gesture, was previously enrolled in the verifier database, during the training phase. It is also possible to associate a particular gesture with a particular action. For instance, tilting in a clockwise direction corresponds to a door unlocking and tilting in an anticlockwise direction is for boot opening. For each pattern the sensor output is different. From this difference, the verifier can determine the required action. If the EID-transmitted information matches with what is in the memory, a required action is carried out. The second implementation, shown in Fig. 6.5(b), is similar to the challenge-response technique of the passive

keyless system. A tilt gesture in a predefined pattern activates the module and generates a unique sensor output. The key generator module then uses the sensor output to generate the secret key. Meanwhile, the receiver accepts the challenge randomly generated from the verifier. The encryption module encrypts the challenge, using the secret key generated from the sensor output. The encrypted challenge (response) is then sent back to the verifier. In the meantime, the verifier encrypts the challenge, using keys enrolled in its database. The verifier compares it with the response from the EID and checks its validity.

The proposed tilt gesture-based keyless system has many advantages. The EID in a watch gives the flexibility of using it as personal identifier for different applications, including access, control and authorization of a person in a vehicle, buildings, garage doors, etc. Unlike the RKE system, there is no need to search for keys inside a pocket or in a handbag, because, for most people, the watch is always on the wrist, and a wrist-tilt gesture can perform the required action. Wrist tilting is generally considered one of the easiest gestures [124], and it is possible (to some extent) even when both hands are occupied (e.g. with shopping bags). Furthermore, wrist tilting requires only limited space and can be performed without much physical or mental effort. Such a keyless system could also replace sensors such as hands-free boot opening sensors [125]. In the gesture-based keyless system, a user interface in the form of a tilt is necessary to activate the key and generate a valid response. Therefore, it is difficult to implement a relay-based attack. Moreover, the proposed system has all the advantages of PUF-based key/identifier generations such as high security, it is difficult to duplicate and it has minimum resource requirements.

6.4 Secure Rotation Sensing using Sensor with Unique and Unclonable Characteristic

Sensing systems in nature are tuned to the unique characteristics of their sensors. In such cases, it is impossible to replace the sensors without knowledge of the brain (the controller). This feature can be utilized in artificial domains for developing highly secure sensing systems. The design details of such a highly secure rotation measurement module, using the proposed sensor, are discussed in the following section.

Rotation sensors are widely used in many applications, such as automobiles, medical devices, defense, etc., for measuring numbers of rotations and angular speed, and indirectly measuring distance traveled [126] [127]. In many applications, the data collected from the rotation sensors are used to decide on further critical actions. For instance, ABS systems use a rotation sensor for speed measurement and utilize measurement data to decide on breaking torque. The authenticity of the measured data is critical in such applications. As already discussed in Chapter 1 (Section 1.4.1), the traditional way of implementing sensor security with a separate cryptography module along with a sensor is vulnerable to direct physical attack. Consider a (supposed) secure rotation measurement system, shown in Fig. 6.6. The system uses a magnetic rotation sensor which consists of a ferromagnetic toothed gear, rotating in front of a permanent

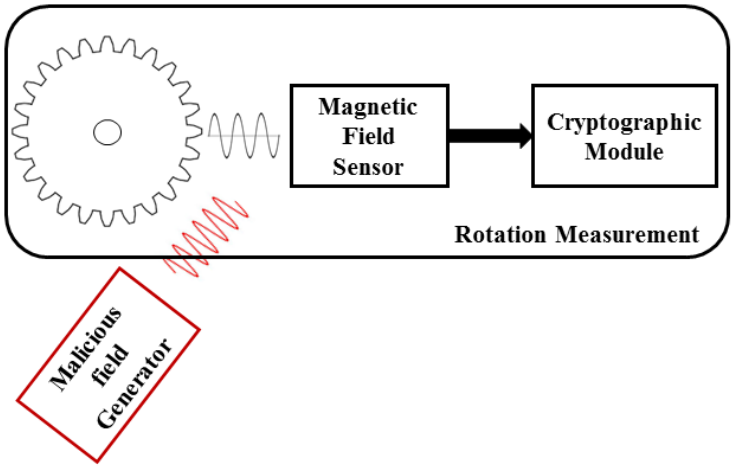

Figure 6.6: Block diagram of a rotation measurement system. A direct sensor attack is also shown (in red)

magnet. This gear rotation generates a time-varying magnetic flux. A magnetic field sensor (eg. pickup coil, hall effect sensor) converts the time-varying magnetic flux into a time-varying voltage signal. The frequency of the voltage signal is proportional to the speed of the toothed gear speed. The cryptographic module encrypts the measurement information and transmits it for further processing. This rotation measurement system is not secure against direct sensor attack, as an attacker may easily replace the magnetic sensor or parts of the magnetic sensor. Alternatively, one can insert a malicious signal. For instance, an attacker can shield the sensor's magnetic field and insert a malicious time-varying magnetic field (as shown in Fig. 6.6) [40]. In this measurement system, the cryptographic module cannot identify whether the measurement signal is coming from the authorized sensor, so the attacker can easily manipulate sensor output. If the measurement system is part of a network (e.g. IoT), the attacker can use it as a weak entry point and gain some control over the network.

A highly secure rotation measurement system using a unique and unclonable sensor is shown in Fig. 6.7(a). The rotation of the unique and unclonable sensor generates a periodic (near-sinusoidal) varying capacitance output, as shown in Fig. 6.7(b). The frequency of the output capacitance variation is proportional to the rotational speed of the sensor, and the number of cycles represents the number of rotations. The cycle characteristic of each sensor is unique. A capacitance measurement system converts the capacitance output into a periodic voltage signal with unique cycle characteristics. The cryptographic module uses this unique characteristic as an identifier to authenticate the sensor output. It is also possible to derive a secret key for the cryptography module from this unique cycle characteristic. In this system, the cryptographic module is tuned to the unique cycle characteristic of a particular sensor. If an attacker tries to replace the sensor or insert malicious signals, the cryptographic module can detect the attack from the cycle's characteristic. The proposed rotation measurement system is secure against

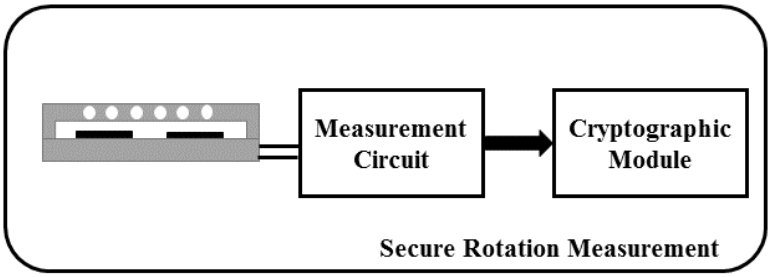

(a)

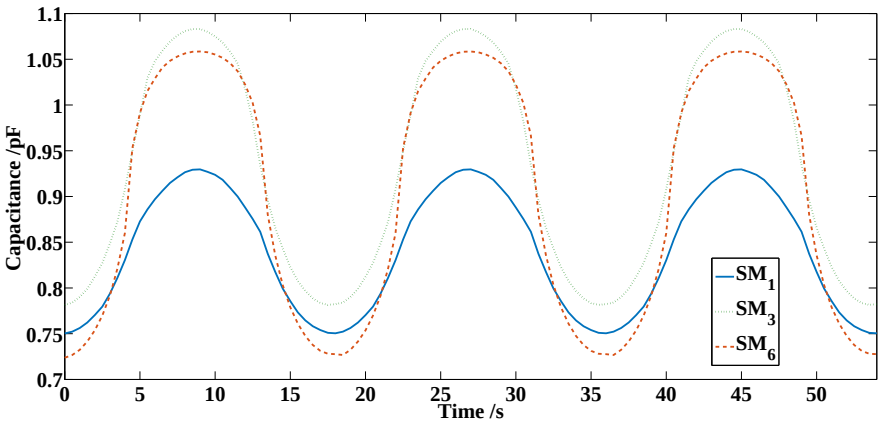

(b)

Figure 6.7: (a) Secure rotation measurement module a using unique and unclonable sensor. (b) Output is recorded when the capacitive sensor (discussed in Chapter 2) is rotated 3times.

direct sensor attack and it can be deployed for highly secure rotation measurement applications, even in remote and untrusted environments.

6.5 Nature-Inspired Lateral Lines, using Sensors with Unique and Unclonable Characteristic

Sensors in nature have unique and random (unclonable) characteristics. Nature's sensing systems exploit these unique-random characteristics to process and extract relevant information from a complex multivariate environment. These sensing systems are far superior (in terms of sensitivity, bandwidth, noise cancellation, etc.) than artificial systems that use highly precise sensors. The concept of extracting information using unique random sensors has yet to be explored in the artificial domain. Sensor systems employing sensors with random characteristics can be developed using the proposed unique

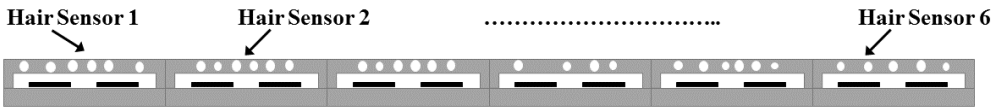

Figure 6.8: Nature-inspired lateral line, using sensors with unique characteristic

and unclonable sensor, which would provide the possibility of understanding more about nature's sensing systems and strategies.

The proposed unique and unclonable sensors can respond to mechanical parameter pressure, tilt and acceleration, and provide the corresponding capacitance output. These functionalities are similar to the hair sensor elements in lateral lines. Lateral lines (discussed in Section 1.3) are the hair sensor arrays used by certain fish and aquatic creatures for underwater localization, flow profiling, prey detection, etc. These lateral lines use the pressure gradients in hair sensors to detect nearby objects, acceleration gradients to determine flow velocity, and a tilt gradient to understand spatial orientation. An array of unique and unclonable sensors (shown in Fig.6.8) can function as an artificial lateral line. Unlike the artificial lateral lines reported to date [14]- [16], the unique and unclonable sensor-based lateral line is closer to nature because of the random characteristics of sensor elements, which are responsible for high sensitivity, large bandwidth and high noise cancellation in nature's sensor arrays, including lateral lines. Such characteristics of sensors in nature can be studied from unique and unclonable-based lateral lines.

6.6 Conclusion

Various applications of the sensors with unique and unclonable characteristic have been discussed. One possibility is to use it as a hardware identifier, similar to a PUF. Conventional PUFs use voltage or optical signals as a challenge, whereas the proposed sensors can be challenged by using tilt. For many applications, applying tilting is more convenient than applying a voltage or an optical signal. Different implementations of the sensors with unique and unclonable characteristics as a hardware identifier, for smart card applications and gesture-based keyless systems, are proposed herein. The proposed sensors can be also considered for developing secure sensing modules. The idea is to enrol the unique characteristics of the sensor in a verifier, which then authenticates sensor data from the unique sensor characteristics. Such a highly secure rotation measurement system, using a unique and unclonable sensor, is also proposed. Another application in which it may be considered is in developing a nature-like lateral line sensor. An array of sensor with unique and unclonable characteristics functions as a lateral line sensor. Due to the unique and random characteristics of the sensor elements, such lateral line sensors are closer to their natural counterparts. Developing such a nature-like sensor system would help to understand more about nature's way of sensing.

7 Conclusion

Sensors in nature are unique. The output characteristics of each one are slightly different from other sensors of the same type. Even within a sensor array, output characteristics differ. The unique output characteristics of nature's sensors are due to the random variations present in their structures. As the nature's sensing systems are tuned to the particular output characteristics, they can extract complex information.

Inspired by nature, sensors with unique and unclonable characteristic, has been developed. In general, they respond to a measurand and provide an output which is unique and different from other sensors. Random variations in the sensor's structure need to be the source of a unique output. The unique sensor's output due to such random structural variations is difficult to measure, model and duplicate. Hence, the unique output of the sensor is also unclonable.

The capacitive sensors proposed in this thesis respond to tilting and provide a unique and unclonable capacitance output. The sensor consists of a functional element and a capacitive electrode structure. The functional element deflects for tilt, and the capacitive electrode converts the deflection of the functional element into the capacitance. Random variations are integrated into the functional element. Owing to these random structural variations, the deflection characteristics of the functional element (mechanical uniqueness), as well as the way in which the functional element modifies the electrical field from the capacitive electrode (electrical uniqueness), is unique for each sensor, and thus the sensor capacitances at different tilt angles are unique for each sensor. As the source of output uniqueness is random variation, it is also impossible to develop sensors with the same capacitance characteristics.

Three different capacitance-based, unique and unclonable sensor designs have been proposed. The first sensor (referred as capacitive sensor) consists of a PDMS structure filled with randomly distributed conductive balls as the functional element. The arrangement of conductive balls in the functional element of each sensor is unique, which in turn introduces both electrical and mechanical uniqueness to the sensor's structure. Other random variations integrated during the sensor fabrication process improve uniqueness further. This sensor's structure shows maximum uniqueness and unclonability when the conductive balls fill 30% of the active functional element volume and when the functional element operates around an uncertain region (at the interface of C_{FR} dominant and C_{FG} dominant) 100 μm above the electrode structure. The differential capacitive sensor is an extension of the capacitive sensor. It also uses a PDMS structure filled with randomly distributed conductive balls as the functional element. The sensor has capacitive electrodes, above and below the functional element, arranged in a differential manner. Compared to the previous capacitive sensor structure, the differential capacitance sensor has a very low offset capacitance, high sensitivity, uniqueness and unclonability.

However, the surface areas of both dual and differential electrode sensors are large for various space-limited applications, and reducing the surface area degrades sensitivity and uniqueness.

The miniaturized capacitive sensor is designed for space-limited applications. It consists of a CPDMS structure with randomly distributed balls acting as the functional element. A planar electrode structure converts the functional element deflection into a unique and unclonable capacitance output. Compared to the other two sensor structures, the miniaturized sensor shows very high uniqueness at a reduced size. The factors that contribute to the high uniqueness of this miniaturized sensor are random ball distribution, random variations in the electromechanical properties of the CPDMS membrane, and random variations in CPDMS membrane thickness. The miniaturized sensor also exhibits high sensitivity. The thin, soft CPDMS membrane for the sensor's functional element is fabricated by mixing CB particles with PDMS. The electromechanical characteristics of the CPDMS membrane vary according to CB concentration. Membrane fabricated using different CB concentrations were characterized in this study to find the optimum CB concentration for unique and unclonable applications. The results show that a CPDMS membrane with a CB concentration of 5-wt% can provide maximum sensitivity to the unique and unclonable miniaturized sensor.

In the proposed sensors, minor random variations such as ball distribution, fabrication tolerances, etc., introduced high uniqueness in sensor characteristics. This uniqueness can be further improved by intentionally varying factors such as the number of conductive balls, ball sizes and CB concentrations. All the sensors also showed high reliability.

The proposed sensors with unique and unclonable characteristic can be used as a hardware identifier for applications such as smart card, keyless systems, etc., as a rotational sensor integrated with an identifier and also as a nature-like hair sensor with random characteristics.

Patent/Publications List

This list collects the author's publications and patent on the topics of this thesis.

- C. B. Karuthedath and N. Schwesinger, "An improved capacitance-based intentionally imperfect sensor for measuring mechanical parameters," in 8th International Conference on Sensing and Technology (ICST), Liverpool, UK, 2014.
- C. B. Karuthedath and N. Schwesinger, "Design and fabrication of individualized capacitive microsensor for tilt measurement," in IEEE SENSORS, Busan, South Korean, 2015.
- C. B. Karuthedath, U. Fikri, and N. Schwesinger, "Resistive characterization of soft conductive pdms membranes for sensor applications," in IEEE Sensors Applications Symposium (SAS), Catania, Italy, 2016 (Best Student Paper Award).
- C. B. Karuthedath, S. Aung, and N. Schwesinger, "Finite element analysis of differential capacitive puf sensors," in IEEE Sensors Applications Symposium (SAS) Catania, Italy, 2016.
- C. B. Karuthedath, S. Aung, and N. Schwesinger, "A capacitive identification-sensor with internal puf," in International Conference on Mechanical Engineering and Electrical Systems (ICMES), Hong Kong, 2016.
- C. B. Karuthedath, U. Fikri, F. Ruf, and N. Schwesinger, "Characterization of carbon black filled pdms composite membranes for sensor applications," in Symposium on Advanced Material Research (ISAMR), Seoul, South Korea, 2017 (First Paper Award).
- C.B. Karuthedath and N. Schwesinger, " Nature Inspired Capacitive Sensor with Unique and Unclonable Characteristic," in International Conference on Sensors, Materials and Manufacturing (ICSMM 2017), Chiayi, Taiwan, 2017 (Best presentation award).
- N. Schwesinger and C.B. Karuthedath, "An inertia based sensor with dynamic PUF," in 11th International Conference on Sensing and Technology (ICST), Sydney, Australia, 2017 (Best presentation award).

- C. B. Karuthedath and N. Schwesinger, "Sensor zum bereitstellen einerphysikalisch unklonbaren funktion, herstellungsverfahren, identizierungsvorrichtungsowie auslesesystem," Nov. 28 2016, DE Patent App. 2016112816435900DE (patent pending).

Acknowledgment

Thank God for the wisdom, health and strength that he has been bestowed upon me during this research, and throughout my life.

I would like to express my sincere gratitude to my supervisor Prof. Dr.-Ing. Norbert Schwesinger for all the support and encouragement during my PhD. His deep insight and immense knowledge helped at various stages of my research. I also thank Mr. Peter Wirth who has acted as my mentor and provided valuable insights during the initial stages of my PhD. I gratefully acknowledge the funding received towards my PhD from the Erasmus Mundus Heritage Scholarship program.

I would like to thank my Master Thesis supervisor Dr. Boby George for giving me the courage and wish to do a PhD.

I also like to use this opportunity to thank my students Ahmed, Friederike, Samir, Sithu and Ubaidul. Guiding their theses not only helped to broaden my understanding but also improved my supervisory skills. I am indebted to my collegues Sherif, Sandy, Mohanad, Ricky, Max and Lars, and also the colleagues of TEP, especially Franz, Steve, Thomas and Johannes for their helps during different stages of this thesis.

Special thanks to Wang, you were a great source of support and motivation during these period. I am lucky to have friends like Adhi, Adri, Anil, Arya, Anoop, Charlie, Fede, Ivine, Jithu, Jobish, Milan and Sijo.

And most importantly, I am grateful to Appa, Amma and Luckachan for their love and care.

Last but not least, I would like to thank my wife Christy for her immense support during the final stages of this thesis.

List of Figures

List of Tables

Bibliography

[1] J. Benyus, *Biomimicry: Innovation Inspired By Nature.* New York, USA: HarperCollins, 1997.

[2] K. Hargroves and M. Smith, "Innovation inspired by nature: Biomimicry," *Ecos*, vol. 2006, no. 129, pp. 27–29, 2006.

[3] P. Arnarson, "Biomimicry," *Reykjavjk University*, 2011, accessed: Oct 2014. [Online]. Available: http://olafurandri.com/nyti/papers2011/Biomimicry%20-%20P%C3%A9tur%20%C3%96rn%20Arnarson.pdf

[4] H. Schmitz and H. Bleckmann, "The photomechanic infrared receptor for the detection of forest fires in the beetle melanophila acuminata (coleoptera: Buprestidae)," *Journal of Comparative Physiology A*, vol. 182, no. 5, pp. 647–657, 1998.

[5] J. A. Thomas, *Echolocation in bats and dolphins.* Chicago, USA: University of Chicago Press, 2004.

[6] C. E. OConnell-Rodwell, "Keeping an ear to the ground: seismic communication in elephants," *Physiology*, vol. 22, no. 4, pp. 287–294, 2007.

[7] T. H. Bullock, C. D. Hopkins, and R. R. Fay, *Electroreception.* Berlin, Germany: Springer, 2006.

[8] B. L. Partridge and T. J. Pitcher, "The sensory basis of fish schools: relative roles of lateral line and vision," *Journal of Comparative Physiology*, vol. 135, no. 4, pp. 315–325, 1980.

[9] Y. Vlasov, A. Legin, A. Rudnitskaya, C. Di Natale, and A. D'amico, "Nonspecific sensor arrays (" electronic tongue") for chemical analysis of liquids (iupac technical report)," *Pure and Applied Chemistry*, vol. 77, no. 11, pp. 1965–1983, 2005.

[10] E. A. Baldwin, J. Bai, A. Plotto, and S. Dea, "Electronic noses and tongues: Applications for the food and pharmaceutical industries," *Sensors*, vol. 11, no. 5, pp. 4744–4766, 2011.

[11] M. L. Hammock, A. Chortos, B. C.-K. Tee, J. B.-H. Tok, and Z. Bao, "25th anniversary article: The evolution of electronic skin (e-skin): A brief history, design considerations, and recent progress," *Advanced Materials*, vol. 25, no. 42, pp. 5997–6038, 2013.

[12] M. G. Metzen, S. Biswas, H. Bousack, M. G. Gottwald, K. Mayekar, and G. von der Emde, "A biomimetic active electrolocation sensor for detection of atherosclerotic lesions in blood vessels," *IEEE Sensors journal*, vol. 12, no. 2, pp. 325–331, 2012.

[13] R. Müller and R. Kuc, "Biosonar-inspired technology: goals, challenges and insights," *Bioinspiration & biomimetics*, vol. 2, no. 4, p. S146, 2007.

[14] Y. Yang, J. Chen, J. Engel, S. Pandya, N. Chen, C. Tucker, S. Coombs, D. L. Jones, and C. Liu, "Distant touch hydrodynamic imaging with an artificial lateral line," *Proceedings of the National Academy of Sciences*, vol. 103, no. 50, pp. 18 891–18 895, 2006.

[15] Y. Yang, N. Nguyen, N. Chen, M. Lockwood, C. Tucker, H. Hu, H. Bleckmann, C. Liu, and D. L. Jones, "Artificial lateral line with biomimetic neuromasts to emulate fish sensing," *Bioinspiration & biomimetics*, vol. 5, no. 1, p. 016001, 2010.

[16] A. T. Abdulsadda and X. Tan, "An artificial lateral line system using ipmc sensor arrays," *International Journal of Smart and Nano Materials*, vol. 3, no. 3, pp. 226–242, 2012.

[17] J. van Wyhe, "Charles darwin: gentleman naturalist: A biographical sketch," *Darwin Online*, 2008, accessed: Nov 2014. [Online]. Available: http://darwin-online.org.uk/darwin.html

[18] M. Burge and W. Burger, "Ear biometrics," in *Biometrics*. Berlin, Germany: Springer, 1996, pp. 273–285.

[19] D. Zhang, Z. Liu, J.-q. Yan, and P.-f. Shi, "Tongue-print: A novel biometrics pattern," in *International Conference on Biometrics*, Crystal City, USA, 2007.

[20] M. J. McHenry, J. A. Strother, and S. M. Van Netten, "Mechanical filtering by the boundary layer and fluid–structure interaction in the superficial neuromast of the fish lateral line system," *Journal of Comparative Physiology A*, vol. 194, no. 9, pp. 795–810, 2008.

[21] A. Wark and C. Peichel, "Lateral line diversity among ecologically divergent three-spine stickleback populations," *Journal of Experimental Biology*, vol. 213, no. 1, pp. 108–117, 2010.

[22] R. Sarlo and D. Leo, "Airflow sensing with arrays of hydrogel supported artificial hair cells," in *ASME Conference on Smart Materials, Adaptive Structures and Intelligent Systems*, Colorado, USA, 2015.

[23] A. Jain, R. Bolle, and S. Pankanti, *Biometrics: personal identification in networked society*. Berlin, Germany: Springer, 2006.

[24] H. Bar-El, "Known attacks against smartcards," 2005, White Paper, accessed: March 2014. [Online]. Available: http://www.infosecwriters.com/text_resources/pdf/Known_Attacks_Against_Smartcards.pdf

[25] R. Maes, *Physically Unclonable Functions*. Berlin, Germany: Springer, 2013.

[26] G. E. Suh and S. Devadas, "Physical unclonable functions for device authentication and secret key generation," in *44th Annual Design Automation Conference*, San Diego, USA, 2007.

[27] C. Tremlet, "Secure authentication based on physically unclonable functions," Mar. 10 2014, US Patent App. 14/202,239.

[28] S. Devadas, E. Suh, S. Paral, R. Sowell, T. Ziola, and V. Khandelwal, "Design and implementation of puf-based" unclonable" rfid ics for anti-counterfeiting and security applications," in *IEEE International Conference on RFID*, Las Vegas, USA, 2008.

[29] R. Maes, A. Van Herrewege, and I. Verbauwhede, "Pufky: a fully functional puf-based cryptographic key generator," in *International Workshop on Cryptographic Hardware and Embedded Systems*, Leuven, Belgium, 2012.

[30] J. Zhang, Y. Lin, Y. Lyu, and G. Qu, "A puf-fsm binding scheme for fpga ip protection and pay-per-device licensing," *IEEE Transactions on Information Forensics and Security*, vol. 10, no. 6, pp. 1137–1150, 2015.

[31] J. Kong, F. Koushanfar, P. K. Pendyala, A.-R. Sadeghi, and C. Wachsmann, "Pufatt: Embedded platform attestation based on novel processor-based pufs," in *51st ACM/EDAC/IEEE Design Automation Conference (DAC)*, San Francisco, USA, 2014.

[32] C.-W. Wong and M. Wu, "Counterfeit detection using paper puf and mobile cameras," in *IEEE International Workshop on Information Forensics and Security (WIFS)*, Rome, Italy, 2015.

[33] S. Morozov, A. Maiti, and P. Schaumont, "An analysis of delay based puf implementations on fpga," in *International Symposium on Applied Reconfigurable Computing*, Bangkok, Thailand, 2010.

[34] J. Guajardo, S. S. Kumar, G.-J. Schrijen, and P. Tuyls, "Fpga intrinsic pufs and their use for ip protection," in *International workshop on Cryptographic Hardware and Embedded Systems*, Vienna, Austria, 2007.

[35] J. T. Ficke, W. E. Hall, T. B. Hook, M. A. Sperling, and L. Wissel, "Physically unclonable function implemented through threshold voltage comparison," Dec. 31 2013, US Patent 8,619,979.

[36] R. Pappu, B. Recht, J. Taylor, and N. Gershenfeld, "Physical one-way functions," *Science*, vol. 297, no. 5589, pp. 2026–2030, 2002.

[37] D. Roy, J. H. Klootwijk, N. A. Verhaegh, H. H. Roosen, and R. A. Wolters, "Comb capacitor structures for on-chip physical uncloneable function," *IEEE Transactions on Semiconductor Manufacturing*, vol. 22, no. 1, pp. 96–102, 2009.

[38] J. Jackson, "Ready, aim, record: Armys prototype system uses rfid tags to track weapons use," *GCN Government Computer News*, 2008, accessed: Jan 2016. [Online]. Available: http://www.gcn.com/Articles/2008/05/01/Ready-aim-record.aspx

[39] M. C. O'Connor, "Three approaches to iot security: Part one," *IOT Journal*, 2005, accessed: Jan 2016. [Online]. Available: http://http://www.iotjournal.com/articles/view?13327

[40] Y. Shoukry, P. Martin, P. Tabuada, and M. Srivastava, "Non-invasive spoofing attacks for anti-lock braking systems," in *International Workshop on Cryptographic Hardware and Embedded Systems*, Santa Barbara, USA, 2013.

[41] I. Haider, M. Höberl, and B. Rinner, "Trusted sensors for participatory sensing and iot applications based on physically unclonable functions," in *2nd ACM International Workshop on IoT Privacy, Trust, and Security*, New York, USA, 2016.

[42] D. F. Kune, J. Backes, S. S. Clark, D. Kramer, M. Reynolds, K. Fu, Y. Kim, and W. Xu, "Ghost talk: Mitigating emi signal injection attacks against analog sensors," in *Security and Privacy (SP), 2013 IEEE Symposium on*, Washington, USA, 2013.

[43] Y. Son, H. Shin, D. Kim, Y. Park, J. Noh, K. Choi, J. Choi, and Y. Kim, "Rocking drones with intentional sound noise on gyroscopic sensors," in *24th USENIX Security Symposium (USENIX Security 15)*, 2015, pp. 881–896.

[44] A. Aysu, N. F. Ghalaty, Z. Franklin, M. P. Yali, and P. Schaumont, "Digital fingerprints for low-cost platforms using mems sensors," in *Proceedings of the Workshop on Embedded Systems Security*, Montreal Canada, 2013.

[45] O. Willers, C. Huth, J. Guajardo, and H. Seidel, "Mems-based gyroscopes as physical unclonable functions," *IACR Cryptology ePrint Archive*, 2016, accessed: Nov 2016. [Online]. Available: https://eprint.iacr.org/2009/277.pdf

[46] Y. Cao, L. Zhang, S. S. Zalivaka, C.-H. Chang, and S. Chen, "Cmos image sensor based physical unclonable function for coherent sensor-level authentication," *IEEE Transactions on Circuits and Systems*, vol. 62, no. 11, pp. 2629–2640, 2015.

[47] U. Rührmair, J. Martinez-Hurtado, X. Xu, C. Kraeh, C. Hilgers, D. Kononchuk, J. J. Finley, and W. P. Burleson, "Virtual proofs of reality and their physical implementation," in *IEEE Symposium on Security and Privacy*, San Jose, USA, 2015.

[48] Y. Gao, H. Ma, D. C. Ranasinghe, S. F. Al-Sarawi, and D. Abbott, "Exploiting unreliability of the puf to secure remote wireless sensing," in *Cryptology ePrint Archive*, 2015, accessed: Jan 2016. [Online]. Available: https://eprint.iacr.org/2015/1240

[49] K. Shimizu, T. Sugawara, and D. Suzuki, "Puf as a sensor," in *IEEE 4th Global Conference on Consumer Electronics (GCCE)*, Osaka City, Japan, 2015.

[50] J. Rajendran, J. Tang, and R. Karri, "Securing pressure measurements using sensorpufs," in *IEEE International Symposium on Circuits and Systems (ISCAS)*, Montreal, Canada, 2016.

[51] K. Rosenfeld, E. Gavas, and R. Karri, "Sensor physical unclonable functions," in *IEEE International Symposium on Hardware-Oriented Security and Trust (HOST)*, Anaheim, USA, 2010.

[52] P. M. Hofman, J. G. Van Riswick, and A. J. Van Opstal, "Relearning sound localization with new ears," *Nature neuroscience*, vol. 1, no. 5, pp. 417–421, 1998.

[53] C. B. Karuthedath and N. Schwesinger, "Sensor zum bereitstellen einer physikalisch unklonbaren funktion, herstellungsverfahren, identifizierungsvorrichtung sowie auslesesystem," Nov. 28 2016, DE Patent App. 2016112816435900DE (patent pending).

[54] C. B. Karuthedath and N. Schwesinger, "An improved capacitance-based intentionally imperfect sensor for measuring mechanical parameters," in *8th International Conference on Sensing and Technology (ICST)*, Liverpool, UK, 2014.

[55] C. B. Karuthedath and N. Schwesinger, "Design and fabrication of individualized capacitive microsensor for tilt measurement," in *IEEE SENSORS*, Busan, South Korean, 2015.

[56] C. B. Karuthedath, U. Fikri, and N. Schwesinger, "Resistive characterization of soft conductive pdms membranes for sensor applications," in *IEEE Sensors Applications Symposium (SAS)*. Catania, Italy, 2016.

[57] C. B. Karuthedath, U. Fikri, F. Ruf, and N. Schwesinger, "Characterization of carbon black filled pdms composite membranes for sensor applications," in *Symposium on Advanced Material Research (ISAMR)*. Seoul, South Korea, 2017.

[58] C. B. Karuthedath, S. Aung, and N. Schwesinger, "Finite element analysis of differential capacitive puf sensors," in *IEEE Sensors Applications Symposium (SAS)*. Catania, Italy, 2016.

[59] C. B. Karuthedath, S. Aung, and N. Schwesinger, "A capacitive identification-sensor with internal puf," in *International Conference on Mechanical Engineering and Electrical Systems (ICMES)*, Hong Kong, 2016.

[60] E. Bischur, S. Michel, and N. Schwesinger, "Intentionally imperfect sensors for measuring mechanical parameters," in *Seventh International Conference on Sensing Technology (ICST)*, Wellington, New Zealand, 2013.

[61] C. B. Karuthedath and B. George, "A simple analog front-end circuit for grounded capacitive sensors with offset capacitance," in *IEEE International Instrumentation and Measurement Technology Conference (I2MTC)*, Liverpool, UK, 2013.

[62] G. Brasseur, "Design rules for robust capacitive sensors," *IEEE Transactions on Instrumentation and Measurement*, vol. 52, no. 4, pp. 1261–1265, 2003.

[63] L. K. Baxter, *Capacitive sensors.* New York, USA: IEEE press, 2000.

[64] A. V. Mamishev, K. Sundara-Rajan, F. Yang, Y. Du, and M. Zahn, "Interdigital sensors and transducers," *Proceedings of the IEEE*, vol. 92, no. 5, pp. 808–845, 2004.

[65] M. J. Madou, *Fundamentals of microfabrication: the science of miniaturization.* Florida, USA: CRC press, 2002.

[66] "Sylgard 184 silicone elastomer," Dow Corning, 2007, USA, Product Information,.

[67] "Alpa-sil classic," CHT R. Breitlich GmbH, 2009, Austria, Product Information.

[68] A. Maiti, V. Gunreddy, and P. Schaumont, "A systematic method to evaluate and compare the performance of physical unclonable functions," in *Embedded systems design with FPGAs.* Berlin, Germany: Springer, 2013, pp. 245–267.

[69] J. H. McDonald, *Handbook of biological statistics.* Baltimore, USA: Sparky House Publishing, 2009.

[70] J. M. Bland and D. Altman, "Statistical methods for assessing agreement between two methods of clinical measurement," *The Lancet*, vol. 327, no. 8476, pp. 307–310, 1986.

[71] J. Lee Rodgers and W. A. Nicewander, "Thirteen ways to look at the correlation coefficient," *The American Statistician*, vol. 42, no. 1, pp. 59–66, 1988.

[72] I. Lawrence and K. Lin, "A concordance correlation coefficient to evaluate reproducibility," *Biometrics*, vol. 45, no. 1, pp. 255–268, 1989.

[73] "AD7746 evaluation board: EVAL-AD7746EB datasheet," analog Devices, 2005, USA, Datasheet.

[74] J. C. McDonald and G. M. Whitesides, "Poly (dimethylsiloxane) as a material for fabricating microfluidic devices," *Accounts of chemical research*, vol. 35, no. 7, pp. 491–499, 2002.

[75] C. Liu, "Recent developments in polymer mems," *Advanced Materials*, vol. 19, no. 22, pp. 3783–3790, 2007.

[76] X. Riedl, C. Bolzmacher, R. Wagner, K. Bauer, and N. Schwesinger, "A novel pdms based capacitive pressure sensor," Waikoloa, USA, 2010.

[77] W. Hu, S. Chen, B. Zhuo, Q. Li, R. Wang, and X. Guo, "Highly sensitive and transparent strain sensor based on thin elastomer film," *IEEE Electron Device Letters*, vol. 37, no. 5, pp. 667–670, 2016.

[78] X. Gong and W. Wen, "Polydimethylsiloxane-based conducting composites and their applications in microfluidic chip fabrication," *Biomicrofluidics*, vol. 3, no. 1, 2009.

[79] T. Mirfakhrai, J. D. Madden, and R. H. Baughman, "Polymer artificial muscles," *Materials today*, vol. 10, no. 4, pp. 30–38, 2007.

[80] D. J. Lipomi, M. Vosgueritchian, B. C. Tee, S. L. Hellstrom, J. A. Lee, C. H. Fox, and Z. Bao, "Skin-like pressure and strain sensors based on transparent elastic films of carbon nanotubes," *Nature nanotechnology*, vol. 6, no. 12, pp. 788–792, 2011.

[81] A. Khosla, "Nanoparticle-doped electrically-conducting polymers for flexible nano-micro systems," *Electrochemical Society Interface*, vol. 21, no. 3-4, pp. 67–70, 2012.

[82] J. Ruhhammer, M. Zens, F. Goldschmidtboeing, A. Seifert, and P. Woias, "Highly elastic conductive polymeric mems," *Science and Technology of Advanced Materials*, vol. 16, no. 1, 2015.

[83] A. Larmagnac, S. Eggenberger, H. Janossy, and J. Vörös, "Stretchable electronics based on ag-pdms composites," *Scientific reports*, vol. 4, no. 1, 2014.

[84] C.-X. Liu and J.-W. Choi, "Patterning conductive pdms nanocomposite in an elastomer using microcontact printing," *Journal of Micromechanics and Microengineering*, vol. 19, no. 8, 2009.

[85] X. Niu, S. Peng, L. Liu, W. Wen, and P. Sheng, "Characterizing and patterning of pdms-based conducting composites," *Advanced Materials*, vol. 19, no. 18, pp. 2682–2686, 2007.

[86] N. Lu, C. Lu, S. Yang, and J. Rogers, "Highly sensitive skin-mountable strain gauges based entirely on elastomers," *Advanced Functional Materials*, vol. 22, no. 19, pp. 4044–4050, 2012.

[87] J. Dusek, M. Triantafyllou, M. E. Woo, and J. Lang, "Carbon black-pdms composite conformal pressure sensor arrays for near-body flow detection," in *OCEANS*, TAIPEI, Taiwan, 2014.

[88] M. Ali Raza, A. Westwood, C. Stirling, R. Brydson, and N. Hondow, "Effect of nanosized carbon black on the morphology, transport, and mechanical properties of rubbery epoxy and silicone composites," *Journal of Applied Polymer Science*, vol. 126, no. 2, pp. 641–652, 2012.

[89] M. A. Unger, H.-P. Chou, T. Thorsen, A. Scherer, and S. R. Quake, "Monolithic microfabricated valves and pumps by multilayer soft lithography," *Science*, vol. 288, no. 5463, pp. 113–116, 2000.

[90] V. Tsouti, V. Mitrakos, P. Broutas, and S. Chatzandroulis, "Modeling and development of a flexible carbon black-based capacitive strain sensor," *IEEE Sensors Journal*, vol. 16, no. 9, pp. 3059–3067, 2016.

[91] A.-L. Deman, M. Brun, M. Quatresous, J.-F. Chateaux, M. Frénéa-Robin, N. Haddour, V. Semet, and R. Ferrigno, "Characterization of c-pdms electrodes for electrokinetic applications in microfluidic systems," *Journal of Micromechanics and Microengineering*, vol. 21, no. 9, 2011.

[92] N. Lu, C. Lu, S. Yang, and J. Rogers, "Highly sensitive skin-mountable strain gauges based entirely on elastomers," *Advanced Functional Materials*, vol. 22, no. 19, pp. 4044–4050, 2012.

[93] K. Chu and S.-H. Park, "Fabrication of a hybrid carbon-based composite for flexible heating element with a zero temperature coefficient of resistance," *IEEE Electron Device Letters*, vol. 36, no. 1, pp. 50–52, 2015.

[94] B. A. Reyes, H. F. Posada-Quintero, J. R. Bales, A. L. Clement, G. D. Pins, A. Swiston, J. Riistama, J. P. Florian, B. Shykoff, M. Qin *et al.*, "Novel electrodes for underwater ecg monitoring," *IEEE Transactions on Biomedical Engineering*, vol. 61, no. 6, pp. 1863–1876, 2014.

[95] M. Liu, J. Sun, Y. Sun, C. Bock, and Q. Chen, "Thickness-dependent mechanical properties of polydimethylsiloxane membranes," *Journal of micromechanics and microengineering*, vol. 19, no. 3, p. 035028, 2009.

[96] D. Stauffer and A. Aharony, *Introduction to percolation theory*. Philadelphia, USA: Taylor and Francis, 1994.

[97] S. Stankovich, D. A. Dikin, G. H. Dommett, K. M. Kohlhaas, E. J. Zimney, E. A. Stach, R. D. Piner, S. T. Nguyen, and R. S. Ruoff, "Graphene-based composite materials," *nature*, vol. 442, no. 7100, pp. 282–286, 2006.

[98] *Saftey Data Sheet*, Cabot Corperation, 06 2016.

[99] *Saftey Data Sheet*, Sigma-Aldrich, 11 2016.

[100] J. N. Lee, C. Park, and G. M. Whitesides, "Solvent compatibility of poly (dimethylsiloxane)-based microfluidic devices," *Analytical chemistry*, vol. 75, no. 23, pp. 6544–6554, 2003.

[101] D. Prat, J. Hayler, and A. Wells, "A survey of solvent selection guides," *Green Chemistry*, vol. 16, no. 10, pp. 4546–4551, 2014.

[102] *Saftey Data Sheet*, Sigma-Aldrich, 12 2016.

[103] S. Krishnan, "On the manufacture of very thin elastomeric films by spin-coating," PhD dissertation, Massachusetts Institute of Technology, Massachusetts, USA, 2007.

[104] W. Luheng, D. Tianhuai, and W. Peng, "Influence of carbon black concentration on piezoresistivity for carbon-black-filled silicone rubber composite," *Carbon*, vol. 47, no. 14, pp. 3151–3157, 2009.

[105] X.-W. Zhang, Y. Pan, Q. Zheng, and X.-S. Yi, "Time dependence of piezoresistance for the conductor-filled polymer composites," *Journal of Polymer Science part B: polymer physics*, vol. 38, no. 21, pp. 2739–2749, 2000.

[106] M. Kalantari, J. Dargahi, J. Kövecses, M. G. Mardasi, and S. Nouri, "A new approach for modeling piezoresistive force sensors based on semiconductive polymer composites," *IEEE/ASME Transactions on Mechatronics*, vol. 17, no. 3, pp. 572–581, 2012.

[107] W. Luheng, D. Tianhuai, and W. Peng, "Influence of carbon black concentration on piezoresistivity for carbon-black-filled silicone rubber composite," *Carbon*, vol. 47, no. 14, pp. 3151–3157, 2009.

[108] J. R. Davis, *Tensile testing*. Ohio, USA: ASM international, 2004.

[109] I. Johnston, D. McCluskey, C. Tan, and M. Tracey, "Mechanical characterization of bulk sylgard 184 for microfluidics and microengineering," *Journal of Micromechanics and Microengineering*, vol. 24, no. 3, pp. 1–7, 2014.

[110] W. K. Schomburg, *Membranes*. Berlin, Germany: Springer, 2015.

[111] C. B. Karuthedath and B. George, "A capacitive ice layer detection system suitable for autonomous inspection of runways using an rov," in *IEEE International Symposium on Robotic and Sensors Environments (ROSE)*, Magdeburg, Germany, 2012.

[112] E. O. Doebelin and D. N. Manik, "Measurement systems: application and design," 2004.

[113] M. Bond, O. Choudary, S. J. Murdoch, S. Skorobogatov, and R. Anderson, "Chip and skim: cloning emv cards with the pre-play attack," in *IEEE Symposium on Security and Privacy*, San Jose, USA, 2014, pp. 49–64.

[114] C. Van der Bijl, "The cloning of credit cards: The dolly of the electronic era," *Stellenbosch Law Review*, vol. 18, pp. 331–336, 2007.

[115] O. Kulikovska, M. Paeschke, W. Fumy, and F. Morgner, "Identity card with physical unclonable function," Jul. 12 2013, US Patent App. 14/436,253.

[116] S. A. Goorden, M. Horstmann, A. P. Mosk, B. Škorić, and P. W. Pinkse, "Quantum-secure authentication of a physical unclonable key," *Optica*, vol. 1, no. 6, pp. 421–424, 2014.

[117] "Identification cardsphysical characteristics," *ISO/IEC 7810:2003*.

[118] "Strong authentication using smart card technology for logical access," 2012, White Paper, accessed: Oct 2015. [Online]. Available: http://www.smartcardalliance.org/resources/pdf/Strong_Auth_WP_FINAL_112112.pdf

[119] S. Schmitz and C. Roser, "A new state-of-the-art keyless entry system," Detroit, USA, Tech. Rep., 1998.

[120] T. Liu, W. Liew, and H. Everss, "An integrated automobile keyless operation system," Detroit, USA, Tech. Rep., 2000.

[121] T. J. Waraksa, K. D. Fraley, R. E. Kiefer, D. G. Douglas, and L. H. Gilbert, "Passive keyless entry system," Jul. 17 1990, US Patent 4,942,393.

[122] D. Pearson, F. LeGasse, and J. Burgess, "Passive entry systems for vehicles and other applications," Apr. 22 2005, US Patent App. 11/112,204.

[123] A. Francillon, B. Danev, and S. Capkun, "Relay attacks on passive keyless entry and start systems in modern cars," in *18th Annual Network and Distributed System Security Symposium*, San Diego, USA, 2011.

[124] A. Atia *et al.*, "Interaction with tilting gestures in ubiquitous environments," *International Journal of UbiComp (IJU*, vol. 1, no. 3, pp. 1–13, 2010.

[125] P. Van Gastel and B. Gerdes, "Capacitive sensor array and method for detecting actuation gestures at a motor vehicle," Jun. 21 2012, US Patent App. 14/128,393.

[126] J. Lenz and S. Edelstein, "Magnetic sensors and their applications," *IEEE Sensors journal*, vol. 6, no. 3, pp. 631–649, 2006.

[127] M. Pervez Khan, A. Hussain, and K. S. Kwak, "Medical applications of wireless body area networks," *Int'l. J. Digital Content Technology and its Applications*, vol. 6, no. 3, 2009.